A study of the radiobiological modeling of the conformal radiation therapy in cancer treatment

BY

ANIL PRASAD PYAKURYAL
M.Sc., Physics, Tribhuvan University, Nepal 1998.
M.S., Electrical Engineering, Southern Illinois University, USA 2002.

THESIS

Submitted as a partial fulfillment of the requirements
for the degree of Doctor of Philosophy in Physics
in the Graduate College of the
University of Illinois at Chicago, 2012
Chicago, Illinois.

Defense Committee:

Sivalingam Sivananthan, Chair and Advisor

Sunyoung Jang, Co-Advisor,	Princeton Radiation Oncology Centre
Bharat B. Mittal,	Northwestern University Memorial Hospital
Jianqiao Luo,	Virginia Commonwealth University
Christoph H. Grein,	University of Illinois at Chicago
Robert Klie	University of Illinois at Chicago
Shailendra Shukla,	University of Florida

Dedication

This work is simply dedicated to the millions of people diagnosed with cancer each year around the globe. We hope that the outcomes of this work would be useful to the radiation oncology community in our global effort to improve the radiation guided treatments in cancer.

Acknowledgements

I would like to thank many people who have helped and inspired me during my doctoral study. I especially want to thank my adviser, Professor Dr. Sivalingam Sivananthan for his supervision and motivation in my research and study at the University of Illinois at Chicago.

I am also really grateful to my co-advisor Dr. Sunyoung Jang for his sincere guidance and support in my research work at the Northwestern Memorial Hospital (NMH) at Chicago, Illinois and the Rhode Island Hospital (RIH) at Providence, Rhode Island. I am also very grateful to the Chairman of the Radiation Oncology Department, Professor Dr. Bharat B Mittal for his generous support and motivation in my research work on the radiation guided treatments at the NMH Comprehensive Laurie Cancer Center. I am also indebted to the physicists Dr. Vythialingam Sathiaseelan, Mahesh Gopalakrishnan, Dr. Kenji Myint, and Dr. Alan Kappa for their assistance in my work at the Center. Similarly, I am also thankful to Dr. Jianqiao Luo for his guidance on the nuclear medicine research at Virginia Commonwealth University (VCU) at Richmond, Virginia. As a result, research life became smooth and rewarding for me.

Prof. Dr.Christoph H Grein, Dr. Robert Klie and Dr. Shailendra Shukla also deserve special thanks as my thesis committee members. I would also like to thank Prof. Dr. David Hofmann, Chairman of the Physics Department for the generous support during my study. It was my pleasure to contribute first of its kind of research work to the department and the university.

My deepest gratitude goes to my parents and family for their unflagging love and support throughout my life; this dissertation is simply impossible without them. Last but not the least, thanks be to God for my life through all the tests in the past eight years. You have made my life more bountiful. May your name be exalted, honored, and glorified.

Abstract

Cancer is one of the leading causes of mortalities in the world. The precise diagnosis of the disease helps the patients to select the appropriate modality of the treatments such as surgery, chemotherapy and radiation therapy. The physics of X-radiation and the advanced imaging technologies such as positron emission tomography (PET) and computed tomography (CT) plays an important role in the efficient diagnosis and therapeutic treatments in cancer. However, the accuracy of the measurements of the metabolic target volumes (MTVs) in the PET/CT dual-imaging modality is always limited. Similarly the external beam radiation therapy (XRT) such as 3D conformal radiotherapy (3DCRT) and intensity modulated radiation therapy (IMRT) is the most common modality in the radiotherapy treatment. These treatments are simulated and evaluated using the XRT plans and the standard methodologies in the commercial planning system. However, the normal organs are always susceptible to the radiation toxicity in these treatments due to lack of knowledge of the appropriate radiobiological models to estimate the clinical outcomes.

We explored several methodologies to estimate MTVs by reviewing various techniques of the target volume delineation using the static phantoms in the PET scans. The review suggests that the more precise and practical method of delineating PET MTV should be an intermediate volume between the volume coverage for the standardized uptake value (SUV; 2.5) of glucose and the 50% (40%) threshold of the maximum SUV for the smaller (larger) volume delineations in the radiotherapy applications. Similarly various types of optimal XRT plans were designed using the CT and PET/CT scans for the treatment of various types of cancer patients. The qualities of these plans were assessed using the universal plan-indices. The dose-volume criteria were also examined in the targets and organs by analyzing the conventional dose-volume histograms (DVHs). The biological models such as tumor control probability based on Poisson statistics model, and normal tissue complication probabilities based on Lyman-Kutcher-Burman model, were efficient to estimate the radiobiological outcomes of the treatments by taking into account of the dose-volume effects in the organs. Furthermore, a novel technique of spatial DVH analysis was also found to be useful to determine the primary cause of the complications in the critical organs in the treatments.

The study also showed that the 3DCRT and IMRT techniques offer the promising results in the XRT treatment of the left-breast and the prostate cancer patients respectively. Unfortunately, several organs such as salivary glands and larynx, and esophagus, were found to be significantly vulnerable to the radiation toxicity in the treatment of the head and neck (HN), and left-lung cancer patients respectively. The radiobiological outcomes were also found to be consistent with the clinical results of the IMRT based treatments of a significant number of the HN cancer patients.

Contents

List of Tables

List of Figures

Chapter I

Introduction

1.1 Background and motivation

Cancer is projected to be the number one leading causes of deaths in the world in 2011-2012 (World Health Organization, 2008). Global cancer death is expected to be more than 21,000 per day in 2012. In US alone, the current cancer-mortality is about 571,950 that accounts for the 20% of the total death, whereas the incidence stands above 1,596,670 each year (American Cancer Society, 2011). Four major diseases such as the lung and trachea cancer, the prostate cancer in male and the breast cancer in female, and the colorectal cancers, were the leading cause of deaths around the globe in the last decade (World Health Organization, 2011).

With the advent in technology, there is a great optimism and expectation of the precise diagnostic approach and the efficient treatment mechanism amongst the cancer patients. The advanced diagnostic imaging modalities such as computed tomography (CT) scan, positron emission tomography (PET) scan, magnetic resonance imaging (MRI), and ultrasound are the primary basis of the efficient diagnosis of the various types of cancers. However, various types of mechanical factors have limited its implications in the accurate diagnosis of the disease. Such drawbacks in the diagnostic imaging need to be addressed properly to achieve the good prognosis in the advanced treatment procedures of various types of cancers.

The basic sciences such as radiobiology, radiation physics, human anatomy and physiology, information technology, techniques of treatment planning, and the analytical statistics are the

fundamental pillars of the radiation oncology. The historical understanding of cancer as a disease of overly rapid cellular proliferation also made it logical to treat cancer patients with radiations such as gamma-rays and X-rays [1]. Within a few month of Roentgen's 1895 discovery of X-rays, the biological effects of ionizing radiation were recognized. In fact, Grubbe [2] states that the first patient was treated with x-rays for a far advanced carcinoma of the breast for curative and palliative purpose in 1896. By the early 1930's, Coutard [3] had developed a fractionated treatment scheme that remains the basis for current radiation therapy. By the 1950's, technological advances had made the treatment of malignant disease possible at far higher x-ray energies other than the early kV treatments. By the end of the decade, the Van de Graff generators, operating at 800-kV, were replaced by mega-voltage (MV) linear accelerators and Cobalt 60 teletherapy units. In general, two fundamental processes must be well understood in predicting and optimizing the effects of radiotherapy treatments such as the physics of ionizing radiation and the cellular response to the interaction of ionizing radiation.

The primary goal of radiotherapy, as declared by the National Cancer Institute (NCI), is the complete destruction of an entire tumor or the shrinking of a tumor sparing the critical organs as a mean of symptom relief. In the past thirty years, computer aided treatments and other developments in medical imaging have each contributed to more sophisticated radiation guided therapeutic strategies. Since the aim of radiotherapy is to kill cancer cells while minimizing the damage to the normal tissues, the expected effects of ionizing radiation to tumor targets and the critical organs must be well known [4]. However, cancer therapies have experienced tremendous setbacks in the past 30 years due to the associated toxic response, resulting in a significant number of treatment-induced deaths rather than disease-induced fatalities. Awareness regarding historic numbers of unsuccessful outcomes has forced patients to look for the alternatives to

bolster survival odds. In this pretext, the majority of this work was formed around the understanding of the volume delineation of the tumor targets, and the radiotherapy treatment planning and assessments, outcomes and prevention in cancer. This work has also employed novel computational approaches to estimate the chances of tumor control and the complications in the normal tissue organs using the dose-volume effects in the radiation guided treatments.

1.2 General overview of the chapters

In this study, more practical diagnostic approaches were implemented to identify the tumor targets using the CT and PET/CT dual-imaging modalities in various types of cancer patients. Furthermore, the advanced therapeutic techniques were employed to design the optimal radiation therapy plans in the treatment of the patients. These plans were assessed using the optimal plan evaluation techniques such as cumulative dose-volume histogram (cDVH) models and the universal plan-indices (UPIs). Since normal tissue organs are always vulnerable to the radiation toxicity in the radiotherapy treatments, several radiobiological models were also utilized to investigate the outcomes of these treatments in various types of cancers using the computational techniques. Notable dose-volume histogram (DVH) based radiobiological models include Poisson-statistics tumor control probability (TCP) and Lyman-Kutcher-Burman (LKB) normal tissue complication probability (NTCP) respectively. Furthermore, a novel technique of the spatial DVH (sDVH) analysis was also utilized to determine the primary cause of the complications in the normal tissues or the critical organs of the patients treated with external-beam radiation therapy (XRT) treatments.

Our discussion starts, in Chapter 2, with the review of CT image reconstruction and the PET phantom volume measurement techniques to determine the optimal method of target

volume delineations in the radiation therapy treatments. The chapter presents an overview of the CT-scan, PET-scan, and its dual-imaging modality applications in radiation therapy treatments.

Similarly Chapter 3 covers the fundamental applications of various types of XRT treatment techniques such as the 3D conformal radiation therapy (3DCRT), intensity modulated radiation therapy (IMRT), and electron beam therapy (EBT) respectively. It also describes the fundamental concepts in designing the radiation therapy treatment plans, the dose computation algorithms, the optimization rules, the novel plan evaluation techniques such as UPIs and DVH modeling, and standard biological modeling for the outcome assessments (BMOA) respectively.

Chapter 4 presents a general method to delineate the volume of a tumor target in CT and PET/CT scans, and the techniques in planning radiation therapy treatment of various types of cancers based on guidelines from International Commission on Radiation Units and Measurements (ICRU) and Radiation Therapy Oncology Group (RTOG). It also covers the dose measurements in water phantom, beam profiles, dose prescription, and the application of plan evaluation techniques using the Histogram Analysis in Radiation Therapy (HART) program.

Chapter 5 covers the details on the dose-volume effects in the organs in the XRT treatment plans, and the UPI evaluation of the plans. The control probability of the tumors and the possible complications in normal organs in the several types of the XRT treatments of head and neck, prostate, left-breast and left-lung cancer patients, will also be discussed respectively. The results were also compared with the clinical outcomes of the IMRT treatment of a significant number of head and neck cancer patients. The chapter concludes with the treatment chart analysis that summarizes the computational results of the treatments of these different cases.

Finally Chapter 6 covers the concluding remarks, future works, and would incorporate an appendix that includes published papers and presentations derived from this work.

Chapter II

Principle of diagnostic medical imaging

2.1 Cause and diagnosis in cancer

Normal cells in the body follow an orderly path of growth, division, and programmed death. However, malignant cells do not experience programmatic death unlike regular cells, and instead continue to grow and divide, leading to a mass of abnormal cells. Benign tumors stay in one spot and demonstrate limited growth whereas malignant tumors form when a cancerous cell manages to move throughout the body using the blood or lymph systems. Malignant cells divide and grow by making new blood vessels to feed itself in a process called angiogenesis. A tumor can spread to the other parts of the body and can grow further, invade and destroy other healthy tissues during metastasis. Metastasized tumors are very difficult to be diagnosed. These tumors can also release hormones that alter body function.

Cells can experience uncontrolled growth if there are mutations to deoxyribonucleic acid (DNA) and therefore, damage to the genes involved in cell division. Four key types of gene are responsible for the cell division process: (a) oncogenes that schedule cell division, (b) tumor suppressor genes which tell cells when not to divide, (c) suicide genes that control apoptosis and destroy the cells if something goes wrong, and (d) DNA-repair genes that instruct a cell to repair damaged DNA. Cancer occurs when a cell's gene mutations make the cell unable to correct DNA damage and unable to commit suicide. DNA mutations inhibit oncogenes and tumor suppressor

gene function, leading to uncontrollable cell growth. Cancer is generally classified into five broad groups: Carcinomas, Sarcomas, Lymphomas, Leukemia and Adenomas.

Early detection of any types of diseases can greatly improve the odds of successful treatment and survival. Physicians use information from primary symptoms and perform several diagnostic tests such as X-rays, CT scans, MRI scans, PET scans, ultrasound, pathology and cell biopsy, in order to verify the stage of the disease. The stage determines which choices will be available for the treatment and informs prognoses. The most common cancer staging method is called the TNM system. T (1-4) indicates the size of the primary tumor, N (0-3) indicates the degree to which the cancer has spread to nearby lymph nodes, and M (0-1) indicates whether the cancer has metastasized to other organs in the body. A small tumor that has not spread to lymph nodes or distant organs is typically staged as (T1, N0, and M0). TNM descriptions then lead to a simpler categorization of stages from 0 to 4, and the appropriate method of the treatments generally depends on the type and stage of the cancer, age, and health status of the patients.

2.2 Interaction of photons and electrons with biological materials

This section describes the interaction property of photon and particle beams with the biological materials such as tissues and bones, in the diagnostic, ortho-voltage and therapeutic regions. Particles and radiations transfer energy or dose to the atoms or molecules in the biological tissues through various types of electromagnetic interactions as discussed below.

2.2.1. Interaction of photons with biological materials

Photons may undergo various possible interactions with the atoms of the attenuators and the biological materials such as photoelectric effect, Compton effect, coherent scattering, and pair production. In the photoelectric effect, the photon interacts with a tightly bound orbital electron

of an atom of the target material, and disappears, while the orbital electron is ejected from the atom as a photoelectron with a kinetic energy (E_K) given as:

$$E_K = h\nu - E_B \; ; \tag{1}$$

where hν is the incident photon energy (E_{photon}) and E_B is the binding energy of the electron in that atom. The mass attenuation coefficient for the photoelectric effect ($\mu_{m,PE}$) is proportional to the term, $(Z_{eff}/E_{photon})^3$ where Z_{eff} is the effective atomic number of the material type.

In coherent (Rayleigh) scattering the photon interacts with a bound orbital electron in the atom. The event is elastic in the sense that the photon loses essentially none of its energy and is scattered through only a small angle. Although Rayleigh scattering does not transfer energy, it contributes to the attenuation coefficient in tissues and tissue equivalent materials. The mass Rayleigh attenuation coefficient ($\mu_{m,R}$) is proportional to the term, $Z_{eff}/(E_{photon})^2$.

The Compton effect, an incoherent scattering, represents a photon interaction with a free and stationary orbital electron. Since $h\nu >> E_B$, the photon loses a part of its energy (E_k) to the recoil (Compton) electron and is scattered as a secondary photon with larger wavelength (λ') at a scattering angle (θ) as shown in Fig. 2.1.

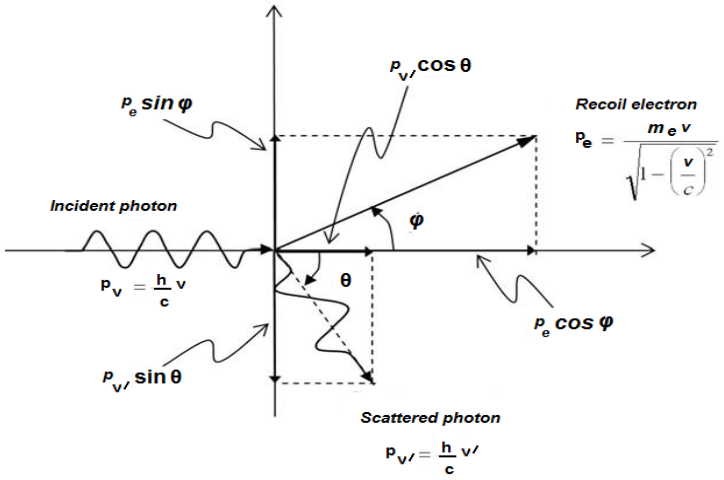

Fig. 2.1 Schematic diagram of the Compton scattering effect.

The mass Compton attenuation coefficient ($\mu_{m,C}$) is proportional to the term, (ρ_e / E_{photon}) where ρ_e is the electron density in a given mass of target material. The Compton interaction represents a photon interaction with an essentially free and stationary electron ($h\nu >> E_B$). Consequently, the mass Compton attenuation coefficient is independent of the atomic number (Z_{eff}) of the target material. Since ρ_e is larger for the tissues as compared to the calcium and phosphorous components in bone, superficial and high energy radiations are preferred in the diagnostic and therapeutic applications in cancer. On average, a 1 MeV photon undergoing Compton scattering will produce a 440 keV recoil electron and a 560 keV scattered photon; a 10 MeV photon will produce a 6.9 MeV recoil electron and a 3.1 MeV scattered photon; and a 100 MeV photon will produce an 80 MeV recoil electron and a 20 MeV scattered photon.

In pair production the photon disappears and an electron–positron pair with a combined kinetic energy equal to $h\nu–2m_ec^2$ is produced in the nuclear Coulomb field. Since mass is produced out of photon energy in the form of an electron–positron pair, pair production has an energy threshold of $2m_ec^2$ (1.02 MeV). The mass attenuation coefficient for the pair production ($\mu_{m,PP}$) varies approximately as $Z_{eff}\, E_{photon}^{1/2}$.

The total mass attenuation coefficient (μ_m) for the gross interaction process is given as a sum of mass attenuation coefficients for the individual photon interactions.

$$\frac{\mu}{\rho} = \frac{\mu_{PE}}{\rho} + \frac{\mu_R}{\rho} + \frac{\mu_C}{\rho} + \frac{\mu_{PP}}{\rho}\,; \qquad (2)$$

Photonuclear reactions generally occur when a high energy photon is absorbed by the nucleus of an atom, resulting in an emission of a neutron ((x, n) reaction) or proton ((x,p) reaction) that could pose a health hazard to the clinical personnel. The probability for photonuclear reactions is much smaller than that for other photon interactions, and their contribution to the total attenuation coefficient amounts to only a few percent at high energy.

Depending on their origin, the indirectly ionizing photon radiations can be categorized as Bremsstrahlung X-rays, characteristic X-rays, γ-rays in nuclei decay, and discrete γ-radiation produced in positron–electron annihilation process. The intensity I(x) of a narrow mono-energetic photon beam, attenuated by a target material of thickness (x), is given as:

$$I(x) = I_o . \exp[-\mu_m(h\nu, Z).\rho x]; \quad (3)$$

where I_o is the original intensity of the unattenuated beam and ρ is the density of the target material of thickness (x). Similarly $\mu_m(h\nu,Z)$ is the mass attenuation coefficient, which depends on the photon energy (hν) and atomic number (Z) of the target material.

The probability for a photon to undergo any type of interaction with an attenuator depends on hν of the photon and on the Z_{eff} of the attenuating material. In general, the photoelectric effect predominates at low photon energies, the Compton effect at intermediate energies, and the pair production at high photon energies. Fig. 2.2 and Fig. 2.3 show the regions of relative predominance of the three most important individual effects with hν and Z_{eff} as parameters [5].

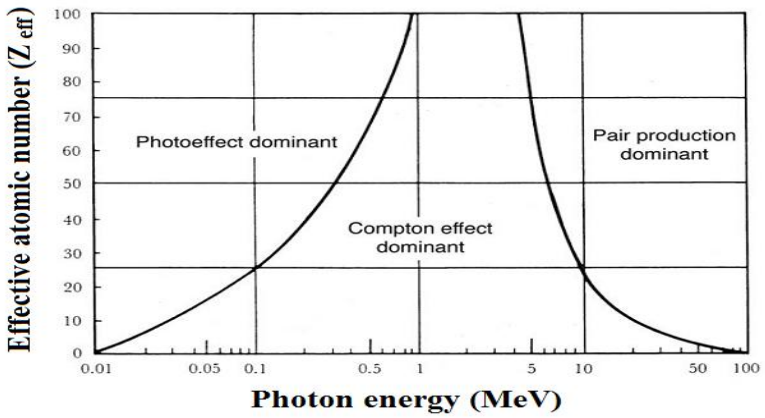

Fig. 2.2 The diagram presents the regions of relative predominance of the three main forms of the photon interaction with matters. Border lines indicate the transitions in absorption coefficients of the material at different energy regions [5].

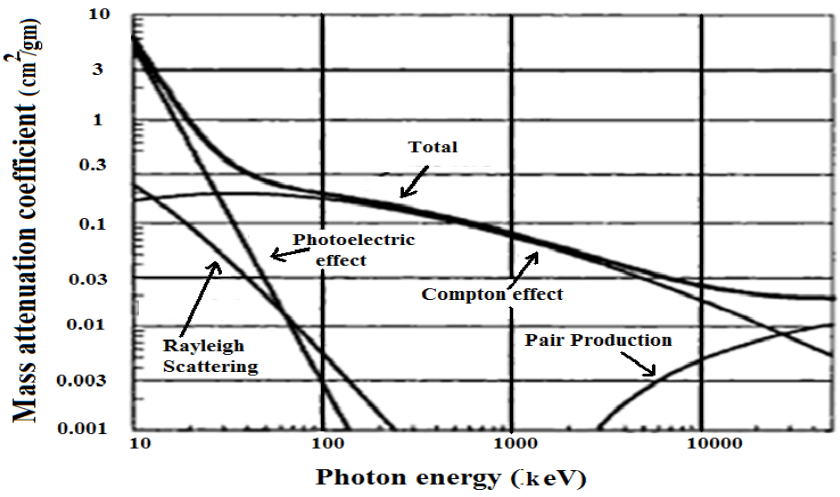

Fig. 2.3 Dependence of the mass attenuation coefficients, $\mu_m(h\nu,Z)$, of the water equivalent soft tissue (Z_{eff} =7) on the energy of the incident photons [5].

2.2.2. Interaction of electrons with biological materials

When an energetic electron traverses an absorbing material, it interacts with the matter through Coulomb interactions with the orbital electrons and atomic nuclei. Through these collisions the electrons may lose their kinetic energy by radiative losses in the form of bremsstrahlung radiation, excitation of the orbital electrons, or change their direction of travel by scattering mechanism. Energy losses and scattering are described by stopping power and scattering power respectively. The collisions between the incident electron and an orbital electron or nucleus of an atom may be elastic or inelastic. In an elastic collision the electron is deflected from its original path but no energy loss occurs, while in an inelastic collision some of its energy is dissipated by radiative loss or excitation of the atoms.

Coulomb interactions between the incident electron and orbital electrons of an absorber result in ionization and excitation of the absorber atoms. It leads to the collisional energy losses and are characterized by collision (ionization) stopping powers. Similarly coulomb interactions between the incident electron and nuclei of the absorber atom result in electron scattering and the

energy loss of the electron as bremsstrahlung radiation. These types of energy loss are characterized by radiative stopping powers. The energy loss by radiation and the radiative yield increase directly with the absorber atomic number (Z) and the kinetic energy of electrons. The radiation yield for X-ray targets in the diagnostic radiology energy range (~100 keV) is of the order of 1%, while in the megavoltage energy range it amounts to 10–20% [5].

2.3 Image reconstruction algorithms

Since its introduction in the 1970s, CT has become an important diagnostic tool in medical imaging to supplement X-rays and ultra-sonography. It employs X-rays to generate a view of "slices" through the body. CT produces a volume of data which can be manipulated, through a process known as windowing and leveling. It is a gold standard image in the diagnostic application and the radiotherapy treatment of cancers. In recent years the CT scan is rapidly involved into the process of tomography [6]. Reconstruction in modern scanners uses special image processing algorithms such as filtered back projection (FBP) and convolution back projection (CBP), based on the nature of the scans such as transmission or emission tomography.

Real CT scanners generally take several different line pictures at each of the 180 different positions of the X-ray tube. Pixels in an image obtained by CT scanners are displayed in terms of relative radio-density. The pixel itself is displayed according to the mean attenuation of the tissues that it corresponds to on a scale from +3071 (most attenuating) to -1024 (least attenuating) on the Hounsfield scale. For a material, X, with the linear attenuation coefficient (μ_X), the corresponding Hounsfield unit (HU) value is therefore given by,

$$\mathrm{HU} = \frac{\mu_x - \mu_{water}}{\mu_{water} - \mu_{air}}\, x\, 1024\,; \qquad (4)$$

where μ_{water} and μ_{air} corresponds to the linear attenuation coefficients of water and air, respectively. Water has an attenuation of 0 HU while air is -1024 HU, cranial bone can reach 2000 HU or more at standard temperature and pressure (STP). The attenuation of the metallic implants (eg. titanium, iron etc) depends on the atomic number of the elements used.

In 1917, Johann Radon provided a formula for the Radon transformation and inverse transformation of the data acquisition in three dimensions. In mathematics, the Radon transformation in two dimensions is the integral transform consisting of the integral of a function over straight lines. Radon transformation is widely applicable to the tomography to create an image from the scattering data associated to the cross-sectional scans of an object. The Radon transform data is often called a sinogram because the Radon transform of a Dirac delta function is a distribution supported on the graph of a sine wave. Furthermore, the inverse of the Radon transform can be used to reconstruct the 3D image of unknown density from the scattering data projection in 2D as depicted in Fig. 2.4, and thus it forms the mathematical underpinning for tomographic reconstruction in CT scan as discussed below.

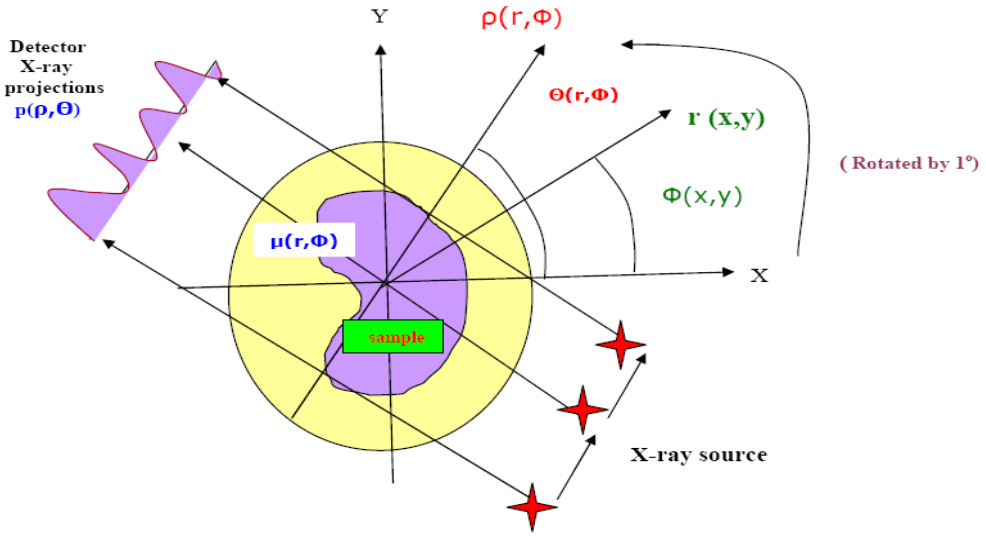

Fig. 2.4 The diagram presents a general schematic of a 3D image reconstruction in the CT scan by employing the transmission tomography. All the notations have their usual meanings.

The Fig. 2.4 shows that the spatial information in each pixel of the region of interest (ROI) can be accumulated as 2D sinograms as raw data or projection, p (ρ,θ) in each scan. Furthermore, the convolution of the Fourier transformation of these 2D sinograms with the high pass filter yield the projection information by isolating the blurs from the image in the frequency domain.

The information of the attenuation coefficients can be stored in discrete elements using the FBP technique and the central slice theorem in momentum space. The complete information of the 3D image data can be acquired by scanning the sample in each unit of translations and rotations of the source-detector pair through 180^{o} in all 2D planes along the z-axis. Eventually the reconstructed image can be retrieved in the spatial domain following the inverse Fourier transformation of the projection data stored in the momentum space.

Localized attenuation coefficients (μ(r,ϕ)) can be computed in the spatial domain by using the most common FBP algorithm, and it can be expressed in terms of inverse of radon transformation as,

$$\mu(\mathrm{r},\phi) = \int_0^{\pi} \int_{-\infty}^{\infty} \left\{ \int_{-\infty}^{\infty} |\mathrm{K}| \mathrm{P}(\mathrm{K},\theta).\exp(\mathrm{i}\mathrm{K}\rho)\,.\,\delta[\mathrm{r}\cos(\varphi-\theta)-\rho]\,\mathrm{dK} \right\} \mathrm{d}\rho\mathrm{d}\theta; \quad (5)$$

where |K| is the inverse filter to minimize the noise due to the star blur (1/r) by using filtration in the reconstructed image. Similarly localized attenuation coefficients (μ(r,ϕ)) in the spatial domain can also be derived using the faster CBP algorithm as given below,

$$\mu(r,\phi) = \int_0^{\pi} \int_{-\infty}^{\infty} \{p(\rho,\theta).\,\mathrm{F}^{-1}|K|\}\,\delta[r\cos(\varphi-\theta)-\rho]d\rho d\theta\,; \quad (6)$$

by using the convolution of momentum vector (K) and projection, *P(K,θ),* in the frequency domain as given below,

$$p(\rho,\theta).\mathrm{F}^{-1}|K| = \int_{-\infty}^{\infty} |K|P(K,\theta).\exp(iK\rho)\,.dK; \qquad (7)$$

where the ρ and K are the translational and momentum vector co-ordinates in spatial and frequency domains respectively, θ is the angle of rotation of the source-detector pair in spatial and momentum space, and (r,ϕ) is the spatial coordinates of each point pixels in CT image. Table 2.1 presents the linear attenuation coefficients for some typical biological components using the CT-numbers (Hounsfield unit) of the pixels in the CT scan images. The coefficients are normalized to that of water at the typical energy region of 30~140 keV.

Table 2.1 The computed values of the mass attenuation coefficients of the various components in the computed tomography (CT) scan.

Components	Material Density (ρ gm/cc)	Mass attenuation coefficients (μcm^2/gm;100 keV)	CT (HU) number at 100 keV	Mass attenuation coefficients (μ cm^2/gm; 1 / 6 /10 MV)
Fat/ tissue	0.91-1.06	0.1589 / 0.1693	-100/(50-70)	0.0701/ 0.0274 /0.0219
Dry Air	0.00129	0.1541	-1000	0.0636/ 0.0252 /0.0204
Bone	1.10-1.92	0.1855	300-3000	0.0657/ 0.0273 /0.0231
Water	1.00	0.1707	0	0.0707/ 0.0277 /0.0222
Blood	1.06	0.1695	40	0.0701/ 0.0274 /0.0220
Lung (tissue)	0.33(1.05)	0.1695	- (300-800)	0.0701/ 0.0275 /0.0220
A-150 plastic	1.12	0.1680	35	0.0699/ 0.0269 /0.0212

2.4 Computed tomography and positron emission tomography

More commonly, a technique much like the reconstruction of CT and single photon emission computed tomography (SPECT) data is used in the emission tomography in the PET

scan. PET scans are increasingly read alongside CT or MRI scans, and the co-registration of both anatomic and metabolic information.

The near-simultaneous detection of non-interacting annihilation photons registers the tens-of-thousands of coincidence events occurring in the PET scanner. A set of simultaneous equations can be solved to determine the total activity of each bit of tissue along many lines of responses (LORs) using the time-of-flight (TOF) of the non-interacting photons and the scanners with better time resolution. TOF determines the difference in real time between the detection of two photons passing through each LOR. Thus a map of radioactivity as a function of location for the bits of tissue or voxels may be constructed and plotted using the raw data registered for each coincident event. The resulting map shows the tissues in which the molecular probe has become concentrated, and can be interpreted by a nuclear medicine physician in the context of the patient's diagnosis and treatment plan.

Coincidence events can be grouped into projection images or sinograms. The sinograms are sorted by the angle of each view and tilt, the latter in 3D case images. The sinogram images are analogous to the projections captured by CT scanners, and can be reconstructed in a similar way. However, the statistics of the data is much worse than those obtained through transmission tomography. A normal PET data set has millions of counts for the whole acquisition, while the CT can reach a few billion counts. As such, PET data suffer from scatter and random events much more dramatically than CT data does.

Iterative expectation-maximization algorithms are now the preferred method of reconstruction over FBP reconstruction in PET scan to improve the image. The advantage is a better noise profile and resistance to the streak artifacts, but the disadvantage is higher computer resource requirements. Since different LORs must traverse different thicknesses of tissue, the

photons are attenuated differentially. The result is that structures deep in the body are reconstructed as having falsely low tracer uptake. Thus various corrections are necessary in practice prior to the final processing of the data for PET image reconstruction such as correction for the random coincidences and scattered photons, detector dead-time correction, and correction for the angular and inherent detector-sensitivity.

Modern PET/CT dual modality scanners can estimate attenuation using integrated X-ray CT equipment with the PET scanner. While attenuation-corrected images are generally more faithful representations, however, the correction process is itself susceptible to significant artifacts. As a result, both corrected and uncorrected images are always reconstructed and read together.

Early PET scanners had only a single ring of detectors; hence the acquisition of data and subsequent reconstruction was restricted to a single transverse plane. More modern scanners now include multiple rings, essentially forming a cylinder of detectors. There are two basic approaches to reconstructing data from such a scanner: 1) 2D reconstruction where images are generated from the coincidences within each separate ring of detectors, and 2) 3D reconstruction that takes into account of the coincidences within rings and between rings, then reconstruct the entire volume together. 3D techniques have better photon sensitivity and therefore less noise, but are more sensitive to the effects of scatter and random coincidences, as well as requiring correspondingly greater computer resources. The advent of sub-nanosecond timing resolution detectors affords better random coincidence rejection, thus favoring 3D image reconstruction.

2.5 Positron emission tomography phantom volume delineation

PET/CT dual-imaging modality is one of the most reliable non-invasive diagnostic imaging techniques. PET employs molecular functional imaging techniques using various types of radiotracers such as 18-Fluoro-deoxyriboglucose (18-FDG). The PET scan is the only tool that

identifies chemical and metabolic changes in the human body. Nevertheless, the uncertainty in travel time and the length of the positron from the origin to the event site, and a tradeoff between spatial resolution and the photon sensitivity in PET scan always limits its application. Thus researchers have attempted to estimate the correct dimensions of the metabolic target volume (MTVs) in various types of PET phantom volume measurements. This information provides guidance for the precise volume delineation in the radiation therapy treatments in cancer [7].

Static and moving phantoms were primarily used in the experiments performed by various researchers at different institutions. Spherical and cylindrical phantoms made up of acrylic plastic materials (eg. NEMA-IEC phantoms; Jaszczak phantoms**),** were typically used in the measurements as shown in Fig. 2.5.

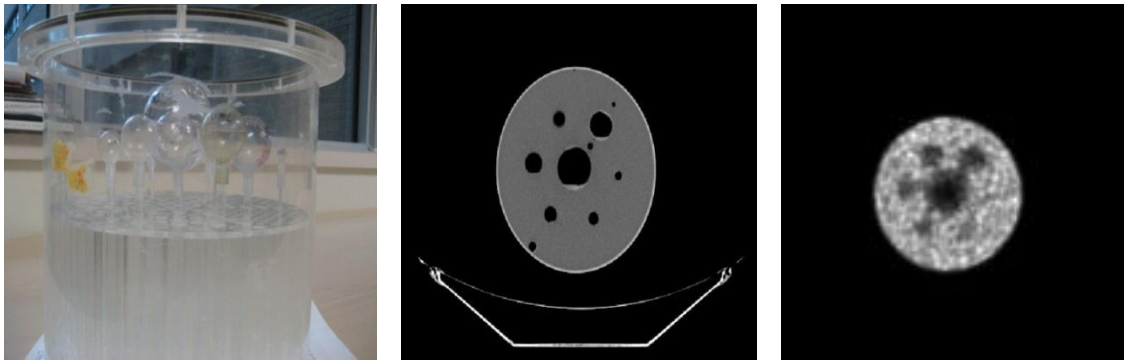

(a) (b) (c)

Fig. 2.5 Demonstration of PET phantom volume measurements: (a) 10 hollow spherical inserts in cylindrical tank with relative activity density of (0.29 μCi /cc) of 18-Fluoro-deoxyriboglucose (18-FDG) in the cylindrical tank (F-18 Jaszczak phantom), (b) CT images for cold spheres, and (c) PET imaging of a typical slice of phantom series. Courtesy of VCU Radiology Department.

The target-to-background activity ratios (SBRs) were found to be 1.5:1 to 14.7:1 in the spherical phantom volume measurements. The true diameters of the spherical phantoms were

ranging from 4.4 to 82.2 mm (0.04 to 290.7 cm^3). Measurements were performed in various types of 18FDG-PET scanners such as Discovery (ST, LS; GE Med. Systems), Advance (GE Med. Systems), C-PET plus (Philips Med. Systems), and Exact HR (Siemens Med. Systems).

Non-iterative methods such as FBP and CBP, iterative reconstruction methods such as ordered subset expectation maximization (OSEM), and the Fourier rebinning (FORE) algorithms were basically used in the image reconstruction process. The volumes of various ROIs were precisely measured using the simple threshold techniques, iterative threshold segmentation, the standardized uptake value (SUV)-based methods, and the edge detection methods.

A more practical range of threshold was approximately 28% to 65% for both static and dynamic phantom volume delineations in such experiments. However 50% and 40% threshold intensities were reported to be the optimal choice in various literatures for small and large size MTV delineations for the static organs respectively as shown in Fig. 2.6 (a).

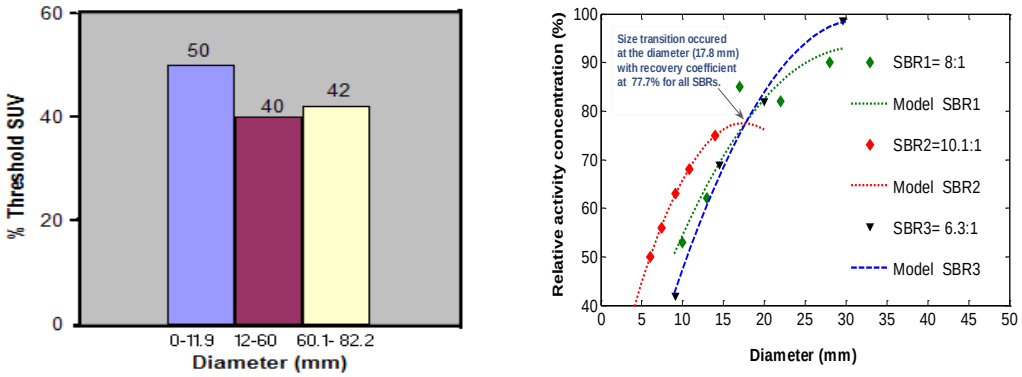

(a) (b)

Fig. 2.6 (a) Selection of the relative threshold standardized uptake value (SUV) for the metabolic target volume (MTV) delineations in the static organs (eg. head and neck structures), and (b) recovery coefficients for the spherical phantom volume delineations at three different source to background activity ratios (SBRs) at threshold transitions (40-50%) for the 18-Fluoro-deoxyriboglucose (18-FDG) radiotracers as reported in various literatures.

The intermediate size of PET MTV was analytically determined to be 17.8 mm of the phantom size at recovery coefficient of 78% for various SBRs for the spherical phantoms in various studies as shown above in Fig. 2.6(b). Furthermore, phantom volumes less than 6.4 cm^3 were found to be more sensitive to threshold changes. The threshold for the PET-positive volume as a function of the intensities of tumor and background were typically found to be an intermediate size between the volume at SUV of 2.5 and the volume with a 40% (50%) threshold for the larger (smaller) size of MTVs as shown in Fig. 2.7. Lower thresholds were found to be better for non-static and larger size organs. Higher threshold levels were more accurate at high resolution reconstruction. Higher tumor to background activity ratio yields lower discrepancies.

In SUV based method, the SUV value should not be just a constant (e.g. 2.5), but as a function of tumor size. It shows that PET scan would be useful for the precise quantification of the tumor volume with a typical size of diameter greater than 1cm due to its limited spatial resolution and low radio-sensitivity. However, it can also provide some important information on shape and size of the small tumors if appropriate corrections (eg. recovery coefficients) can be made in the measurements. It can be argued that the combination of various techniques of PET phantom volume measurements for appropriate size and shape of tumor targets could be useful to determine a universal mechanism for PET MTV delineations in radiation therapy treatments.

The appropriate PET volume delineation methods include the edge detection and threshold methods with better correlations of tumor to background uptake ratio and tumor size. Since the image characteristics are the product of detector technology and image processing methods including reconstruction algorithm, a selected method for PET volume delineation for the precise diagnosis of the disease should be validated prior to the implementation. The accurate target volume delineation based on the functional metabolism is useful to the radiotherapy treatments.

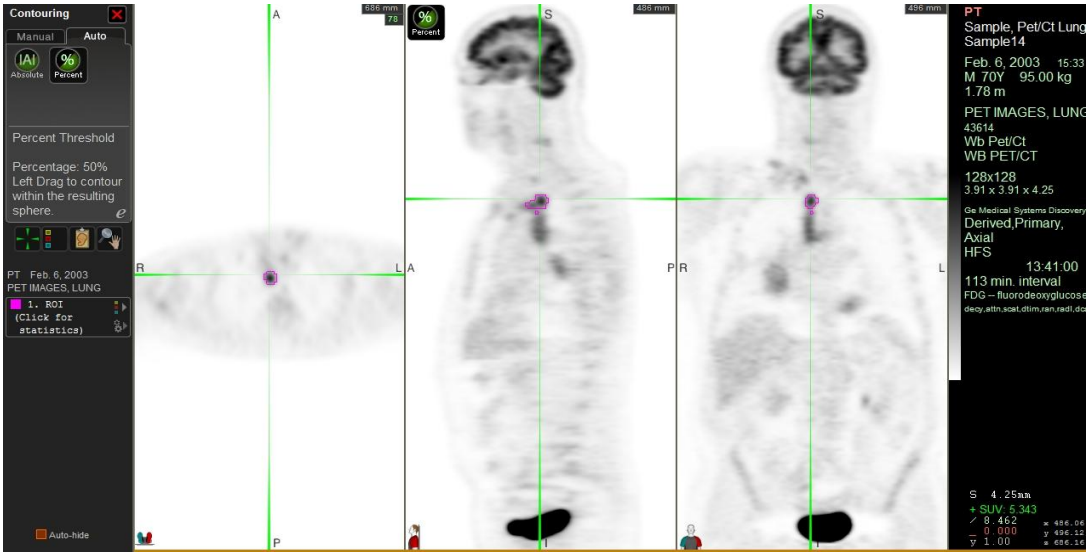

(a)

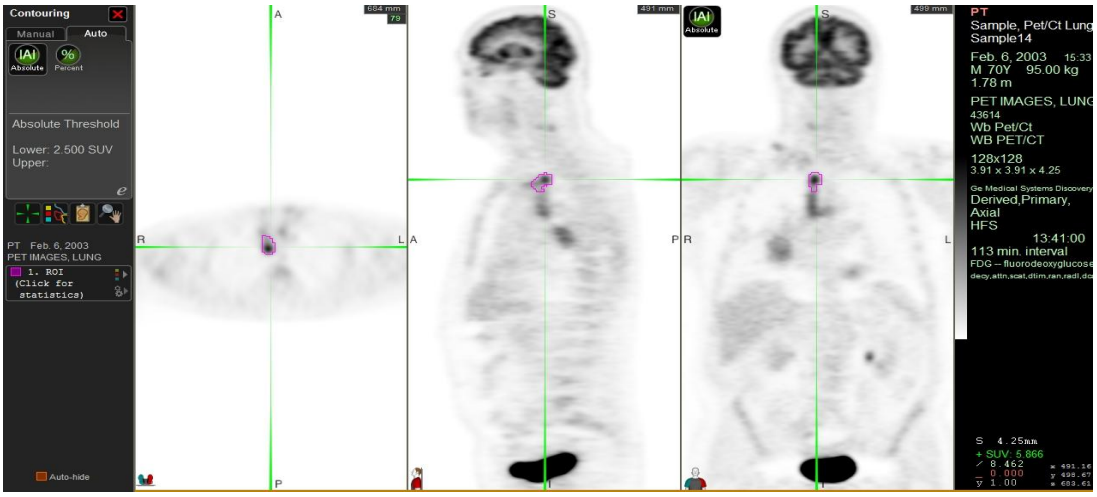

(b)

Fig. 2.7 Demonstration of positron emission tomography (PET) tumor volume delineation by contouring the target at (a) 50% threshold of maximum standardized uptake value (SUV) index, and (b) SUV (2.5) techniques. Typically 5-10 mCi /10mg of 18-Fluoro-deoxyriboglucose (18-FDG) is injected intravenously for a complete whole body scan. Courtesy of Nuclear Medicine Group, Rhode Island Hospital, Providence, RI.

2.6 Tape/Network exchange specification and Radiation Therapy Oncology Group

RTOG, founded in 1968, is a national clinical cooperative group that explores the optimal treatment methodologies in cancer. Radiotherapy treatment planning (RTP) system imports the treatment parameters in radiotherapy treatments using RTOG and digital image communication (DICOM) image formats. Since RTOG format does not include the conversion of CT number to the electron density, a correlation curve for the pixel values to the electron density is used to compute the 3D dose distribution in the RTP system. CT images are stacked in a set of RTOG or DICOM format of files. RTOG is limited to transverse only images in the CT scans.

NCI has developed a new Tape/Network specification in the RTOG format to support the digital image data transfer system in radiotherapy applications. These new image types include the information on CT scans, beam geometries, collimator angles, beam positions, digital reconstructed radiographs (DRRs), 3D dose matrix, outlined structures and DVHs. This specification utilizes (a) Local right-handed Cartesian co-ordinate system of the patient (PCS), and (b) a 2D "beam's-eye view" (BEV) co-ordinate system (BCS). The z axis always points toward the patient's feet in the local PCS as shown in Fig. 2.8 [8].

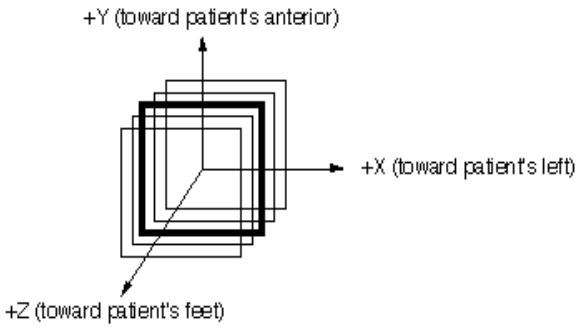

Fig. 2.8 Figure illustrates the local coordinate system (PCS) of a patient who is scanned head first in a supine position. The X and Y coordinate axes are tied to a treatment couch with +X to the right of the gantry when viewed from the couch and +Y is up toward the ceiling. The +Z coordinate is always toward the patient's feet independent of their treatment orientation.

Two types of data can be stored on tape: BINARY data, for CT scans and digital film images; and ASCII character strings for discrete images and the directory files. Patient image pixel numbers are positive in the range 0 to 32767 for 16 bit square pixels in the CT image, and 0 to 255 (32767) for 8 (16) bit square pixels in MRIs and ultrasound images.

Generally the origin of the PCS is at the dead center or iso-center of the CT/MRI/ultrasound images. However, offsets of the images are permitted as indicated in the following Fig. 2.9.

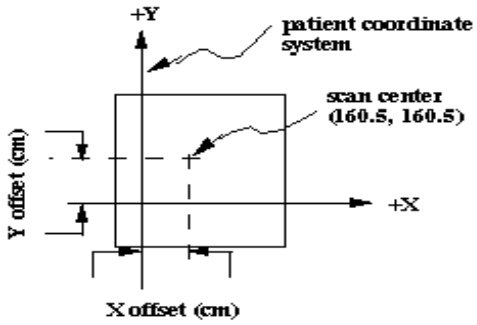

Fig. 2.9 Offset corrections in the patient co-ordinate system (PCS) in the computed tomography (CT) scan.

CT/MRI/ultrasound scans are connected in contiguous order of monotonically increasing value of the z-coordinate in PCS. The upper left hand corner pixel (least x, greatest y) is first, followed by pixels in the first row, followed by the subsequent rows of lesser y value until the bottom right (greatest x, least y) pixel terminates the array. Furthermore, the structures are connected as sequences of 3D coordinates to define the ROIs on tape. All the points are grouped together in successive planes on which CT scans are centered. Within a given plane, a structure will consist of one or more "segments". Segments in contiguous scans are connected in some way to form the surface of the volume on tape [8] as shown in Fig. 2.10.

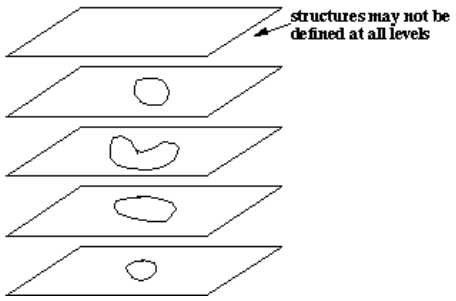

Fig. 2.10 Components of a structure contoured in a localized patient coordinate system (PCS) in three dimensional computed tomography (CT) scan image.

Beam geometry's are to be transferred as one data file per beam with the data file containing the information of the defining beams and its aperture, and the dose fractionation scheme. The format includes the grouping of all beams utilized in the treatments, so that a composite of all treatments may be reconstructed by taking into account of the cumulative dose fractionation for the total treatment fields. Similarly the origin of the BCS is defined with the treatment machine's collimator rotated to the neutral position and the gantry angle set such that the beam is pointed to the floor (down) as shown in Fig. 2.11. All collimator, gantry and couch angles are defined to be zero for the gantry pointed down. Beam shapes may be specified by MLC settings, contours for the custom portal blocks. Furthermore, the data in the image file contains coordinate of machine iso-center (in cm) in the PCS, collimator settings for the x jaws and y jaws respectively.

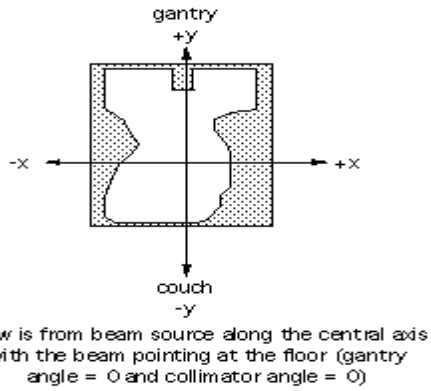

Fig. 2.11 Beam's eye view (BEV) frame of reference.

The film coordinate system of the digital images is identical to that used for the beam geometry images with respect to the x and y offsets and axes. The DRR digital film image is assumed to be aligned with the un-rotated collimator. The integrity of the right-handed Cartesian coordinate system is preserved using a standard sign convention in sagittal and coronal planes. The coordinates for single planes as presented to the observer are as shown in Fig. 2.12.

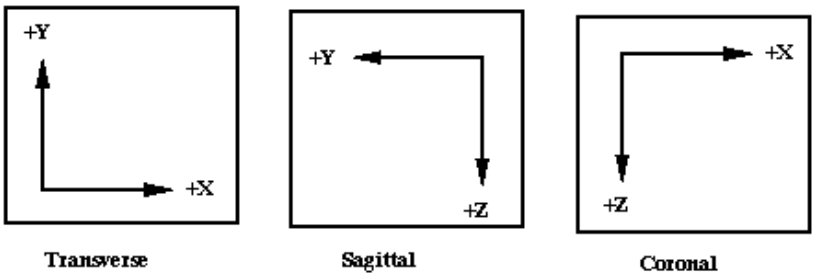

Fig. 2.12 Right hand coordinate system employed in 3 different views of the computed tomography (CT) scan: Transverse, sagittal, and coronal images

A dose distribution is the result of a calculation of dose at one or more points throughout the ROIs in the anatomy, for a particular configuration of beams in a specific treatment plan. Furthermore, DVHs account for the 3D dose distribution in the corresponding structures. DVHs are typically transferred as one structure per image file.

Chapter III

Radiation therapy treatment

3.1 Radiation therapy and adjuvant systematic treatments

Radiation therapy is one of the three principal modalities in the treatment of cancer, the other two being surgery and chemotherapy. Adjuvant systemic therapy (eg. chemotherapy, immunotherapy, hormonotherapy) and radiotherapy are often administered following the primary treatment as surgery to improve the disease-specific problems and the overall survivality of the patients. Typically, chemotherapy is concurrently administered at lower dose to make the cancer cells more sensitive to the local treatment using radiations. Only three types of cancers efficiently respond to chemotherapy such as testicular cancer, some lymphomas and leukemias. It has not yet proven useful in treatment of the metastasized breast, lung, pancreas, and prostate cancers.

Adjuvant hormonal therapy is given after prostate removal in prostate cancer. In breast cancer, adjuvant therapy may consist of chemotherapy, radiation therapy, and the hormonal therapy following the lumpectomy. Adjuvant chemotherapy has been proven successful in the treatment of early stage breast cancer, liver cancer, testicular and ovarian cancers. In early stage one small cell lung carcinoma, adjuvant chemotherapy and adjuvant radiotherapy is administered to either the lung to prevent a local reoccurrence, or the brain to prevent the metastases.

Depending on what form of treatment is used; adjuvant therapy can develop side effects and complications in the normal tissue organs, like all therapy for neoplasms. Chemotherapy frequently causes vomiting, nausea, mucositis, and acute myeloid leukemia. Radiotherapy causes

radiation dermatitis and fatigue, and depending on the area being irradiated, may have other side effects. For instance, radiotherapy to the brain can cause memory loss, headache, and radiation necrosis. If the abdomen or spine is irradiated, nausea, vomiting, diarrhea, and dysphagia can occur. If the pelvis is irradiated, various complications like prostitis, diarrhea, and abdominal pain can occur. Adjuvant hormonal therapy for prostate cancer may cause cardiovascular disease, and other, possibly severe, side effects. These risks may outweigh the risk of reoccurrence of the primary tumors following the treatments of various types of cancers.

3.2 Conformal radiation therapy

The goal of radiation therapy is to eliminate cancerous cells within a patient tumor volume while minimizing the damage to the normal tissues and critical organs. It is essential to localize the tumor accurately in order to achieve an effective treatment. The process with which the treatment dose is tailored to a tumor target while sparing normal tissue is generally referred as the conformal radiation therapy (CRT).

The target volume delineation involves the use of accurate 3D patient image sets, observation, palpation and surgical findings. In fact, high quality CT image sets can be used to ensure the reliable clinical tumor volume delineation, and to define the treatment volumes in the radiotherapy plans. Clearly, a convention for defining tumor volumes, accurate CT image sets, advanced beam collimation techniques, and the accurate dose calculation algorithms are essential in meeting the goal of the advanced CRT techniques such as 3DCRT and IMRT.

3.2.1 Volume definitions in radiation therapy treatments

The ICRU Reports 50 and 62 have recommended specifications for prescribing, recording and reporting standard volumes and doses for most clinical radiotherapy treatment situations [9,

10]. Report 50 specifies a number of physical volumes that are to be defined prior to, and referenced during the treatment planning as shown in Fig. 3.1. The Gross Tumor Volume (GTV) is defined as the gross palpable or visible quantity of malignant growth with high tumor cell density. Therefore, an additional volume is defined as the Clinical Target Volume (CTV) to include other associated microscopic effects. CTV consists of a tissue volume that contains a demonstrable GTV and subclinical microscopic malignant disease. Both GTV and CTV must be treated adequately in order to achieve the aim of therapy. Throughout the treatment process the position and shape of the CTV should ideally be constant with respect to a common fixed coordinate system.

Furthermore, an Internal Margin (IM) is added to the CTV to compensate for expected physiological movements and variations in tumor size, shape, and position during treatment. To distinguish the volume enclosed by the CTV surface plus an IM, from that of the Planning Target Volume (PTV), an intermediate volume is defined as the Internal Target Volume (ITV) [11]. Thus Internal Target Volume (ITV) is defined as the volume that includes the irregular surface of the CTV, and the high risk and low risk lymph nodes with respect to the common fixed coordinate system. However, the tumor size may change during the course of treatment, and the tumor volume subjects to the internal movement. In addition, patient position variations may occur during treatment set-up and delivery. To address the geometric uncertainty due to the tumor movement and patient set-up, Report 50 defines the exterior contour, PTV, as a geometric concept used to select the appropriate beam size and orientation; taking into consideration of the net effect of all possible geometric variations. Accounting for all geometric variations ensures the prescribed dose (PD) is actually distributed throughout the CTV. PTV can therefore be envisioned as a static, geometric volume used only for the treatment planning.

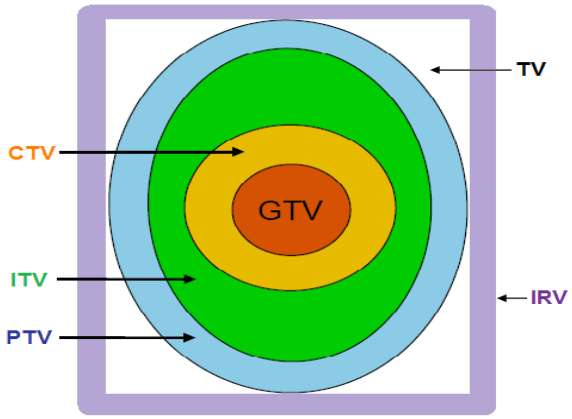

Fig. 3.1 Schematic diagram showing the various volumes in the radiation therapy treatment as defined in ICRU Report 50. The inner most region is defined as the Gross Tumor Volume (GTV) followed by the Clinical Target Volume (CTV), Internal Target Volume (ITV), Planning Target Volume (PTV), and the Treated Volume (TV), and the external Irradiated Volume (IRV).

Other volumes specified in Report 50 are the Treated Volume (TV) and Irradiated Volume (IRV): the former defined as the volume enclosed by an isodose surface selected by the radiation oncologist, and the later defined as the volume irradiated to a dose considered significant in relation to the normal tissue tolerance.

As a supplement to Report 50, ICRU published Report 62 to formulate more accurate definitions related to volumes, margins, organs at risk (OARs), dose variations, and uncertainties that result from the technological advances in clinical imaging and treatment precision. Report 62 clearly specifies two independent coordinate systems such as one associated with the patient position (internal) in the imaging system and the other in treatment unit (external), and two reference points that are to be used in combination. The coordinate systems co-relate the positions of tissues, organs and volumes in the patient with the position and orientations of the beams used for the imaging and therapy.

In conjunction with accurate patient set-up during imaging and therapy, ICRU Report 62 defines the Internal Reference Point (IRP) as the point used for localization of GTV or CTV with respect to anatomical landmarks. The External Reference Point (ERP) is defined as palpable or visible points located on or near the surface of the body or on the surface of an immobilization device. A Set-up Margin (SM) is incorporated to account for patient position, mechanical, and dosimetric uncertainties with respect to the external set of coordinates. The SM is added to the ITV to give the revised PTV previously defined in Report 50. In fact, an OAR is any normal tissue whose radiation sensitivity may significantly influence the planning or the PD where the resulting Planning Organ at Risk Volume (PRV) is included to the account for any movements of the OAR volume during treatment.

3.2.2 Modern techniques in conformal radiation therapy

CT image data can provide high quality anatomic information that, in turn, can be used to reveal the accurate location of the tumors and organs in CRT [12]. Knowing the precise location of the three dimensional tumor volumes, clinicians define the relevant ICRU volumes with increased confidence. To achieve the desired outcome of therapy, treatment fields should be made to conform to the tumor volume while sparing the critical structures using appropriate beam collimation techniques [13]. Allowing multiple beams with varied orientations may provide sharp margins around the target. As each treatment field is made to conform to the PTV, delivered dose may be escalated to produce a greater biological effect. Khan [14] adds that in the design of conformal fields, sufficient margins must be given between the PTV and any field boundary to ensure adequate coverage. With sufficient margins, PTV dose can be made to incorporate cross-beam profile penumbra and lateral radiation transport as a function of depth, radial distance and tissue density.

Webb [15] broadly divides CRTs into two categories: those which employ geometric field shaping alone and those which also modulate the fluence intensity across the geometrically-shaped field. Throughout this work, geometric field shaping techniques using customized blocks, wedges and multi-leaf collimators (MLCs), will be referred to as 3DCRT, whereas techniques that incorporate modulated fluence intensities will be referred to as IMRT as discussed below.

3.2.2.1 Three-dimensional conformal radiation therapy

For most deep seated tumors, a realistic tumor dose can only be achieved by using a combination of several beams. Conventional 3DCRT treatment planning is forward planning based and manually optimized. In fact, acceptable isodose distributions are generally achieved using a combination of therapy beams with appropriate energy, size, weighting and gantry angle in such techniques. Beam shaping has traditionally been achieved through the use of alloy blocks individually made to collimate each field to a specific shape. The blocks are placed in a tray attached to the machine head and must be changed for each field.

An alternate approach to collimating conformal therapy beams was developed by Takahashi [16]. This method uses a large number of rectangular wedged fields, each at different gantry angles, made to approximately conform to the target volume. The total dose distribution that results from this method can be made to produce a high tumor dose. However, this method is limited by the rectangular beam collimation and therefore is not truly conformal. A typical conformal treatment uses 3 to 5 fields, therefore, the time required to prepare and set-up the collimating blocks can become considerable. Thus MLC field shaping is a more practical approach to achieve the conformal photon beam in radiotherapy treatments.

Today, 3DCRT generally refers to the multi-field treatments, where each field is shaped using a MLC. In general, beam shaping is accomplished in the following manner:

- Accelerated electrons strike a tungsten target producing a shower of high energy photons.
- A fixed primary collimator first attenuates all but the forward-directed bremsstrahlung cone.
- In absence of flattening filter, the cone beam passes through a parallel-plate ionization chamber. The resulting ionization current is used to monitor and control the machine output.
- The beam next passes through a set of motorized tungsten blocks that reduce the circular cross section of the cone to a rectangular field circumscribing the desired field shape.
- Finally, the individual leaves of the MLC are set to the boundaries of the desired field shape.

MLCs are clinically the most sophisticated method for generating arbitrary shaped radiotherapy fields, yet the utility of MLC collimation is not restricted to just conformal treatments. Fig. 3.2 presents a simple diagram for the generation of photon and electron beams using a clinical linear accelerator (Clinac). Inherent objectives for a 3DCRT treatment plan are to use beam directions such that the irradiation of the OARs is minimized so as to reduce normal tissue complications, and to ensure adequate dose coverage of the PTV.

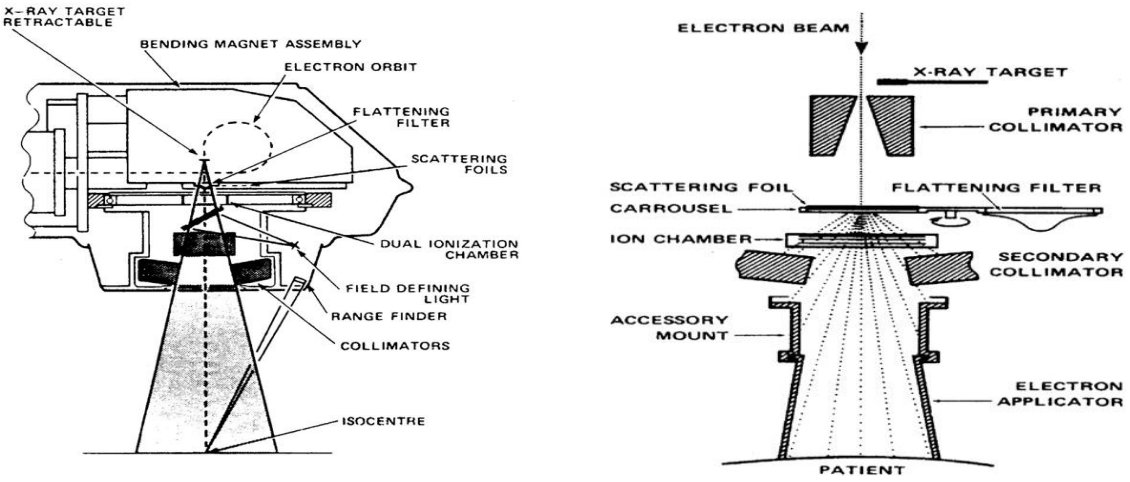

Fig. 3.2 General schematics of a clinical medical linear accelerator (Clinac): (a) X-ray production using tungsten target in conformal radiation therapy (CRT), and (b) generation of intense electron beam in electron beam therapy (EBT).

3.2.2.2 Intensity modulated radiation therapy

It is necessary to allow full freedom in the shape of the delivered beams both with regard to beam energy, beam direction and beam profile for the efficient radiotherapy treatment. Freedom in beam profile implies modulation of the beam intensity across each field [17]. Traditional CRT techniques use field intensities that are either uniform or change uniformly using wedge filters whereas the intensity profile of a modulated field can produce non-traditional fluence maps. Bortfeld et al [18] frames the problem of optimizing the dose distribution for the CRT with the intensity modulated external beams, analogous to the reconstructing of a 3D image from its 2D projections, as demonstrated in Fig. 3.3. It was suggested by Webb [15] that only about 30% of clinical problems requires the use of IMRT treatments.

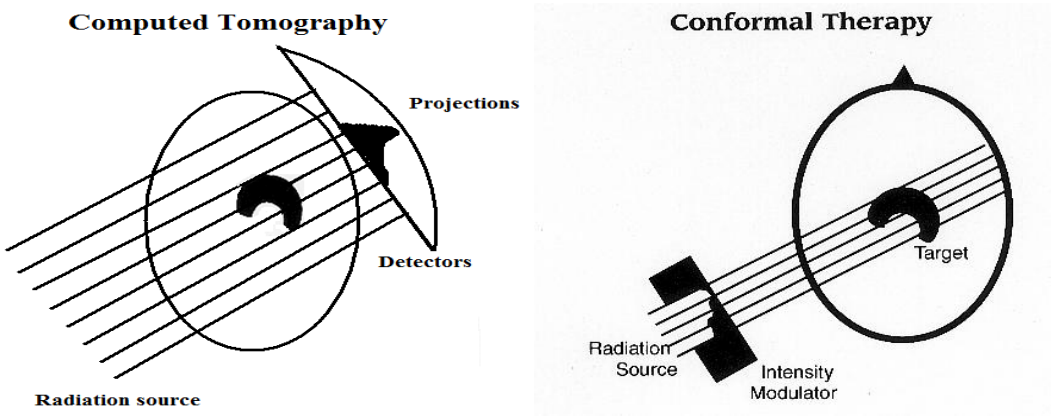

Fig. 3.3 Image demonstrates how optimizing the dose distribution for the conformal radiation therapy (CRT) with the intensity modulated external beams is similar to the problem of reconstructing a 3D image from its 2D projections in computed tomography (CT) scan [18].

There are two general methods used to produce the IMRT beams shaped with MLCs. The first is to use a series of discrete conformal fields or field segments each located at the same gantry angle. The treatment machine is turned on to give a conformal dose for the first field.

Each pair of multi-leaves are then moved to a set of different positions. This produces a new conformal field and the machine is once again turned on. This results in a series of fractional conformal doses given at that same gantry angle. The total dose is therefore the sum of the fractional doses delivered through each conformal field and results in a modulated dose distribution. This technique is referred to as step-and-shoot intensity modulation and finds many applications in radiotherapy. Fig. 3.4 shows four different conformal fields used in an example step-and-shoot treatment [19]. A second IMRT technique used in radiotherapy is a dynamic method where the leaves are moved while the treatment machine is on; this is referred to as dynamic multi-leaf collimation (dMLC) technique. Having the fluence intensity modulated as a dynamic process does pose a number of difficulties.

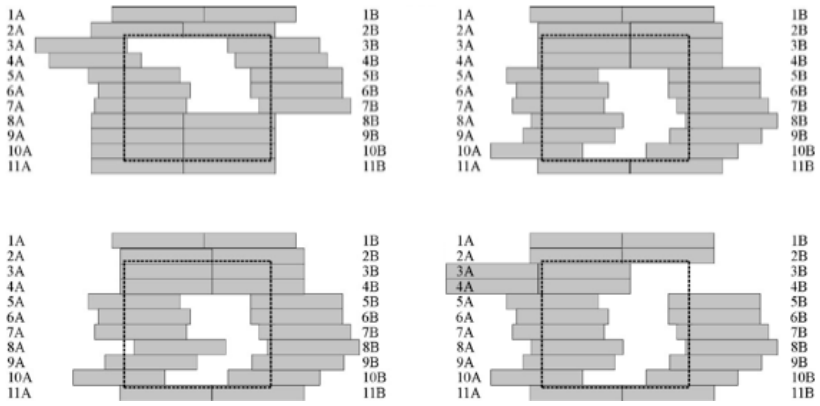

Fig. 3.4 Shown are the four multi-leaf collimated fields used in step-and shoot intensity modulated radiation therapy (IMRT) treatment techniques [19].

Due to the large number of beamlets, weight optimization becomes impossible in IMRT using forward planning method. IMRT field intensity optimization process employs the inverse treatment planning method. Fully optimized IMRT requires automatic, computer-generated optimization of beam weights and optimal parameters for the field segmentation using MLCs.

One of the key requirements in IMRT is to interpret the desired intensity modulation into a set of instructions used to drive the leaves across the treatment field using appropriate algorithms such as direct machine parameter optimization (DMPO) algorithm. A simple solution for calculating the leaf positions as a function of time was presented by Khan [14], and Boyer and Strait [20]. This method relates the desired beam intensity to the velocity of each leaf-pair. This is a very intuitive solution that assumes the leading leaf is moving at the maximum possible velocity and varies the velocity of the trailing leaf to produce the desired intensity modulation.

In general, IMRT optimizes weights assigned to the individual rays of the beam (beamlets) by coordinating with the leaf-pair in MLCs. The control of individual rays allows IMRT to produce desirable dose distributions in ROIs in CT scans. The objective function constrained by the PD to the target volume and OARs, requires being minimal. As it is impossible to deliver negative dose, there are restrictions on the parameters used in optimizing beam weights that produce modulated field intensities. Intensity modulation of the beam across each field can result in an inhomogeneous dose distribution within the tumor volume. However, De Meerleer [21] and other scientists noted that the use of inhomogeneous dose distributions may provide a higher dose to the tumor without increasing normal tissue doses.

3.3 Dose tolerance of the serial and parallel organs

As we stated earlier that the goal of radiotherapy is to completely eliminate cancerous cells within a patient tumor volume while minimizing the damage to the normal tissues. A knowledge of the tolerance dose ($TD_{50,5}$; 50 percentage chance of complications reported in the normal organs in the past 5 years) for the normal tissues is essential for the safe practice of radiotherapy treatments of various types of cancers. Table 3.1 presents the summary of the $TD_{50,5}$ of the major critical organs contoured in the radiotherapy treatment of various types of cancer respectively.

Table 3.1 A list of normal tissue tolerance dose ($TD_{50,5}$) of the large volume fractions (>2/3) of the critical organs published in various articles, for the radiotherapy treatment of various types of cancer using the conventional hyperfractionation dose-rate of 1.8-2.0 Gy in once a day (QD).

Structures	**$TD_{50,5}$ (cGy)**	**$TD_{50,5}$ (cGy)**	**$TD_{50,5}$ (cGy)**	**DVH constraint (cGy)**
	Emami et al, 1991; [22]	Kehwar et al, 2005; [23]	Luxton et al, 2008; [24]	Clinical guidelines for the normal tissue organs*.
Brainstem	6500	6656	6500	5400
Spinal cord	-	7162	6650	D_{Max} < 5000
Parotid gland	4600	5172	4600	D_{Mean}< 2000
Brain	6000	6868	6000	7200 (partial volume)
Cochlea	6500	6725	6500	D_{Mean}< 4500
Optic chiasm	6500	8457	6500	D_{Max} < 5500
Mandible	7200	7858	7200	D_{Max} < 7000
Esophagus	6800	7207	4700	5000
Larynx (Edema)	8000	8813	8000	D_{Mean} <4400; D_{Max}< 6600
Combined lung	2450	3702	2450	D_{Mean} < 2300
Heart	5000	4818	4800	6000
Rectum	8000	8393	8000	7500
Bladder	8000	8649	8000	8000
Femoral Head	6500	6370	6500	5000
Submandibular gland	-	-	4600 [25]	D_{Mean} < 3500
Constrictor	-	-	5000 [26]	D_{Mean}< 5000
Oral-cavity	-	-	-	D_{Mean} < 5000
Larynx (Neocrosis)	8000	7925	7000 [24]	

* Mean dose = D_{Mean} ; Maximum dose = D_{Max} ; NMH based treatment criteria

The relative volume of the organ irradiated to certain dose levels is used to predict the probability of occurring serious complications in the normal organs in such treatments. In general, the dose-volume relationship will differ for each organ and will generally be a mix of two extreme cases: (a) critical dose (element) limit, and (b) the critical volume limit that leads to the certain known endpoints. The normal tissue is constructed of functional sub-units (FSUs). The irradiation of a single FSU to a certain dose level (D_{max}) might alter the functionality of the organ and cause complications. These organs are classified under the critical dose model or as having serial architecture. Serial organs have a minimal dose-volume effect because once any of the critical elements are damaged; the function of the entire organ is impaired. Alternatively, irradiating a certain proportion of the total organ volume may be required before the functionality of the organ is impaired and complications arise. This is known as the critical volume model or parallel architecture. In the case of the parallel architecture, the FSUs are termed as tissue-rescue units (TRUs) since the organ possesses a certain functional reserve of the FSU's that assist in the repair of the functionality following partial volume irradiation. A complication might occur in such organs when a substantial fraction of the FSUs is damaged. The critical element and critical volume models are extreme cases and most organs respond to the combination of the two models. Some data are available in literature about dose constraints and volumes according to the tissue architectures, as will be discussed in Chapter 5. Mean dose and DVH analysis is the most convenient tool to incorporate such types of constraints in radiation therapy treatment plans.

Clinically, the dose-volume effect has been quantified for many organs. It has been clinically determined that the parotid glands, submandibular glands, kidney, lung, liver, larynx and bladder possesses a strong volume effect, whilst the brainstem, spinal cord, mandible, esophagus and

rectum are shown to be highly serial. However, brain and heart show the dual property. Late organ toxicity from therapeutic irradiation is a function of many confounding variables. Similarly, the effects of chemotherapy, molecular targeted agents, or any other concurrent therapy could potentially make patients more susceptible to complications from radiation, so the dose tolerance limits may need to be lowered in those cases. Many of these effects are well known for the conventional fractionation schemes. It is also worthy to note that dose tolerance limits will not have their intended benefit if the dose calculation is not accurate.

3.4 Implication of the radiobiology in radiation therapy

Radiobiology, a branch of science concerned with the action of ionizing radiation on biological tissues and living organisms, is a combination of two disciplines: radiation physics and biology. All living organisms are made up of protoplasm, and its smallest unit capable of independent existence is the cell. Cells contain inorganic compounds (water and minerals) as well as organic compounds (proteins, carbohydrates, nucleic acids and lipids) dissolved or suspended in water. The two main constituents of a cell are the cytoplasm, which supports all metabolic functions within the cell, and the nucleus, which contains the genetic information coding in DNA as shown in Fig. 3.5. A group of tissues composed of cells, together perform one or more functions as an organ. A group of organs that perform one or more functions is called an organism. Human cells are either somatic cells or germ cells. Somatic cells follow mitosis division such as stem cells, mature cells and transit cells, and germ cells follow meiosis division.

The cell proliferation cycle is defined by two well defined time periods: Mitosis (M), where division takes place; and the period of DNA synthesis (S). The S and M portions of the cell cycle are separated by two gaps G1 and G2 when, respectively, DNA has not yet been synthesized or has been synthesized but other metabolic processes are taking place. The time between

successive divisions (mitoses) is called the cell cycle time. For mammalian cells growing in culture the S phase is usually in the range of 6–8 h, the M phase less than an hour, G2 is in the range of 2–4 h and G1 is 1–8 h, making the total cell cycle of the order of 10–20 h. In contrast, the cell cycle for stem cells in certain tissues is up to about 10 days. In general, cells are most radiosensitive in the M and G2 phases, and extremely resistive in the late S phase. The cell cycle time of malignant cells is shorter than that of some normal tissue cells, but during regeneration after injury normal cells can proliferate faster. Cell death of non-proliferating (static) cells is defined as the loss of a specific function, while for stem cells and other cells capable of many divisions it is defined as the loss of reproductive integrity (reproductive death). A surviving cell that maintains its reproductive integrity and proliferates indefinitely is the clonogenic cell.

When cells are exposed to ionizing radiation the standard physical effects between radiation and the atoms or the molecules of the cells occur first and the possible biological damage to cell functions follows later. The biological effects of radiation result mainly from damage to the DNA molecules within the cell as shown in Fig 3.5.

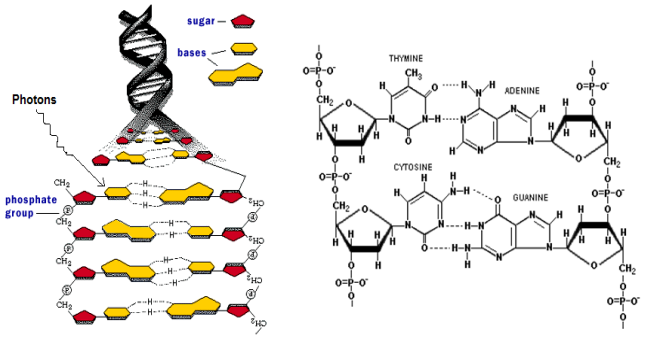

Fig. 3.5 Schematics of the indirect ionization process of the deoxyribonucleic acid (DNA) genome by oxidation of the molecules. DNA mutation can occur in various processes such as hydrolysis, deamination, alkylation and oxidation.

Double strand DNA chromosomes are the critical targets for the radiations; however, there are also other sites in the cell that, when damaged, may lead to the cell death. When directly ionizing radiation is absorbed in biological material, the damage to the cell may occur in one of the two ways: direct or indirect.

In direct action the radiation interacts directly with the critical target in the cell. The atoms of the target itself may be ionized or excited through the Coulomb interactions, leading to the chain of physical and chemical events that eventually produce the biological damage. Direct action is the dominant process in the interaction of high linear energy transfer (LET) particles (eg. proton, neutron, heavily charged ions) with biological material.

In indirect action the radiation interacts with the atoms and molecules such as water within the cell to produce free radicals, which can damage the critical targets through diffusion in the cell. In interactions of radiation with water, short lived yet extremely reactive free radicals such as the H_2O+ (water ion) and OH- (hydroxyl radical) are produced. The free radicals in turn can cause biological damage to the target within the cell by breaking the chemical bonds. It leads to the chemical changes in DNA molecules because they have an unpaired valence electron. About two thirds of the biological damage by low LET radiations such as X-rays or electrons, is due to the indirect action. Indirect action can be modified by chemical reagents. Irradiation of a cell can result in various consequences such as no effect in the system; disrupt apoptosis, DNA mutation, and even higher resistance to the subsequent irradiation.

Radiation damage to the mammalian cells may be lethal, sub-lethal, and potentially lethal damage. An organ or tissue expresses response to radiation damage either as an acute effect such as inflammation, denudation of tissues, and hemorrhage, or as a late (chronic) effect such as organ dysfunction, blood change, sperm damage, stenosis, and obstruction of the intestine. Late

effects may be generic and caused by absorption of radiation directly in the tissues, or consequential to acute damage in overlying tissues. Chronic effects belong to the deterministic type where severity increases with the increasing dose above its threshold radiation dose.

The effects of radiation on the human population can be classified as either somatic or genetic. Somatic effects are the effects due to the exposure of radiation to the individuals who suffer during their lifetime, such as radiation induced cancers (eg. carcinogenesis in skin, bone, lung, and thyroid), sterility, and opacification of the eye lens. Hereditary effects are the radiation induced mutations to an individual's genes leading to the birth of defective descendants.

The response of different tissues or organs to radiation varies markedly, depending primarily on two factors: the inherent sensitivity of the individual cells and the kinetics of the population. The cell survival curves for late responding tissues are more curved than those for early responding tissues as shown schematically in Fig. 3.6. For early effects the ratio α/β is large and α dominates at low doses. For late effects α/β is small and β has an influence at doses lower than for early responding tissues. Similarly α and β components of mammalian cell killing are equal at approximately $\alpha/\beta = 10$ Gy and $\alpha/\beta = 3$ Gy for early and late effects, respectively.

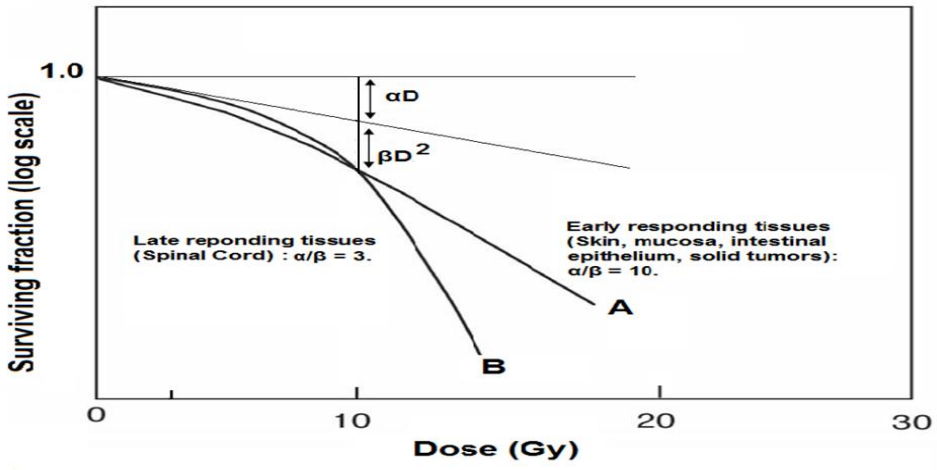

Fig. 3.6 Cell survival curves for the early responding tissues (A) and late responding tissues (B).

For the same radiation dose, radiation delivered at a lower dose rate may produce less cell killing than radiation delivered at a higher dose rate, because sub-lethal damage repair occurs during the protracted exposure. The typical dose rates used in radiotherapy are of the order of (1) 1 Gy/min in standard radiotherapy and high dose rate (HDR) brachytherapy, (2) 0.1 Gy/min in total body irradiation (TBI), and (3) 0.01 Gy/min in low dose rate (LDR) brachytherapy.

Fractionation of radiation treatment delivered over a period of weeks rather than in a single session would result in a better therapeutic ratio. However, to achieve the desired level of biological damage the total dose in a fractionated treatment must be much larger than that in a single treatment. The basis of fractionation is rooted in five primary biological factors in radiotherapy: radiosensitivity, repair, repopulation, reassortment, and reoxygenation.

Conventional fractionation splits the total dose into multiple fractions that spare normal tissues through repair of sub-lethal damage between dose fractions and repopulation of cells. Concurrently, fractionation increases tumor damage through reoxygenation and redistribution of tumor cells. The current standard fractionation is based on five daily treatments per week over several weeks of treatments. Other fractionation schemes are being studied with the aim of improving the therapeutic ratio such as hyperfractionation, accelerated fractionation, and continuous hyper-fractionated accelerated radiation therapy for 12 days. Our study employed hyperfractionation scheme that uses more than one fraction per day with a smaller dose per fraction (< 1.8 Gy) to reduce the long term complications and to boost the dose in tumor targets.

3.5 Dose computation algorithm and fluence optimization

The accuracy of computer treatment planning system is important in achieving clinically acceptable dose distributions using appropriate dose-computation algorithms in radiotherapy

treatments. The more practical dose computation algorithms are cone-collapse superposition algorithm (CCSA) for photons, and pencil beam algorithm (PBA) for electrons respectively.

3.5.1 Cone-collapse superposition algorithm

Terma is the total energy absorbed per unit mass of the voxel elements in the target medium. The CCSA algorithm calculates the terma volume of the tissues by employing the ray tracer techniques for the attenuated beams or the energy fluence through the CT image, the mass attenuation coefficients, and radiological depths in the ROI. The algorithm takes into account of the patient heterogeneity in the complete dose computation process in the commercial treatment planning system. Terma dose absorbed by each voxel of attenuation coefficient, μ (E,z), at the given depth, z, of the medium of density, ρ, which is exposed to the radiation of energy, E, is given as,

$$\mathrm{T(E,z)} = \frac{\mu\ \mathrm{(E,z)}}{\rho} * \mathrm{E} *\ \Psi\,\mathrm{(E,z)}; \tag{8}$$

for Ψ(E,z), the total fluence of energy, E, projected in unit area of cross section of the target element at depth, z, as shown in Fig. 3.7. It can be expressed as,

$$\Psi\,\mathrm{(E,z)} = \Psi\,\mathrm{(E,0)}\exp\left(-\mu(E,z) * \mathrm{z}_{eq}\right); \tag{9}$$

and $z_{eq} = \frac{\int_0^{\mathrm{z}} \rho\,(\mathrm{z}')\mathrm{dz}'}{\rho_{\,\mathrm{water}}}$;

The energy deposited, D(r), per unit mass of the voxel elements is quantized in a number of discrete cones defined in a given field in CCSA model. If the terma, T(r'), for all voxels in each discrete cones of volume, V, with the kernel density, K(r-r'), is known, then the total dose D(r),

deposited in unit mass of the target material at the depth, r, can be simply computed by the convolution of the terma with the kernel density in the given volume of cone,

$$D(r) = \int_{cone} T(r')K(r - r')d^3r' \; ; \qquad (10)$$

The CCSA is now available for clinical use on various commercial treatment planning systems (TPSs). This more complex dose model was first described in 1987. In contrast to the one-dimensional correction of the PBA, the CCSA uses full three-dimensional density scaling to model the effects of nearby heterogeneities on dose-calculation points. This results in increased accuracy, particularly with in regions of low-density tissue and steep density gradients (such as interfaces between lung and soft tissues) than PBA models.

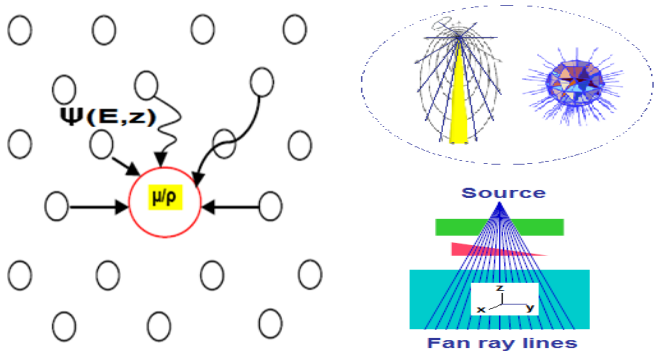

Fig. 3.7 Lay out for the cone-collapse superposition algorithm for the x-ray photons. Cone collapse removes the inverse square law and utilizes the exponential attenuation of the fluence.

A number of previous studies have verified the accuracy of the ADAC Pinnacle (ADAC Laboratories, Milpitas, U.S.A.) based CCSA model in the homogeneous and heterogeneous phantoms. Francescon et al. [27] used patient CT data to compare the Pinnacle CCSA model with a Monte Carlo-based dose model, a gold standard for the dose calculations. It was shown that, for breast and mediastinum treatments, the results of the two calculation methods are

comparable, with no systematic differences. The accuracy of the dose calculations using the CCSA instead of the PBA model is limited by 2% variation with the Monte Carlo-based dose model in various treatment sites. Similarly, various measurements have also shown that neither algorithm correctly models the dose at interfaces between bone and soft tissue, but it was indicated that the CCSA was more accurate within the bone.

3.5.2 Pencil beam algorithm

The pencil beam is represented in terms of the standard single polyenergetic kernel developed from the measured beam data and the Monte Carlo-based kernels. It is necessary to provide the input information in the dosimetric application, however, one can only measure dose in a plane perpendicular to a beam, not the whole spectrum, at individual pixels covering the radiation field. Therefore PBA takes into account of the intensity distribution at each pixel in each plane in reference to a particular dose grid as shown in Fig. 3.8.

The dose is computed to the reference point, P, in each plane taking into account of the contributions from the total dose grids in the circular disk of radius, r, at the radiological depth, d_e using the expression (11). As shown in Fig. 3.8, (x,y) is the coordinates of P at the treatment machine's iso-centric source-to-axis of rotation distance (SAD), and (x_r,y_r) is the coordinates of the differential area element at distance SAD. The integration of the dose calculated in each planes following the techniques, would generate the full spectrum of the pencil beam dose distribution in a given field size.

$$dose_P = I_0 \times dose\_c \times OCR_{med}(t,d_e) \times (SAD/SpD)^2; \quad (11)$$

$$\text{for } I_0 = \frac{1}{2\pi}\int_0^{2\pi}\int_0^{R} K(r, d_e\ (r,\ \theta\ )) \times Field(x_r, y_r) \times \frac{drd\,\theta}{Max\left[1.0, OCR_{air}\left(\frac{r}{SSD_K + d_e\ (r,\theta\ )}\right)\right]} \text{ and } t = \left[\frac{\sqrt{(x^2+y^2)}}{SAD}\right];$$

where dose_c = dose rate constant that normalizes the computed dose for some field size, SSD, and depth with the calibrated dose for the same field size, SSD, and depth,

Off Axis Correction, $OCR_{med}(t,d_e)$ = Off axis correction for the fluence delivered at the tangent of the angle (t) with the central ray (z) at the effective radiological depth (d_e (r,θ))in the medium for the largest field size,

SAD = 100 cm, and SpD = Distance from source to the plane of point, P, along central ray (z), $(SAD/SpD)^2$ = Inverse square law, and Field = Field size ratio at (x_r,y_r),

Kernel density, $K(r,d_e)$ = Pencil dose distribution in unit length of radius (r) from the incremental area (ds; dr rdθ) at the radiological depth ($d_e(r,\theta)$) in the medium for a given field size.

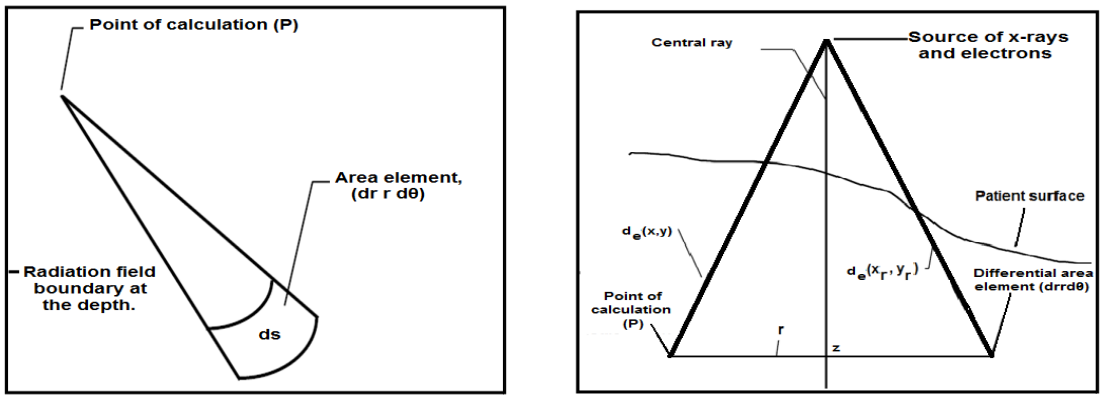

Fig. 3.8 Dose computation for electrons and x-rays in a medium using pencil beam algorithm. The diagram shows the integration of the pencil beam in the radiation field by calculating the contribution of dose from the cross-section of the differential element (ds) to the point (P) at depth (z) in the patient body.

Pencil kernel, $K(r,d_e)$, is primarily determined along the central ray (z) using the Gaussian spectrum obtained from the Monte Carlo computation of the poly-energetic point spread function in subsequent planes along z, and the primary data obtained from the central depth dose (E_0)

measurements in medium at various radiological depths (d_e) along z for the given field size. The Gaussian spread function for the pencil beam kernel can be expressed as,

$$I = I_0 \exp\left(\frac{-(E-E_0)^2}{\sigma}\right), \text{ where deviation } (\sigma) = \begin{cases} \sigma_l & where\ E \leq E_0 \\ \sigma_u & where\ E \geq E_0 \end{cases} \quad (12)$$

EBT technique employs PBA as suitable dose calculation algorithm. High energy electrons deposit relatively a larger amount of dose than the high energy photons in the superficial treatment of the homogeneous targets. Although PBA meets the tolerance of targets and neighboring organs for the treatment plans in regions of homogenous tissue density, various studies have shown the limitations of the PBA where heterogeneities exist such as lungs tissues. Dose calculated from the PBA models in lung-soft tissue interface regions are much higher than that computed from CCSA models. These limitations are due to the one-dimensional density correction of the PBA, which does not accurately model the distribution of secondary electrons in regions of tissue heterogeneity [28].

PBA doses are scaled according to the radiological depth along a ray-line from the radiation source to a calculation point, not accounting for the effects of side and backscattered radiation. It has also been observed that the number of monitor units (MUs) is generally lower for the PBA, meaning that the absolute dose delivered to the isocenter is lower than the PD. This warrants the modification of the PDs in order to account for the more accurate absolute dose calculation at the target. If not corrected for, delivered dose would increase with the introduction of routine use of the CCSA model, which may have implications on doses to OARs. This shows the advantage of the CCSA model over PBA model, as the former accounts for the increased effect of lack of scattered dose to the isocenter with increasing field size.

The implementation of the CCSA algorithm represents a milestone in the development of dose modeling in radiation therapy. It is likely to be superseded by advanced Monte-Carlo based models within few years, which will give more accurate modeling in the vicinity of the bones.

3.5.3 Fluence optimization algorithm

As discussed earlier, 3DCRT, IMRT and EBT are the major clinical procedures to treat the malignancies using the fundamental properties of high energy radiation and particle beams. In modern science, various computer programs are used to design the optimal radiotherapy treatment plans such as IMRT and 3DCRT. Although the overall processes of IMRT and 3DCRT are quite similar, these techniques employ opposite approaches for planning purpose. Conventional 3DCRT treatment planning is forward based and manually optimized in order to achieve the desirable dose distribution in target. An optimal 3DCRT plan is the result of an iterative manipulation of beam energy, weighting, and direction, and beam modifying devices such as blocks, wedges and MLC field shaping. Although computer-driven optimization of parameters such as beam direction [29], and weighting [30] has been attempted, it has met only limited clinical success.

Conversely, with IMRT dose distributions are inversely determined, meaning that the treatment planner must specify in advance the dose distribution that is desired, and the computer then calculates a set of beam intensities that will produce, as nearly as possible, the desired dose distribution. Specification by the planner of the desired dose distribution is made by means of dose-volume constraints in which the planner defines for the minimum and maximum desirable doses for all structures in the plan such as CTV, PTV, and radiosensitive normal tissues, and a set of penalty weights to indicate the relative importance of meeting the specified dose constraints for each structure. So, for IMRT the optimization parameters and structures are the

primary variables used to control the dose distribution as opposed to the beam weights or shapes as in the 3DCRT plans. Therefore the combination of beam placements, optimization parameters, dose computation algorithm, and volume delineation of the structures needed to achieve the optimal plan is always patient specific.

For each IMRT treatment field, the collimator is generally adjusted to enclose the targets with a certain margin (1.5-2 cm) that prevents the target from lying within the beam penumbra and avoids the undesirable intensity peaks near the beam edges. An initial dose calculation is performed during which each beam is divided into finite size beam segments (eg. 4 mm x 4 mm) and the dose deposition coefficients, a_{ij} representing the dose deposited to i^{th} point in a structure for a unit weight of the j^{th} ray, are calculated using the ray tracing techniques. The dose deposition coefficients contain all the information needed by the optimization algorithm, to determine the intensity profiles for the specific IMRT field. The desired dose distribution is described through the optimization parameters (i.e., constraints) for the targets and normal tissue organs. Thus the optimization is achieved by using an iterative process to minimize a quadratic objective function (F_{obj}), as shown below in a simplified form for a single target:

$$F_{Obj} = \frac{1}{N}\left[\sum_j (D_j - C_p)^2 + \sum_k w_k \sum_j \Theta(D_j - C_k) * (D_j - C_k)^2\right]; \quad (13)$$

where C_p is the prescription dose for the target and C_k is the dose of the k^{th} target constraint,

w_k is the user-defined penalty for the k^{th} target constraint,

D_j is the actual dose to the j^{th} point within the target and N is the number of target points.

For targets, a prescription dose and a dose window defining the maximum and minimum dose constraints are allowed. For critical structures, dose and dose-volume constraints are taken

into account in the optimization of the IMRT plan. Dose constraints are defined by a maximum dose and penalty, while dose-volume constraints are defined by a dose-volume combination and penalty. All optimization constraints, so-called soft constraints, allow violation of the constraint at certain cost (i.e., penalty). Hard constraints may not be violated under any circumstances.

Upon completion of the optimal plan, MU settings are calculated and plan documentation is prepared to coordinate effectively with the beam delivery systems. Independent verification of the MU setting for each field is also performed using water phantoms. A stand-alone software application is generally utilized for the quality assurance of IMRT plans. This software accepts as input, the leaf motion file and MU setting for each field derived from the simulation. From the leaf motion file, an intensity profile is generated and the dose to a user-specified point is calculated in the phantom using MU settings. The dose profile in the portal image is compared with the DRRs imported from the planning system for a specific treatment to validate the plan.

Because of the increased conformality of the dose distributions achieved with IMRT, accurate and precise patient treatment is of even more importance than with conventional treatment. All patients undergoing IMRT are generally immobilized according to the tumor location and patient condition using the custom foam or thermoplastic molds for prostate, head and neck, and breast patients. After immobilization set up in CT simulator room, all patients undergo simulation, during which images are acquired throughout the treatment volume or an isocenter is defined. Using the CT and other appropriate image sets such as MRI or PET, the PTV and critical organ contours are defined and transferred along with the images to the TPS.

IMRT templates defining the optimization parameters and clinical criteria for all targets and normal tissues are developed by physicists for each site prior to the large-scale IMRT implementation. These templates utilize the goals and realities of the IMRT treatments

performed on a significant number of the patients. After optimization, the intensity profiles are typically converted into 100-200 segments, requiring that in each segment, at least one leaf move at the maximum allowable speed, thereby minimizing treatment time. Both transmission through the leaves and the effect of the rounded leaf edge of the MLCs in the Clinac are considered for correction in real dose estimation in the target. Since the original intensity profiles cannot be converted with complete fidelity, the final leaf motion is converted back into a deliverable intensity profile for the subsequent forward dose calculation and the plan evaluation purpose.

3.6 Evaluation of radiation therapy treatment plans

The radiotherapy plan can be evaluated using various types of standard methods including planar dose distributions, DVHs, UPIs, and radiobiological indices such as TCP and NTCP.

3.6.1 Isodose curves and dose-volume histogram

Various energies are used in radiotherapy treatments using both photons and electrons. Changing the beam energy will affect the dose delivered at various depths. The deposition of dose within a medium can be visualized through the use of isodose curves in the treatment plan. Isodose curves are the first hand metric to examine how the dose is deposited within the medium, and are expressed in terms of the percentage of the dose delivered with respect to the reference.

As shown in Fig. 3.9, skin sparing occurs by high dose regions being concentrated in the target volume and low doses occurring more superficially in the tissues. A single photon field incident upon a flat area of tissue will have isodose curves that are uniform and deposit a maximum dose to a known depth, beyond which the dose decreases. The conformal isodose lines to the target allow dose to be accurately shaped to its volume in the optimal treatment plan.

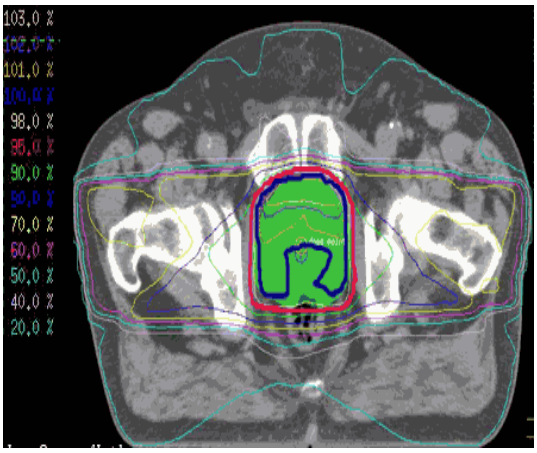

Fig. 3.9 A transverse view of a typical seven beam intensity modulated radiation therapy (IMRT) treatment of a prostate cancer patient. The target volume is shaded green, the 95% isodose line is red and the 100% isodose line is blue.

The second metric commonly used is a DVH curve, which plots the amount of radiation deposited against the volume of tissue that receives that dose as exemplified in the Fig. 3.10.

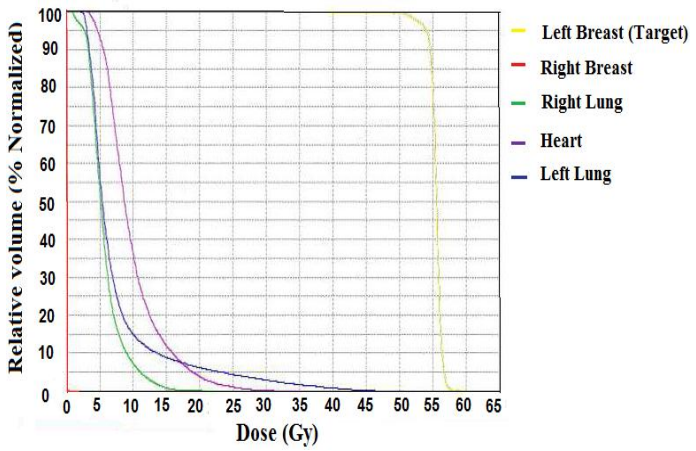

Fig. 3.10 Figure shows a cumulative dose-volume histogram (cDVH) analysis in a typical 3D conformal radiation therapy (3DCRT) treatment of the whole breast in a left-breast cancer patient. The yellow line that represents the target volume has nearly100% of its volume receiving 50 Gy of radiation, and the critical organs in the region on average receive between 5 and 10 Gy.

Although cDVH analysis easily determines the problems in a treatment plan by visual inspection, the sDVH analysis would be needed in order to locate the “hot spots" precisely in the critical organs that receive more radiation than the tumor target, PD, in the contiguous region. The details on sDVH analyses (x-,y- and zDVHs respectively) are also available in Appendix B.

3.6.2 Indices of radiation therapy treatment plans

Plan indices are important to assess the accuracy of the radiotherapy treatments. It takes into account of the dose homogeneity, conformality, and the sparing of normal tissues in the plans. The search for a single parameter to determine the quality of these plans is still ongoing, but, as of yet unsuccessful. In this perspective, a more practical approach of analyzing radiotherapy plans is to utilize the UPI set and the overall quality factor (QF) of the treatment as discussed in literature [31]. The details on UPI parameters are also available in Appendix C. The QF parameter helps to identify the under-dose and over-dose treatments.

3.6.3 Radiobiological models

The outcomes of radiotherapy treatments can be precisely evaluated using the biological models such as TCP and NTCP. TCP can be evaluated by using the Poisson statistics model, and NTCP can be evaluated by using the sigmoidal dose response (SDR) model for homogeneous medium based on equivalent uniform dose (EUD) techniques proposed by JT Lyman [32].

The necessary and sufficient conditions for a TCP model require the killing of all tumor clonogens. Assuming the heterogeneous irradiation in the tissues, the overall TCP is defined as the product of the probability of killing all clonogens in each differential volume element (v_i) of a tumor target irradiated with a dose (D_i) in the Poisson statistics model [31]. Furthermore, the overall TCP takes into account of the cell survival fractions assuming the single hit mechanism of the cell damage. It can be expressed as:

$$TCP = \left[\frac{1}{2}\right]^{\sum_i v_i \exp\left[\frac{2\gamma 50\,(1-D_i/TCD_{50,5})}{\ln 2}\right]}, \tag{14}$$

where the parameters $TCD_{50,5}$ and $\gamma 50$ are the dose and normalized slope at 50% probability of tumor control in the target.

The probit function, $\Phi\left[\frac{EUD - TD_{50,5}}{m\,TD_{50,5}}\right]$, best describes the SDR model to determine the NTCP indices for the organs irradiated in radiotherapy treatments [33]. NTCP index can be best expressed as given below:

$$NTCP = \Phi\left[\frac{EUD - TD_{50,5}}{m\,TD_{50,5}}\right], \tag{15}$$

The generalized mean dose (GMD) or EUD represents the dose that, if delivered uniformly to the normal tissues or to the entire critical structure, would produce the same effect as the heterogeneous dose distribution in a total volume (V_{max}) of a structure in JT Lyman model. The parameter, m, controls the slope of the dose response curve, and $TD_{50,5}$ determines the position of a dose response curve at 50% chance of complication in the critical structure. Furthermore, the GMD can be expressed as:

$$GMD = \left(\sum_i v_i D_i^{1/n}\right)^n, \tag{16}$$

where n determines the dose-volume dependence of a tissue which is deterministic for differences in tissue architecture. The expression (14) is commonly used to predict the dose response probability and the TCP of the tumor target, and expression (15) is used to estimate the NTCPs of the critical organs in the neighborhood of the target respectively.

The above method, as proposed by Lyman for DVH reduction to a single dose (GMD) irradiated to the V_{max} of the homogeneous structure, is analogous to the Kutcher-Burman (KB) reduction scheme for a non-uniform DVH in the inhomogeneous medium, to a uniform one with an effective volume (V_{eff}) using expression (17), and a reference dose equal to the maximum dose (D_{max}) delivered to the organ [34].

$$\frac{V_{eff}}{V_{Total}} = \sum_{i=1}^{N}\left[\left(\frac{D_i}{D_{Max}}\right)^{\frac{1}{n}}\left(\frac{V_i}{V_{Total}}\right)\right], \quad \text{and} \quad TD_{50,5}\left(\frac{V_{eff}}{V_{Total}}\right) = TD_{50,5} * \left(\frac{V_{eff}}{V_{Total}}\right)^{-n}; \tag{17}$$

The KB and Lyman models are found to be more consistent with the expected biological effects. These are the most robust techniques out of many available DVH reduction schemes. Similarly the uncomplicated cure probability (P+), a probability of achieving tumor control without the appearance of normal tissue, can be evaluated as,

$$P+= TCP * \Pi_i\,(1 - NTCP(i)); \tag{18}$$

where the index, NTCP (i), refers to i^{th} critical structure in the neighborhood of the tumor target. The choice of the specific NTCP model can have a profound impact on the treatment planning decisions in the advanced radiation therapy treatments.

Chapter IV

Methods and Materials

4.1 General consideration

This study was primarily focused on the precise diagnosis of the tumors, the XRT treatment planning and its evaluations using the DVH analysis and the BMOA. The procedure was initiated by the proper identification of the tumors, and the precise delineation of the GTVs in the CT-images of the cancer patients using the CT-simulator system. Additionally, the PET/CT dual imaging modality was also utilized in the efficient detection of the tumors in the lung cancer patients. The radiation oncologist also performed the GTV and PTV delineations and the contouring of the organs in the CT or PET/CT images in the commercial TPS. The physicians also prescribed the radiation dose for the treatment of the specific type of cancer diseases.

The target specific radiation dose were first computed using the attenuation coefficients of the tissues, fats, and bones based on the CT numbers of the pixel images in the CT scans imported into the TPS. Furthermore, the treatment dose was also computed using CCSA and PBA models for the photons and electron beams respectively. The commercial TPS was also validated with the measured dose data using a commercial water phantom. The optimal treatment plans were designed in the treatment of four different types of cancers such as head and neck, prostate, breast, and lung cases using the 3DCRT and IMRT techniques. The accuracy and the outcomes of the 3DCRT and IMRT plans were further assessed using the DVH modeling, UPI indices, and the various types of radiobiological models in the proposed treatments.

4.2 Computed tomography simulator and clinical linear accelerator

Improvement in imaging technology makes difference in every stages of the radiotherapy treatment process. Whilst for many treatments, the definition of the 3D tumor volumes is a primary requirement; CT simulation is the basis for all types of radiotherapy treatments. Dedicated CT simulators are comprised of a CT scanner, computer controlled laser patient positioning/ marking system and offset corrections, and a workstation. These simulators allow the manipulation and visualization of the CT data in 3D planes for the target localization in virtual (or CT) simulation process [35]. The multi-planar image reconstructions (MPRs) are the derivatives of the axial CT slices reconstructed in other planes, such as coronal or sagittal slices. MPRs are used to define both the treatment volumes and to spare the OARs by simplifying the treatments. The simulation process includes the selection of field sizes, gantry angles, and other machine parameters to define the treatment beams to cover the targets. The fluoroscopy image and the X-ray film in conventional simulator are replaced by the DRRs in the virtual simulator.

The simplest method of virtual simulation is to model the methods used with the conventional simulator. With this approach, the first step is to position the treatment fields on the DRRs, and the axial scans and the MPRs are then used to assess the field coverage of the target. The main feature of these scanners is the increased aperture size (up to 85 cm) allowing the use of patient immobilization devices as shown in Fig.4.1. Large-bore CT-simulators are specifically designed with the therapeutic needs in mind. The increased source–to-detector distance on these larger scanners slightly increases both the noise levels of the scans and the patient dose, but these increases are minimal, and have little diagnostic or clinical impact. In this study, CT-Simulator (Brilliance, Big bore oncology, Philips) with the aperture bore of 85 cm, and a commercial TPS, Pinnacle^3 (Philips, v.7.6c), were used for the virtual simulation using the DRRs and MPRs.

Fig. 4.1 Computed tomography (CT) simulator, Brilliance Big Bore Oncology (Philips medical system), installed at NMH Robert Lurie cancer treatment center.

The simulator was capable of scanning a field of view of 60 cm width using rapid view 4D / 3D cone beam FBP image reconstruction of DRRs and MPRs. It was designed to produce 8-16 slices per revolution with 2.4 cm maximum field-coverage. The simulator employed X-ray source power of 120 kV at 85 mA current for the diagnostic applications. CT slices were generated at 3 mm spacing and 0.9 mm image resolution for all types of radiotherapy treatments.

The Elekta Clinac (SLA series) was utilized in the simulation procedures in the TPS using the high energy photons and electrons as shown in Fig. 4.2.

Fig. 4.2 Elekta clinical linear accelerator (SLA-series) installed at NMH Laurie cancer center.

Each of the 40 pairs of MLC leaves was capable of projecting the fluence over 1 cm width at 100 cm isocenter of the machine. The resolution of the MLC was 2.5 mm at the isocenter. The thickness of the lead built MLCs was 7.5 cm. The electron beam was initially accelerated at 25 keV energy through the electron gun composed of non-gridded diode in the Clinac. The beam was further accelerated using the magnetron based dual-energy travelling wave guide system.

In general, the electron beam performs an oblique shape rotation using the bending magnet of 202.5^{o} after traversing the wave guide system, and the rotated beams hit the scattering foils after exiting through the copper window in the Elekta machine. Tantalum and aluminum alloy are the primary and secondary scattering foils used for the generation of electrons, whereas the tungsten are the target material for the high energy X-ray photons. The X-ray filters are basically designed from the steel built materials to overcome the beam hardness in such machine.

It is necessary to measure the dose delivered to the tumor target prior to the real treatment in patients. It is a common practice to verify the dose at various depths of the target using universal phantom (eg. distilled water phantom). In this study, Pinnacle^3 took into account of the dose delivered by the Elekta Clinac in the DC motorized Scanditronix-Wellhofer RFA water tank system (GmbH, Germany) supported by the Common Control Unit (CCU) and the OMNI-PRO software, at 100 cm source-to-surface distance (SSD) as shown in Fig 4.3.

The water tank (46 Kg; 200 liters; acrylic materials) was capable of scanning the phantom volume size of 48 x 48 x 41 cm^3. The CCU was built with the two integrated independent electrometers for the ion chambers and the diode detectors. The spatial resolution of ± 0.1 mm was employed in the dose measurement procedures in the water phantom. The electrometer had the current resolution of 5 fA ($5x10^{-15}$A) at maximum scale of 40 nA. The leakage current was typically less than 1 fA and the time constant of the filter was 20 ms in the electrometer circuit as

per the specification. The bias voltage range was ± 50 V through ± 500 V in the CCU unit, and the power was supplied from the primary source of 100–240 V AC (± 10 %) at 50-60 Hz.

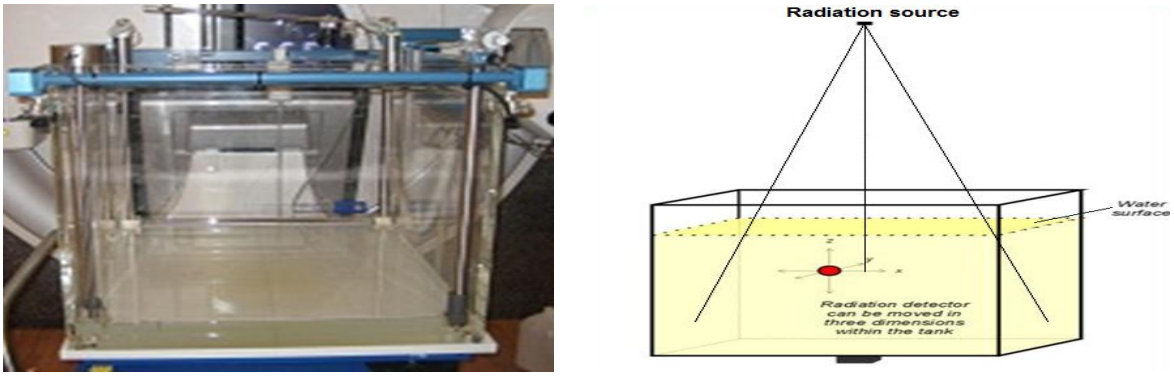

(a) (b)

Fig. 4.3 General overview of the water tank scanning system for the dose measurements: (a) IBA Scanditronix-Wellhofer Blue Phantom water tank system, and (b) the schematic diagram.

Photon / Electron field p+ silicon diode detectors (PFD^{3G}, Hi-pSi, SN: DEB012-3777; EFD^{3G}; Hi-pSi, SN: DEB002-3808) and IBA microchamber (Model CC01; effective volume of the tip of the vacuum tube: 0.01 cm^3) were primarily used for the dose measurement in the phantom as shown in Fig 4.4. Diameter of the active area of the diode was 2.0 ± 0.1 mm. The thickness of the Si-chip was 500 µm.

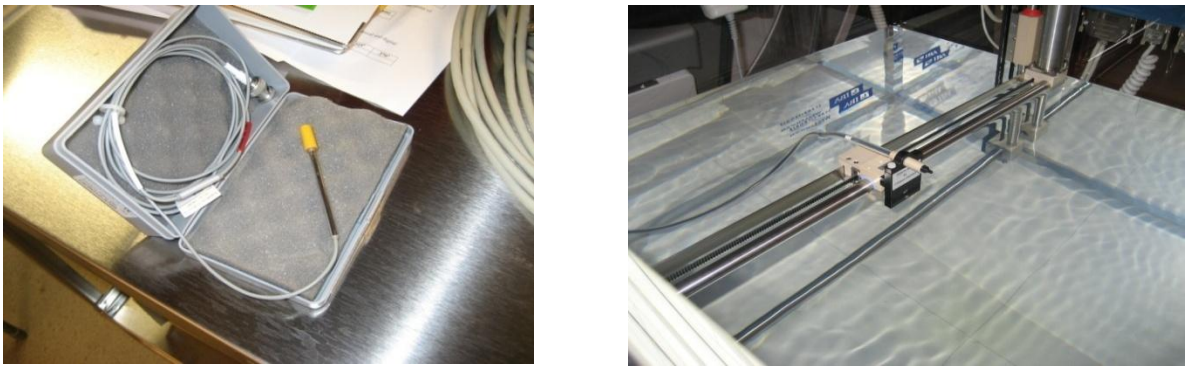

(a) (b)

Fig. 4.4 Radiation detectors (a) p^+ Si-diode detector (PFD^{3G}), and (b) IBA dosimeter.

4.3 Treatment planning system and patients profile

The radiation therapy treatment plans were simulated in the Pinnacle^3 designed and developed by ADAC Laboratories in the Linux environment. The Pinnacle^3 TPS efficiently coordinated the DICOM and RTOG data format of the CT scan, MRI scan, PET scan, and the ultrasound imaging with the radiotherapy treatment planning procedures using the high energy radiation and particle beams. The primary basis of the dose calculations were the CCSA for photons, and PBA for the electrons respectively. IMRT simulation utilized the DMPO algorithm to manipulate the intensity profile for the beam modulation. Field segmentations were also performed using the wedges, blocks, MLC shaping, BEV and DRRs in the plan simulation.

The radiotherapy treatments were primarily guided by the RTOG and ICRU protocols for the dose-homogeneity and conformality conditions in the tumor targets, and the dose-volume constraints in the critical organs. A retrospective study was performed to analyze the outcomes of the conformal XRT treatments of 38 head and neck cancer patients using a 9 field sequential IMRT boost (SqIB) treatment technique and 3 head and neck cancer patients using a 9-field simultaneous IMRT boost (SIB) techniques at NMH Laurie cancer treatment center. The SqIB and SIB techniques both utilized the coplanar beams followed by the hyper-fractionation dose delivery scheme on once a day (QD) week-on and week-off basis respectively. The dose was delivered at the conventional dose rate of 1.8-2.0 Gy/ fraction in the SqIB treatments, and at relatively high dose rate of 2.0-2.2 Gy/fraction in the SIB treatments respectively. Similarly other retrospective studies were also pursued in various cases such as (a) radiotherapy treatment of the 10 prostate cancer patients using conventional 4-field (4-FD) box techniques and 7-field IMRT treatments at the fractionated dose rate of 1.8 Gy/fraction in the QD week-on and week-off basis, (b) accelerated whole breast irradiation of the 10 left-breast cancer patients in the sequence using

the coplanar 3DCRT plans at the hyper-fractionated dose rate of 1.5 Gy/fraction in the QD week-on and week-off basis, and EBT plans to boost the target dose at the fractionated dose rate of 2 Gy/fraction in the QD week-on and week-off basis respectively, (c) 9 left-lung cancer patients using the 3-5 field coplanar 3DCRT or the oblique beam collimation (OBC) techniques for the curative intent at the dose rate of 1.8-2.0 Gy/fraction in the QD week-on and week-off basis, and the 8 left-lung cancer patients using the anteroposterior / posteroanterior (APPA) field for the palliative intent at the dose rate of 1.5 Gy/fraction in the QD week-on and week-off basis.

4.4 Beam profiles in clinical linear accelerator

The real dose delivered by high energy electrons and photons at various depths of the Scanditronix-Wellhofer Blue Phantom water tank, were measured at the room temperature (~22.3^{o} C) and atmospheric pressure (~744.6 mm Hg) using the solid state detectors (or micro-ion chambers), as discussed earlier in the section 4.1. The in-line and cross-line beam profiles were also measured utilizing 100 cm SSD technique in the water tank. These primary dose profiles were used to compute the possible dose delivered at various depths in the water phantom for various photon beam energies of 4, 6, 10, and 18 MV, and for the electron beam energies of 6,10,12,18, and 20 MeV in Pinnacle[3] as shown in Fig 4.5 (a,b) and Fig 4.6 (a,b) respectively.

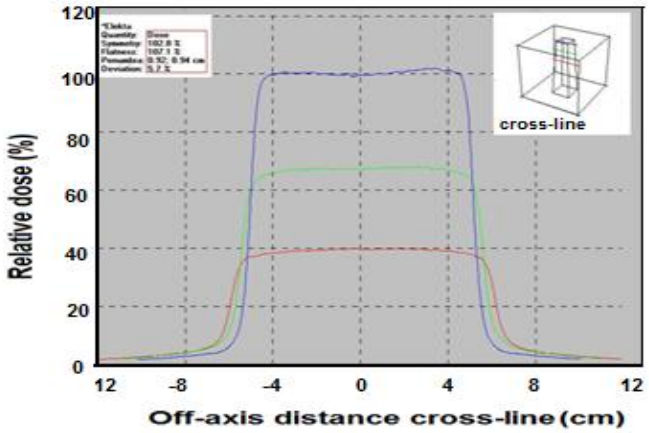

Fig. 4.5 (a) The figure shows the cross-line beam profile plot at maximum percentage dose depth (PDD), 10 cm and 20 cm depths respectively, in the Pinnacle[3] system for the 6 MV photon beam energy delivered to the blue phantom water tank system at 100 cm source-to-surface distance (SSD) using Elekta SLA series clinical linear accelerator (Clinac) at (10x10) field size.

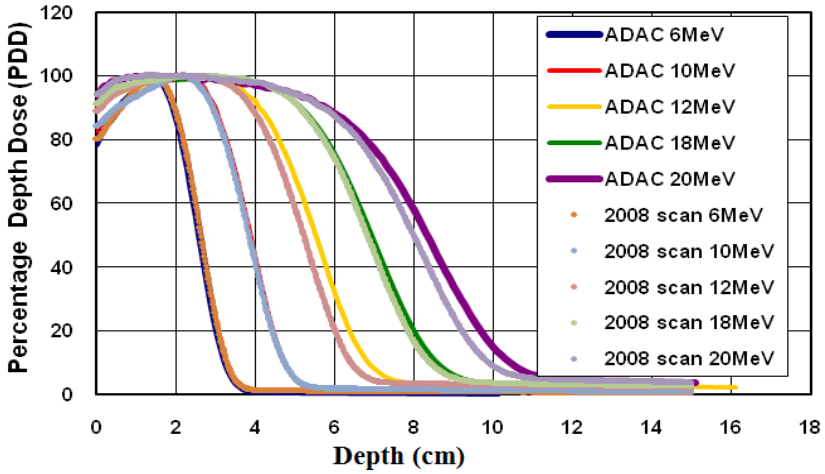

Fig. 4.5 (b) Comparison plots of the computed and measured percentage depth dose (PDD) profiles for 4,6,10, and 18 MV photon beam energy, in Pinnacle[3] using Elekta SLA series Clinac at (10x10) field size and the blue phantom water tank scanning system at 100 cm source-to-surface distance (SSD).

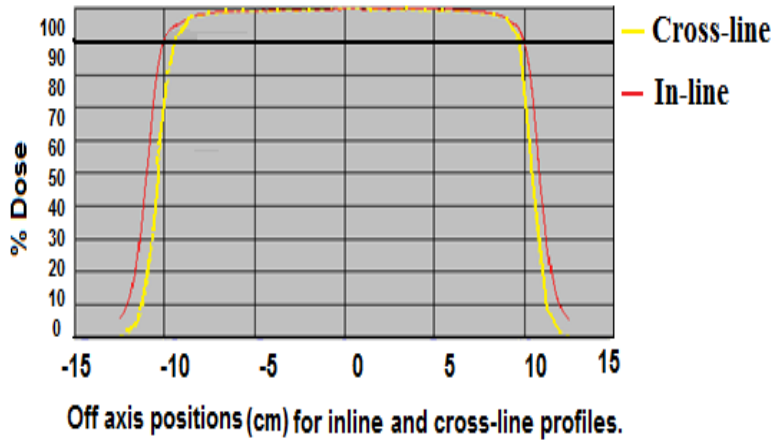

Fig. 4.6 (a) The figure shows the cross-line beam profile plot in ADAC Pinnacle[3] at maximum dose depth of 3.4 cm of 18 MeV electron beam energy delivered to the blue phantom water tank scanning system at 100 cm source to surface distance (SSD) using the Elekta SLA series Clinac at (20 x 20) field size.

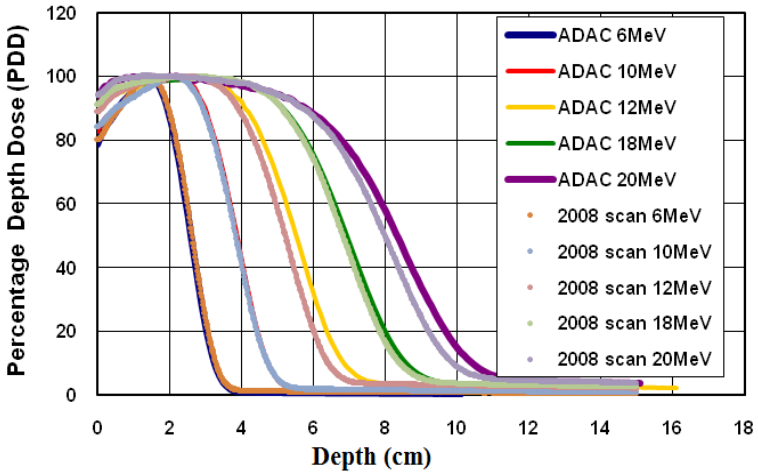

Fig. 4.6 (b) Comparison plots of the computed and measured percentage depth dose (PDD) profiles for 4,6,10, and 18 MeV electron beam energy, in ADAC Pinnacle[3] using the Elekta SLA Clinac at (10 x 10) field size and the blue phantom water tank scanning system at 100 cm SSD.

4.5 Target volume delineation and dose prescription

The physicians primarily determined the dimension and location of the tumors in the patient's body using high resolution DRRs in the CT scan, and biopsy wherever necessary. PET scans were specially used in delineating the MTVs in left-lung cancer patients. Threshold SUV of 40% and standard SUV value of 2.5 were the primary criteria for the precise detection of MTVs using non-deformational PET/CT image fusion. The CT images were primarily utilized to delineate the GTV in head and neck, prostate and left-breast cancer patients respectively.

Since DNA, itself, is very unstable in nature, it maintains the capability of repairing the damage caused to the genome by the external factors. Thus it is very important to deliver the sufficient radiation dose in order to destroy the microscopic and clonogenic cells in the tumor target completely. The cell survivality in the given ROI can be analyzed using the appropriate cell killing models in the radiation therapy treatment. In general, the treatable human tumors were found to be in the order of size 10 grams to 1000 grams in the study. A unit gm of tumor target comprises nearly 10^9 cells. A percentage of 10^9 cells in each gram of tumor are the clonogenic (malignant) cells. The maximum number of contaminated cells are estimated to be of the order of 10^{10}~10^{12} in 10-1000 grams of the target volume.

Assuming a typical size (N_o) of the order of 10^{12} of the clonogenic and contaminated cells in 1000 grams of PTV, the net survival fraction of the clonogenic cells can be easily estimated using the linear quadratic cell killing model. For instance, the model was tested at the typical PD of 75 Gy in nearly 42 and 37 fractions at the rate of 1.8 and 2.0 Gy per fraction of dose (D) in SqIB and SIB treatments of the head and neck cancer patients respectively. Cell killing is exponential with the cumulative dose exposure in tumor target in the linear quadratic model as shown in Fig. 4.7 for the high LET and low LET radiation. However, the cell death remains

constant for each fraction of the dose rate of 1.5-2.0 Gy, when delivered to maintain an average of one event in each cell of the target. Typically 3 ion pairs are generated for each photon of energy 100 eV, when radiation is delivered to the homogeneous target. The net survival fraction (S) of the clonogenic cells in this model can be estimated as,

$$\frac{S}{N_O} \sim \exp^{-f(\alpha D+\beta D^2)} \; ; \tag{19}$$

for α =0.3 Gy^{-1}, β =0.03 Gy^{-1} for the total number of fractions (f) and the fractional dose (D).

Therefore, S_{SqIB} is estimated to be 3.9, and S_{SIB} is estimated to be 2.7 in 1000 gm of PTV at PD of 75 Gy. The SIB technique delivers higher dose to the target with priority to destroy a large number of microscopic and clonogenic tumor cells, however it always poses a higher risk of developing complications in the normal tissue organs in the neighborhood of the targets than the SqIB treatments [36]. The PDs were also estimated using similar formalism for other types of case studies such as prostate cancer, breast cancer, and lung cancer respectively.

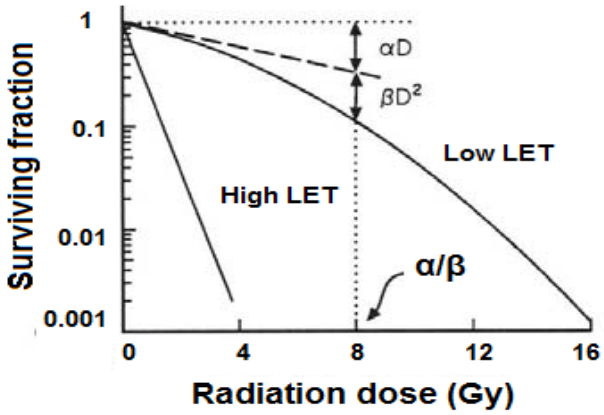

Fig. 4.7 Typical cell survival curves for high linear energy transfer (LET) radiation and low LET radiation for the current linear quadratic model based on the multi-target single hit cell killing mechanism [5].

4.6 Planning and simulation in the radiation therapy treatments

As discussed earlier, various types of plans were designed in the XRT treatments of the head and neck cancer patients, the prostate cancer patients, the left-breast cancer patients, and the left-lung cancer patients respectively. The methods are systematically presented as given below.

4.6.1 Radiation therapy treatment of head and neck cancer patients

The radiotherapy treatment planning of the head and neck cancer patients requires special attention due to the complex geometry of the targets and its neighboring critical organs. In the study, the inverse treatment planning techniques were chosen as the optimal methods of the treatment planning of 38 and 3 head and neck cancer patients at stages 2-4, using SqIB and SIB techniques in Pinnacle^3 TPS system. The SqIB and SIB techniques were implemented to deliver the cumulative PD of 72.52 ± 0.73 Gy (N=38) and 72 Gy (N=3) to the targets at the iso-center of SAD (100 cm) respectively.

SqIB employed the therapeutic technique with 6 MV X-ray photons to deliver the dose in the targetand the dose level was boosted systematically to the PTVs (PTV1, PTV2, and PTV3 respectively) in the order of three sequential plans (PTV1, PTV2, and PTV3 plans respectively) administered in 7-8 weeks of the treatments scheduled on week-on and week-off basis. However SIB also employed the therapeutic technique with 6 MV X-ray photons, which implemented the simultaneous dose delivery techniques to all PTVs (PTV1and PTV2) at the same time in two concomitant plans (PTV1 and PTV2 plans) administered in 4-5 weeks of the treatments. Similarly an additional boost was also delivered to the PTV3 target using PTV3 plan in the SIB based treatments.

The delineation of the PTVs and contouring of the neighboring organ volumes were consistently defined by the physicians in the retrospective study as presented below in Table 4.1.

Table 4.1 A standard outline of the structures contoured in the intensity modulated radiation therapy (IMRT) plans designed in the treatment of the head and neck cancer patients.

SN	General structures	Contour volumes
1	Brain stem	From top of pituitary fossa to foramen magnum.
2	Brain	Entire brain excluding brainstem; and partial brain (contour brain up to superior end of brainstem)
3	Pituitary gland	From top of pituitary fossa to bottom of pituitary fossa.
4	Spinal cord	Outlined up to tracheal bifurcation.
5	Cochlea (Right and left)	Contoured complete volume.
6	Optic nerves (Right and left)	Contoured complete regions
7	Optic chiasm	Rests on the diaphragm sellae that follows optic nerves
8	Eyes (Right and left)	Globes only
9	Parotid (Right and left)	
10	Sub-mandibular glands (Right and left)	
11	Oral cavity	From top of hard palate to mentum of mandible excluding maxillary or mandible, only mucosa)
12	Oropharynx	From lower border of soft palate to the tip of epiglottis, including tonsil, and BOT.
13	BOT	Base of tongue.
14	Supraglottic larynx	Includes thyroid cartilage, and to the tip of epiglottis.
15	Glottic larynx	Includes thyroid cartilage and sub-glottic larynx
16	Larynx	Supraglottic + glottic larynx; (Omit tracheal bifurcation).
17	Hyoid bone	Perimeter of the bone.
18	Post-cricoid esophagus	Esophagus behind the cricoid cartilage.
19	Cervico-thoracic (Ct) esophagus	Up to tracheal bifurcation (Omit post-cricoid esophagus)
20	Lips	
21	Mandible	Includes cornu.
22	Pharyngeal-constrictor (superior)	From inferior tip of pterygoid to upper tip of hyoid
23	Pharyngeal constrictor (middle)	From upper border of hyoid to lower tip of hyoid.
24	Pharyngeal constrictor (inferior)	From lower tip of hyoid to bottom of cricoids.
25	Combined constrictors	
26	Carotid vessels (Right and left)	From skull base to superior sternoclavicular joint.

Similarly the proper treatment environment is also presented systematically for the individual plans in both types of IMRT treatments in Table 4.2.

Table 4.2 Configuration and set up for the simulation of IMRT plans designed for the treatment of head and neck cancer patients in the commercial treatment planning system (Pinnacle[3]).

Target Volumes	PTV1 SqIB/SIB	PTV2 SqIB/ SIB	PTV3 SqIB/SIB	COMPOSITE SqIB/SIB
PD (Gy)	39-46 / 54	10-15/ 54	10-24/18	64-75/ 72
Dose rate (Gy/ fraction)	1.8-2.0 /2.0-2.2	1.8-2.0 /2.0-2.2	1.8-2.2/2.0-2.2	1.8-2.2/ 2.0-2.2
SAD (cm)	100	100	100	100/ 100
9-Beams (20-340@ 40^{o})	6 MV	6 MV	6 MV	6 MV/6 MV
3D-Target Contouring	PTV2 + (0.5– 1 cm)	PTV3 + (1 - 5 cm)	CTV + (0.5-1 cm)	*

Fig. 4.8 and Fig. 4.9 presents the schematics and the process of the IMRT simulations, and the delineations of the PTVs and the contouring of the neighboring organs using the SqIB techniques in Pinnacle[3] as discussed earlier in section 3.2.2.2. The Clinac delivered the dose obtained from the simulation using the step and shoot beam delivery systems at 100 cm SAD in BID basis at the dose rate of 1.8 Gy per fraction in the complete treatment cycle of 7-8 weeks using the SqIB techniques.

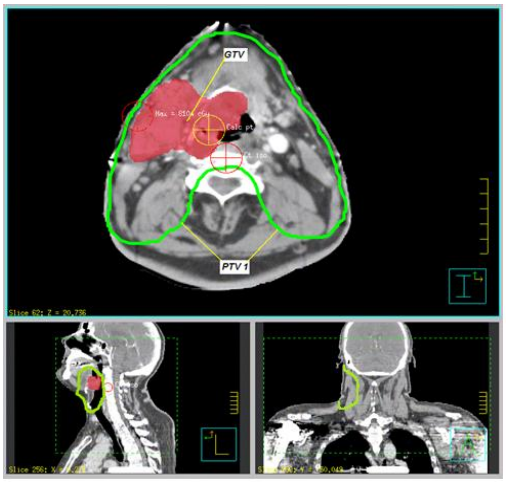

(a)

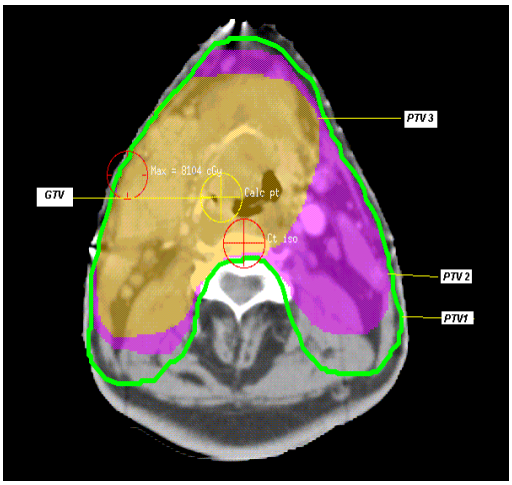

(b)

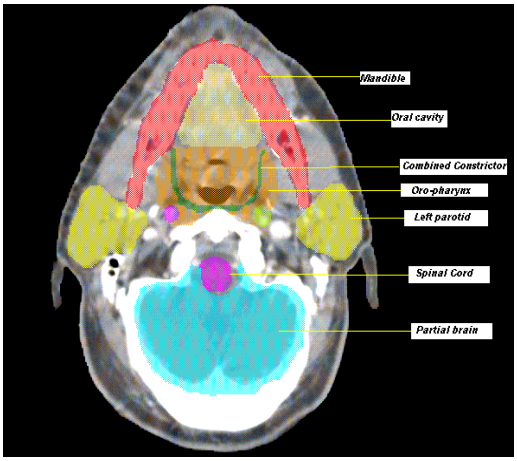

(c)

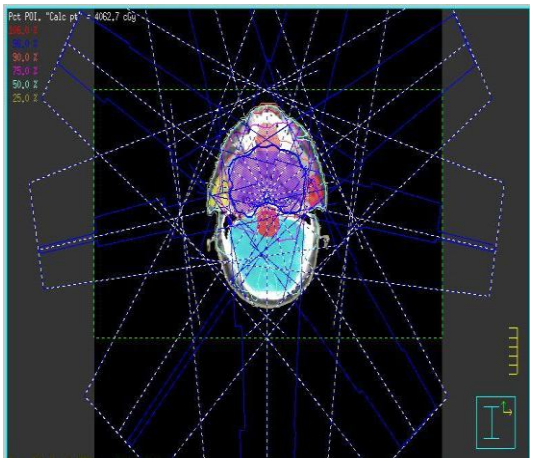

(d)

Fig. 4.8 (a) Gross Tumor Volume (GTV) delineation, (b) localizing the Planning Target Volumes (PTV1, PTV2, and PTV3), (c) contouring of the critical organs, and (d) nine beam alignment around the Planning Target Volumes (PTVs) using sequential IMRT boost (SqIB) techniques at 100 cm of source-to-axis distance (SAD), and step and shoot beam delivery system.

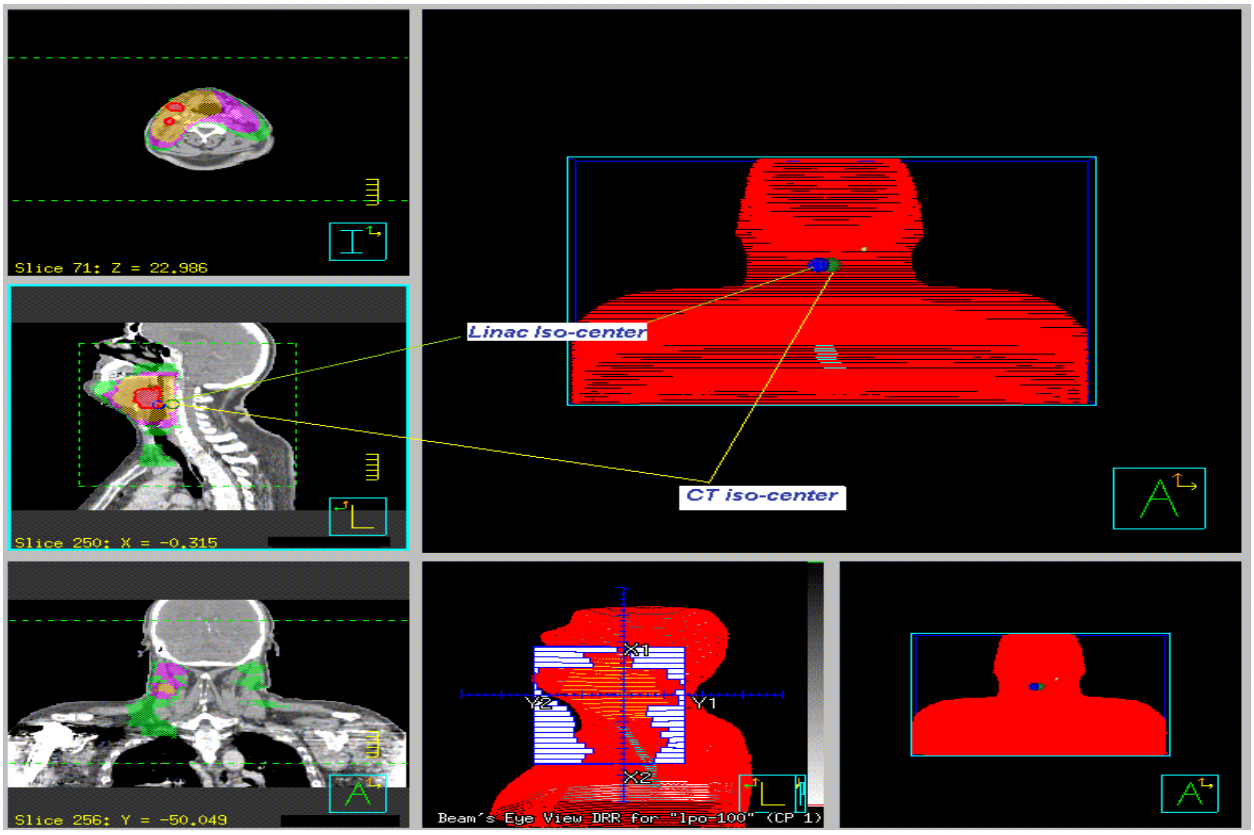

Fig. 4.9 Adjustment of the computed tomography (CT) iso-center and the Clinac iso-center, and the beam's eye view in the radiation therapy treatment planning using field segmentations with 40 pairs of multi-leaf collimators (MLCs) and non-uniform beam collimation technique.

4.6.2 Radiation therapy treatment of prostate cancer patients

Studies have shown that as many as 8 out of 10 men had prostate cancer by age 80. Prostate cancer begins with small changes (prostatic intraepithelial neoplasia; PIN) in size and shape of prostate gland cells, known as prostate adenocarcinoma. Cancerous prostate cells release a higher level of a chemical called PSA (prostate-specific antigen) into the bloodstream that can also be detected by the blood test. With the advent in technology, prostate cancer has been the most

widely used application of IMRT with the longest follow-up periods. Prostate cancer fits the ideal target criteria for the IMRT treatment because of the adjacent sensitive dose-limiting tissues (eg. rectal, bladder etc). A retrospective study was also performed on 10 prostate cancer patients at stages 2-4, and were treated with the radiation to the GTV in pelvis at PD of 45 Gy using a standard 4-FD box technique at SAD (100 cm), and 7 beam IMRT boosts to the PTVs at the isocenter of SAD (100 cm) to the cumulative PD of 69.6 ± 4.6 Gy (N=10) as shown in Fig. 4.10. Bladder was delineated using the iodinated contrast (dye) injected through a catheter inserted into the patient's urethra. Plans were simulated for the 4-FD box and the SqIB treatments with the fractionated dose rate of 1.8 Gy in the QD week-on and week-off basis.

The 4-FD box technique was utilized to treat the GTV in pelvis region based on forward planning method at 100 cm SAD using 4 beams with beam energy of 18 MV at PD of 45 Gy. Similarly 7 beam IMRT boost fields treated three PTVs (PTV1, PTV2, and PTV3 respectively) using the inverse planning method at 100 cm SAD, and step and shoot techniques with beam energy of 6-10 MV at PDs of (12.6 ± 2.5, 10.4 ± 0.76, and 5.1 ± 1.6 Gy respectively). Physicians and oncologists consistently performed the target volumes (GTV; PTV) delineations and the contouring of the neighboring organs in all plans prior to the treatments. However, the contours for the neighboring organs were found to be different in conventional 4-FD box and IMRT plans because the SqIB treatments were planned in the different CT scans in successive stages of the treatments after evaluating the progress of the earlier treatments.

(a) (b)

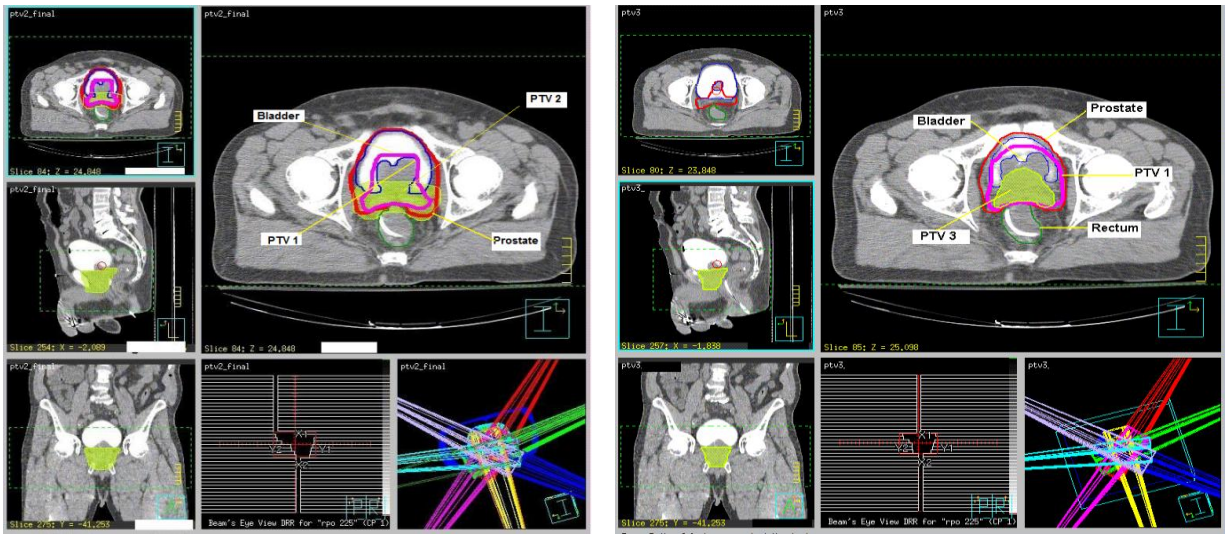

(c) (d)

Fig. 4.10 Radiation therapy treatment planning using (a) conventional four field (4-FD) box treatment of the pelvis region, (b) sequential IMRT boost (SqIB) treatment of PTV1 region, (c) SqIB treatment of PTV2 region, and (d) SqIB treatment of PTV3 region.

4.6.3 Radiation therapy treatment of left-breast cancer patients

A group of 8 left-breast cancer patients of stages 1-3 were treated by using the COMPOSITE plan designed for the accelerated whole breast irradiation technique. This technique was comprised of the 3DCRT treatments using the 6-18 MV X-ray photons at PD of 45 Gy, and the EBT treatments using 10-20 MeV electrons at PD of 6-16 Gy with the cumulative PD of 56.05 ± 5.23 Gy as shown in Fig. 4.11. Lateral and medial opposing photon beams were delivered to the inhomogeneous tumor targets in the whole breast based on the forward planning methods at 100 cm SAD in the 3DCRT treatments. Electron boosts were also delivered to the target at 100 cm SSD at normal incidence.

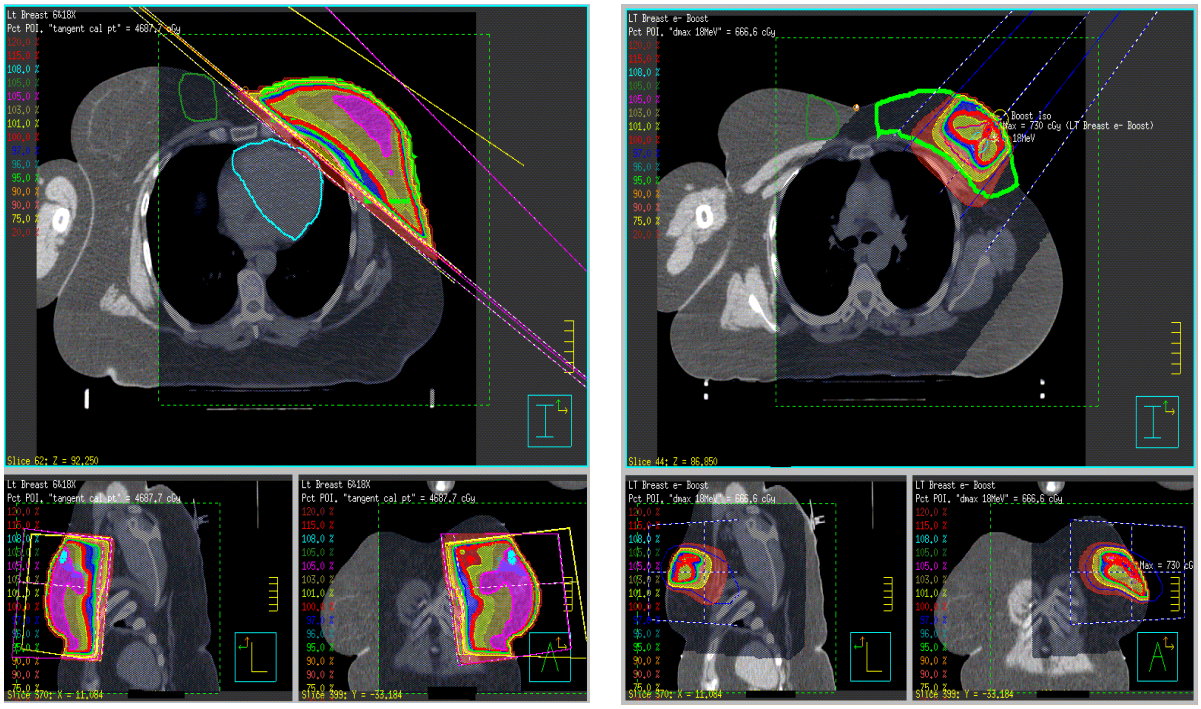

(a) (b)

Fig. 4.11 Radiation therapy treatment planning using (a) 3DCRT technique with the tangential photons delivered to the left-breast of the patient, and (b) the electron boost techniques with the normal projection of the electrons to the tumor bed at 100 cm source-to-surface distance (SSD).

4.6.4 Radiation therapy treatment of left-lung cancer patients

A group of 9 non-small cell left-lung cancer (NSCLC) patients at stages 1-3, were treated in QD basis with the curative intent using the forward plans in 3DCRT treatments. The treatment employed 3-5 fields with 10-18 MV X-ray photons to deliver the cumulative PD of 55.3 ± 3.1 Gy (N=9) at 100 cm SAD. Similarly 8 left-lung cancer patients in early stage were also treated with palliative intent using APPA, and OBC methods based on 3DCRT techniques. The APPA and OBC employed the simulation technique based on the forward planning method using the 10-18 MV X-ray photons at the cumulative PD of 31.0 ± 2.0 Gy (N=8) delivered at the 100 cm SAD as shown in Fig. 4.12. The COMPOSITE plan was designed in the PET/CT image fusion considering the inhomogeneity nature of the lung tissues. This imaging modality was very useful in the precise delineation of the MTVs in left-lung cancer patients.

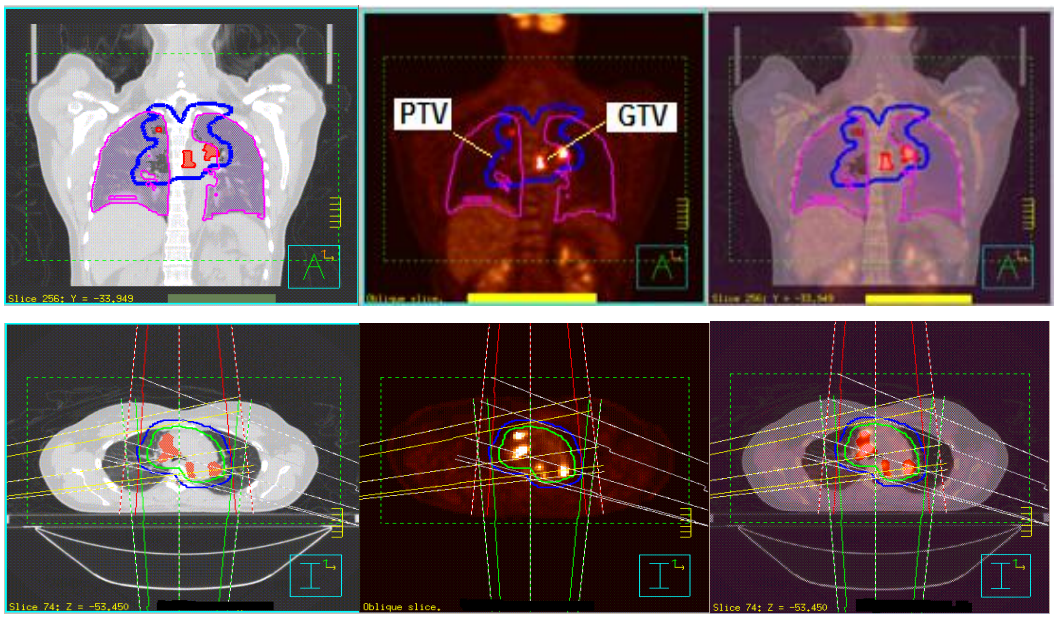

(a) (b) (c)

Fig. 4.12 Three dimensional conformal radiation therapy (3DCRT) treatment of the left-lung cancer patient using the (a) computed tomography (CT) scan, (b) positron emission tomography (PET) scan, and (c) manual PET/CT image fusion.

4.7 Computational environment in radiation therapy research

Several tools were also utilized for the computational purpose in the radiotherapy research. The most commonly available open source software system, Computational Environment in Radiotherapy Research (CERR; 2003) developed and maintained by the School of Medicine and Siteman Cancer Center, Washington University, St. Louis was also found useful in the 3D image analysis of the organs using the CT based images. The major applications of CERR are multi-modality image fusion, PET/SPECT/MR image imports, intensity volume histogram analysis, dose-volume and dose surface histogram analysis, translation and rotation of the structures in x,y, and z-axes, dose-distance plotting, transverse/sagittal/coronal slice viewing, dose metric comparison, IMRT planning, DICOM-RT and RTOG based image analysis respectively [37].

CERR was also utilized in our study for the image based DVH analysis in CT scan images obtained from the patients undergoing various types of radiotherapy treatments. It was also useful to analyze the biological modeling based outcome analysis of the treatments in the study. However, CERR does not provide the platform for the extraction of conventional and space based DVH statistics and the treatment plan evaluations using RTOG or DICOM-RT image formats. Thus a new tool, HART was also developed for the specific purpose of the study. The details on the development of the tool, calibration, and applications are presented in the literature [27]. HART offers spatial and conventional DVH analysis, UPI analysis to evaluate the treatment plans, physical parameterizations (eg. center of mass, attenuation coefficients), dose response modeling of the critical organs, biological modeling based outcome analysis of the radiotherapy treatments respectively. It is also an open source software system and is available online freely. It is also expected to be developed in future for the efficient application of space - time DVH analysis in various types of advanced radiation therapy treatment plans.

Chapter V

Results and discussion

5.1 Implication of PET/CT imaging in radiation therapy treatment of lung cancer

Lung cancer is the leading cause of cancer mortality among the men and women in the US and throughout the world. So an optimal approach of the treatment that can reduce the lung cancer mortality by even 20% has the potential to spare a significant number of people from the ravages of this disease and the radiation toxicity in the critical organs such as heart, lung, spinal cord and esophagus. Erratic heart beats, disability to pump the blood, and inflammation around the heart are the major cardiovascular risks due to the radiation toxicity in radiation therapy treatment of breast and lung cancer patients. Thus strong steps must be taken in order to minimize the dose level in heart to avoid further complications in the left-lung and left-breast cancer patients in the 3D conformal XRT treatments.

In this study, the PET/CT image fusions were utilized in the 3DCRT treatment of 8 left-lung cancer patients (N=8) to deliver the conformal dose to the GTVs delineated in lung sparing the critical organs such as thoracic esophagus, heart, spinal cord, and lungs. The average cumulative PD was 54.77 ± 3.33 Gy (N=8) in the 3DCRT treatment using 3-5 oblique beams with the curative intent of the disease. The volume coverage of the heart exposed to the radiation was successfully minimized to less than 5% at $TD_{50,5}$ in this technique as shown in Fig. 5.1.

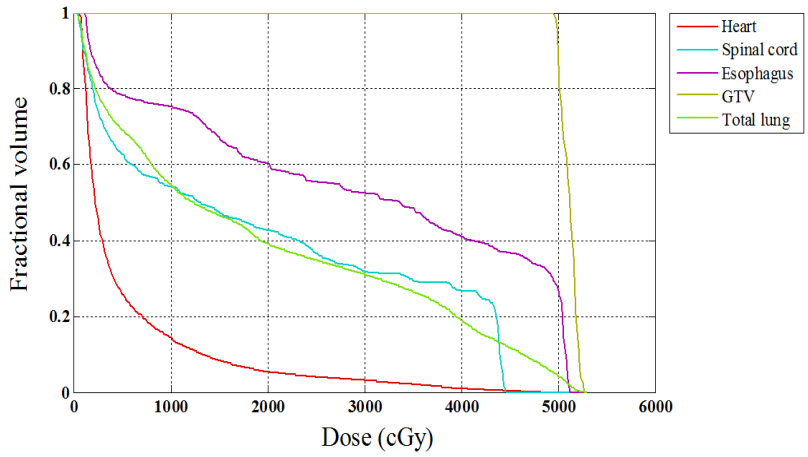

Fig. 5.1 (a) Relative dose-volume coverage in various critical organs and Gross Tumor Volume (GTV) in 3D conformal radiation therapy (3DCRT) treatment of a left-lung cancer patient.

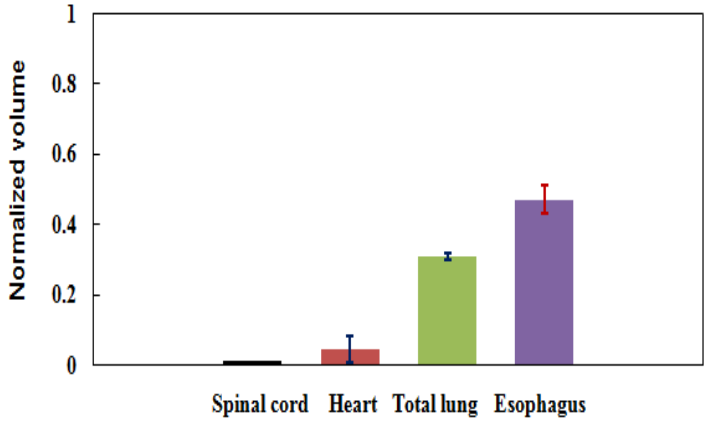

Fig. 5.1 (b) Dose-volume coverage at tolerance dose ($TD_{50,5}$) of the heart, spinal cord, total lung, and esophagus in the 3D conformal radiation therapy (3DCRT) plan designed in the treatment of the left-lung cancer patients at the cumulative PD (54.77 ± 3.33 Gy; N=8).

The contoured volumes were 24.9 ± 4.6 cc (N=8) at 95% confidence interval (CI) in the spinal cord, 520.9 ± 131.5 cc (N=8; CI: 0.95) in heart, 25.5 ± 4.3 cc (N=8; CI: 0.95) in thoracic esophagus, and 2957.4 ± 485.2 cc (N=8; CI: 0.95) in the total lung respectively. Relative volume coverage were 0 (N=8) in spinal cord, 0.05 ± 0.04 (N=8; CI: 0.95) in heart, 0.31 ± 0.03 (N=8; CI: 0.95) in total lung, and 0.47± 0.08 (N=8; CI: 0.95) in the esophagus at the corresponding

$TD_{50,5}$ of the organs respectively. The result showed that the esophagus ($TD_{50,5}$: 47.0 Gy) and the total lung ($TD_{50,5}$: 24.5 Gy) were the major organs vulnerable to the radiation toxicity; however this technique was successful in preserving a large fraction of the heart ($TD_{50,5}$: 50.6 Gy) and spinal cord ($TD_{50,5}$: 66 Gy) in the 3DCRT treatment of the left-lung cancer patients.

Lung cancer screening by PET/CT dual imaging modality can also reduce the lung cancer deaths by detecting the disease at early stages. Modern radiotherapy treatment techniques have also dramatically reduced the toxicity in various organs and the cardiovascular complications. Studies have also shown that the reduction in heart volume receiving 30 Gy can be achieved in patients with left sided breast and lung cancers using moderate deep inspiration breath-holds assisted with an active breathing control device. The average number of breath-holds needed is typically 2.5 per beam direction (4-6 per 3DCRT treatment of left-breast cancer) with a median duration of 22 seconds per breath-hold.

5.2 Evaluation of the universal plan-indices in the radiation therapy treatments

A radiotherapy treatment plan needs to be optimized to achieve the goal in cancer-treatment. The technique of evaluating the UPIs and QF of the radiotherapy treatment plans are the most practical approach in making critical decisions in the treatments. Plan indices and QFs were analyzed in the IMRT treatment of the 5 head and neck cancer patients, the IMRT treatment of the 10 prostate cancer patients, 3DCRT and EBT treatments of the 5 left-breast cancer patients, and 3DCRT treatment of the 7 left-lung cancer patients respectively.

5.2.1 Plan indices evaluation in radiotherapy treatment of head and neck cancer patients

The UPIs and QFs were estimated for the three consecutive SqIB plans (PTV1 plan, PTV2 plan, and PTV3 plan respectively) designed at successive PDs (39 Gy, 15 Gy, and 17.3 ± 3.7 Gy

respectively) in the treatment of the head and neck cancer patients (N=5). Estimated indices for the respective plans are presented in Table 5.1.

Table 5.1 The computed values of the universal plan indices (UPIs) and Quality Factors (QFs) of the three major sequential IMRT boost (SqIB) plans designed for the treatment of the head and neck cancer patients (N=5).

Plans	QF	COSI	RCI	PITV	HI	CN	TVR	DG	NCI	MHI	TCI
PTV1	0.97	0.69	0.99	1.1	1.1	0.85	0.90	0.97	1.16	0.96	0.97
PTV2	0.91	1.0	0.99	1.15	1.1	0.80	0.86	0.96	1.22	0.97	0.96
PTV3	0.91	1.0	0.97	1.15	1.09	0.79	0.87	0.96	1.26	0.95	0.96

The mean values of UPIs and QFs of the three SqIB plans were determined systematically as shown below in Fig. 5.2.

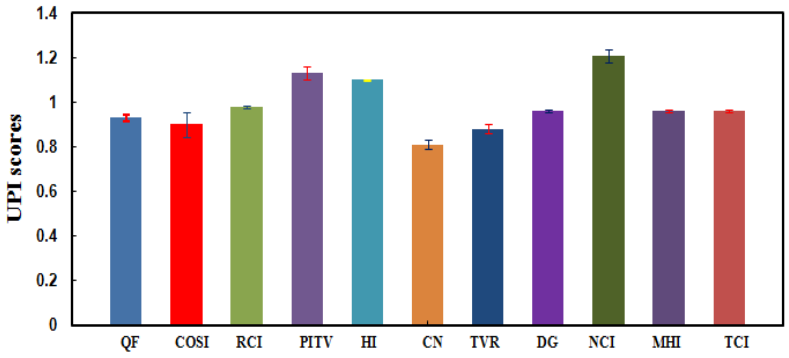

Fig. 5.2 Mean values of the universal plan indices (UPIs) and the Quality Factors (QFs) of the three sequential IMRT boost (SqIB) plans designed for the external beam radiation therapy (XRT) treatment of the head and neck cancer patients (N=5).

Similarly, the target volumes were 1592.8 ± 487.1 cc (N=5; CI= 0.95), 864.9 ± 478.1 cc (N=5; CI= 0.95), and 364.4 ± 194.4 cc (N=5; CI= 0.95) for the three PTVs (PTV1, PTV2 and PTV3 respectively) contoured in the CT scans for the given head and neck cancer patients.

5.2.2 Plan indices evaluation in radiotherapy treatment of prostate cancer patients

UPIs and QFs were analyzed for the three consecutive SqIB plans (PTV1, PTV2, and PTV3 plans respectively) designed at the PDs (14.4 Gy, 10.3 ± 0.8 Gy, and 5.3 ± 2.5 Gy respectively) for the prostate cancer patients (N=10) as presented in Table 5.2. Mean values of the UPIs and QFs of the three SqIB plans were systematically determined in 95% CI as shown in Fig. 5.3 [38].

Table 5.2 The computed values of the universal plan indices (UPIs) and Quality Factors (QFs) of the three sequential IMRT boost (SqIB) plans designed in the treatment of the prostate cancer patients (N=10).

Plans	QF	COSI	RCI	PITV	HI	CN	TVR	DG	NCI	MHI	TCI
PTV1	0.99	1.0	0.99	1.14	1.10	0.84	0.86	0.99	1.16	0.95	0.99
PTV2	0.99	1.0	0.99	1.10	1.10	0.88	0.90	0.99	1.11	0.95	0.99
PTV3	1.00	1.0	0.98	0.99	1.08	0.97	1.01	0.98	1.03	0.94	0.98

The target volumes were 318.25 ±44.20 cc (N=10; CI=0.95), 210.98 ±20.55 cc (N=10; CI=0.95), and 71.1 ±12.2 cc (N=10; CI=0.95) for the 3 PTVs (PTV1, PTV2 and PTV3 respectively) in the CT images.

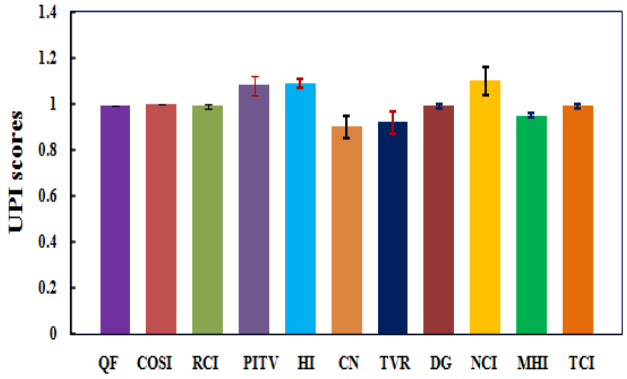

Fig. 5.3 Mean values of the Universal Plan Indices (UPIs) and Quality Factors (QFs) of the 3 sequential IMRT boost (SqIB) plans in radiotherapy treatment of prostate cancer patients (N=5).

5.2.3 Plan indices evaluation in radiotherapy treatment of the left-breast cancer patients

The UPIs and QF were analyzed in the COMPOSITE plan of the 3DCRT and EBT treatments designed at cumulative PD of 55.6 ± 5.0 Gy for the 5 left-breast cancer patients (N=5). Mean values of the UPIs and QF were systematically determined as presented in Fig. 5.4. The mean volume of the tumor bed was 12.2 ±7.4 cc (N=5; CI=0.95) in the CT scans of the cancer patients.

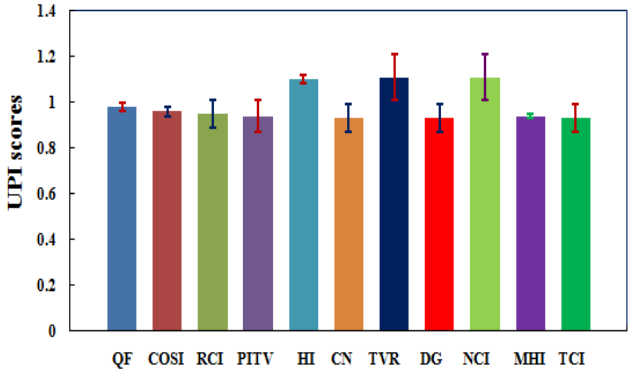

Fig. 5.4 Mean values of the Universal Plan Indices (UPIs) and Quality Factor (QF) of the COMPOSITE plans designed in the three dimensional conformal radiation therapy (3DCRT) treatment of the left-breast cancer patients (N=5).

5.2.4 Plan indices evaluation in radiotherapy treatment of left-lung cancer patients

The UPIs and QF were analyzed to evaluate the homogeneity and conformality in the 3DCRT treatment of the 7 left-lung cancer patients (N=7) at mean PD of 55.4 ± 3.5 Gy. Mean values of the UPIs and QF were systematically determined in the COMPOSITE plans at 95% CI as shown in Fig. 5.5. Mean volume of the targets was observed to be 746.03 ± 270.25 cc (N=7; CI= 0.95) in the CT scans of the left-lung cancer patients (N=7).

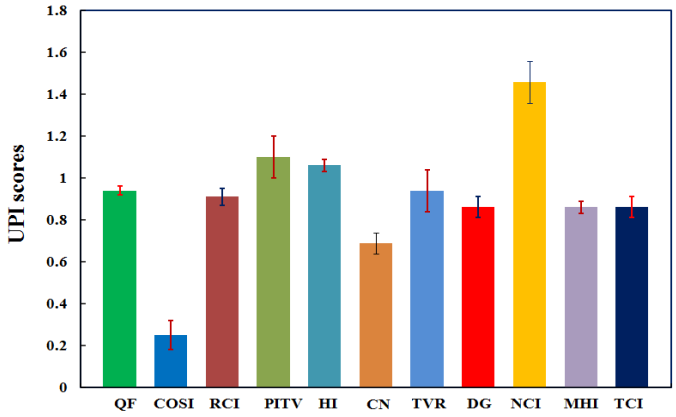

Fig. 5.5 Mean values of the universal plan indices (UPIs) and the Quality Factor (QF) of the COMPOSITE plans in the 3D conformal radiation therapy (3DCRT) treatment of the left-lung cancer patients (N=7).

In general, the computed values of QFs were 0.93 ± 0.03 (N = 5; CI = 0.95), 0.99 ± 0.00 (N= 10; CI = 0.95), 0.98 ± 0.04 (N = 5; CI = 0.95), and 0.94 ± 0.04 (N= 7; CI = 0.95) in the corresponding radiotherapy treatment plans of the head and neck cancer patients, prostate cancer patients, left-breast cancer patients, and left-lung cancer patients respectively. The smaller values of the QF showed that the radiation toxicity is inevitable in the IMRT treatment of the head and neck cancer patients, and the 3DCRT treatment of the left-lung cancer patients respectively. The critical organs such as (a) heart, esophagus, lungs, and (b) parotid glands, larynx, submandibular glands were found to be significantly vulnerable to the radiation toxicity in the treatment of the (a) left-lung cancer patients, and (b) head and neck cancer patients respectively. Hence the complex geometry of the target and the constraint of the neighboring organs could result in the overdose treatments (QF< 1) in the IMRT treatment of the head and neck cancer patients and the 3DCRT treatment of left-lung cancer patients respectively.

5.3 Cumulative dose-volume histogram (DVH) analysis in radiotherapy treatments

DVH is a strong tool to evaluate the radiotherapy treatment plans and to assess the outcome of the advanced radiation therapy treatments. Two different types of DVH models (cDVH and sDVH respectively) were utilized to determine the dose-volume coefficients to assess the plans and the primary cause of complications in the critical organs respectively, in the treatments.

The cumulative DVH (cDVH) analyses were performed in the SqIB treatment of 38 head and neck cancer patients and the SIB treatment of 3 head and neck cancer patients, the conventional 4-FD box treatment and the SqIB treatment of 10 prostate cancer patients, the 3DCRT treatment of 8 left-breast cancer patients, and the 3DCRT treatment of 8/8 left-lung cancer patients for the curative and palliative intent utilizing the CERR and the HART programs.

5.3.1 Cumulative DVH analysis in the treatment of head and neck cancer patients

The cDVH analyses were performed in the target (GTV) and other 14 neighboring critical organs in the SqIB treatment of the head and neck cancer patients using the COMPOSITE plans at mean PD of 72.52 ± 0.73 Gy (N=38). The relative distribution of the dose-volume coverage in the PTV1, PTV2, PTV3 and GTV targets, and the 6 major critical structures is also presented in Fig. 5.6 (a) in the corresponding SqIB treatment plans respectively. The relative distribution of the dose-volume coverage in the GTV and the 14 critical structures is also presented in Fig. 5.6 (b) and Fig. 5.6 (c) in the COMPOSITE SqIB treatment plans.

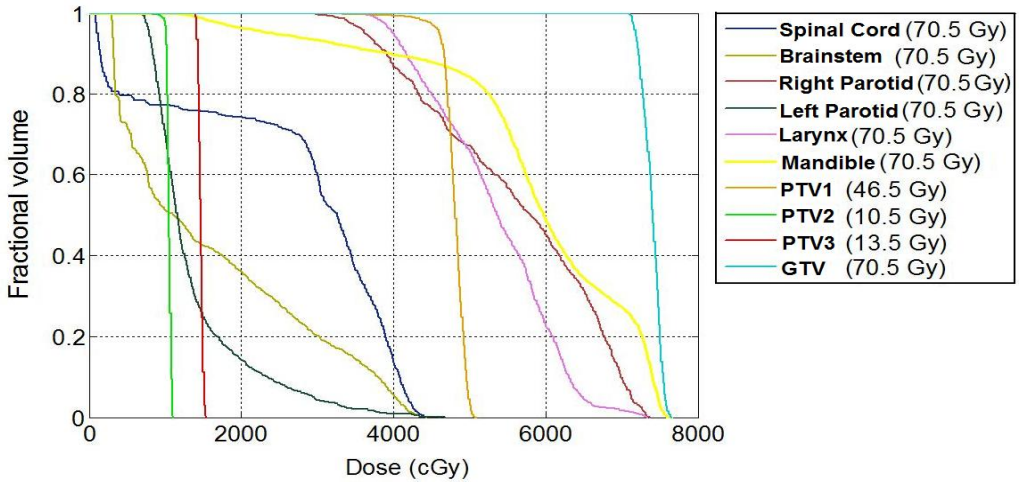

Fig. 5.6 (a) Relative dose-volume coverage in Planning Target Volumes (PTV1, PTV2 and PTV3 respectively), Gross Tumor Volume (GTV), and the various critical organs in the neighborhood of the target in the sequential IMRT boost (SqIB) treatment plans (PTV1, PTV2, PTV3 and COMPOSITE plans respectively) in the treatment of a head and neck cancer patient.

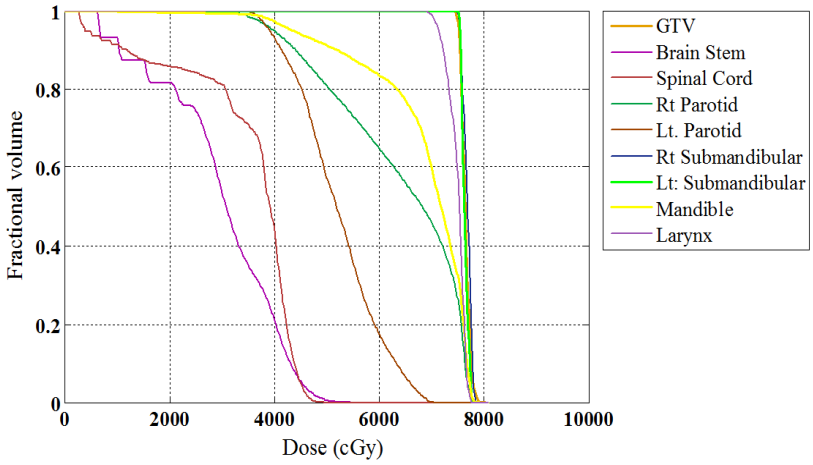

Fig. 5.6 (b) Relative dose-volume coverage in various critical organs and Gross Tumor Volume (GTV) in the COMPOSITE sequential IMRT boost (SqIB) treatment plan of a typical head and neck cancer patient at the prescription dose (PD) of 73.5 Gy.

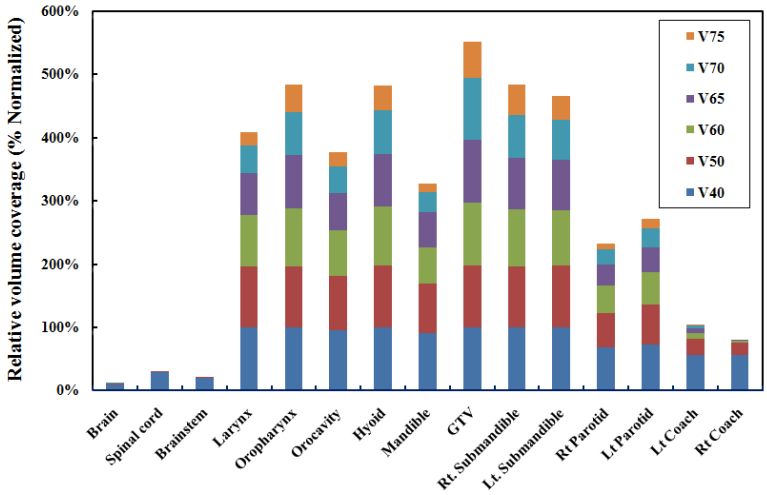

Fig. 5.6 (c) Relative dose-volume coverage in various organs and Gross Tumor Target (GTV) in the sequential IMRT boost (SqIB) treatment of the head and neck cancer patients (N=38).

The relative dose-volume coverage for the 15 neighboring organs and the GTV were also estimated in the COMPOSITE plans at the corresponding PDs of the targets and the corresponding $TD_{50,5}$'s for the large volume dependence of the critical organs in the head and neck cancer patients treated with the SqIB techniques (N=38) as shown in the Fig. 5.7, and the SIB techniques (N=3) as shown in Fig. 5.8 respectively. In the pretext of the usual practice of SIB treatment of head and neck cancer patients at high dose rate of 2.0-2.2 Gy per fraction at a large number of medical institutions, it is important to establish an alternative mechanism of IMRT treatments such as SqIB to spare the critical organs using the smaller dose-rate hyper-fractionation treatment techniques such as 1.5 Gy per fraction in such types of treatments.

In the study, the volumes of the contoured regions were found to be 24.88 ±1.54 cc (N=38; CI: 0.95) in the left parotid gland, 26.55 ±1.79 cc (N=38; CI: 0.95) in the right parotid gland, 8.31 ± 0.47 cc (N=38; CI: 0.95) in the left submandibular gland, 8.33 ± 0.47 cc (N=38; CI: 0.95) in the right submandibular gland, 11.6 ± 1.5 cc (N=38; CI: 0.95) in ct-esophagus, and 37.59 ±1.84 cc (N=38; CI: 0.95) in the larynx respectively, in the SqIB treatment plans.

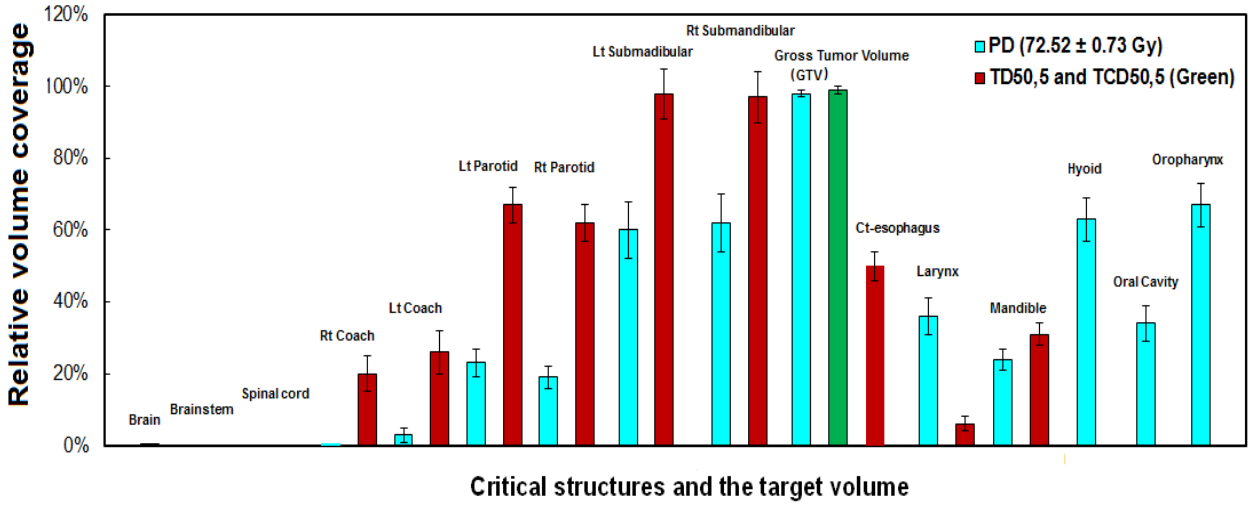

Fig. 5.7 Relative dose-volume coverage in the 15 critical organs and the Gross Tumor Volume (GTV) in the sequential IMRT boost (SqIB) treatment of the head and neck cancer patients at PD of 72.52 ± 0.73 Gy (N=38), at the tumor control dose ($TCD_{50,5}$; 63.8 Gy) of the GTV, and at the corresponding tolerance dose ($TD_{50,5}$) of the critical organs respectively.

As shown above in Fig. 5.7, the relative volume coverage for the left submandibular gland (98.0 ± 2.0 % ; N=38; CI: 0.95), right submandibular gland (97.1± 2.0 % ; N=38; CI: 0.95), left parotid gland (67.0 ± 8.0 %; N=38; CI: 0.95), right parotid gland (62.0 ± 8.0 %; N=38; CI: 0.95) and larynx (45.1 ± 10.0% ; N=38; CI: 0.95) were found to be critical of losing its functionality due to the exposure of the corresponding organs to the radiations at the minimum $TD_{50,5}$ respectively. Ideal dose-volume constraint typically requires a minimum fraction of 50% volume coverage at the dose lower than 30 Gy to preserve the parotid and submandibular glands. Mean dose of less than 26 Gy is currently recommended by some investigators, for the parotid glands to receive the best functional outcomes following the radiation therapy treatments.

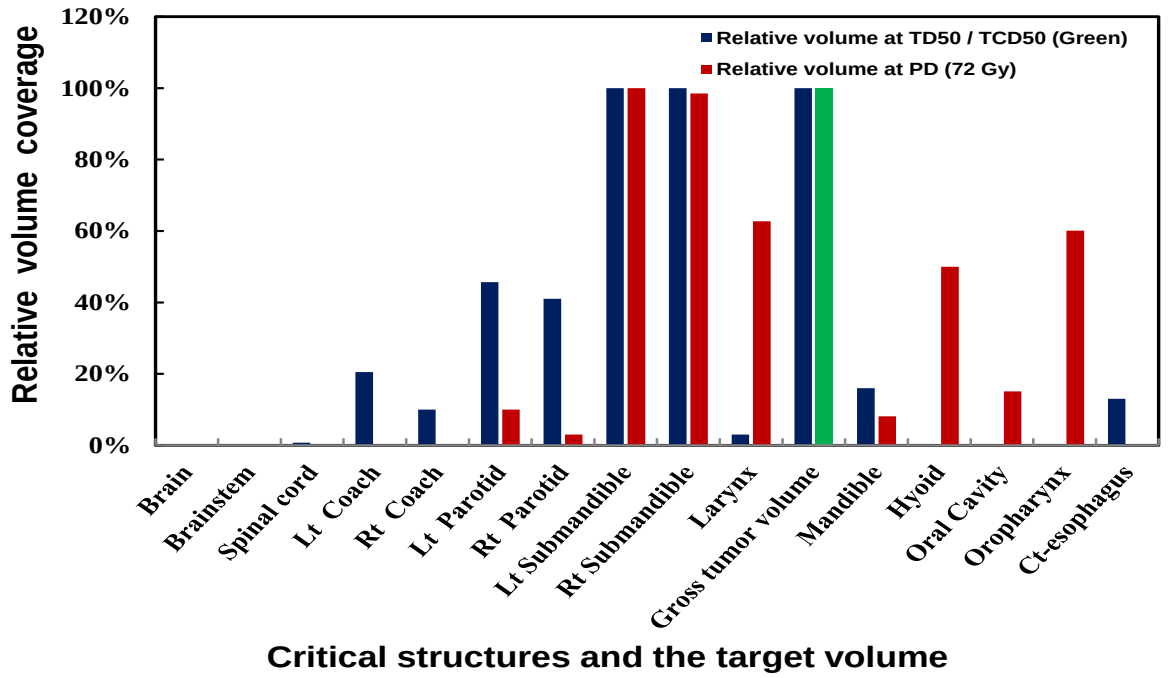

Fig. 5.8 Relative dose-volume coverage in the 14 critical organs and the Gross Tumor Volume (GTV) in the simultaneous integrated boost (SIB) treatment of the head and neck cancer patients at the prescription dose (PD) of 72 Gy (N=3), at the tumor control dose ($TCD_{50,5}$; 63.8 Gy) of the GTV, and at the corresponding tolerance dose ($TD_{50,5}$) of the critical organs.

Clinical benefit of the submandibular gland sparing is more controversial. Studies have shown that a mean dose less than 40 Gy could preserve the submandibular gland functions. It is not yet clear whether the parotid and submandibular glands have the same dose-volume characteristics in the radiation based treatments. Although some experimental data suggests that the submandibular glands may be somewhat more sensitive to the fractionated radiotherapy than the parotid glands, their radiosensitivity is not likely to differ markedly from that of other salivary glands. Specific skills on salivary glands sparing could significantly decrease the oral complications such as lack of saliva, alteration in tastes, and sensation of dryness, in the XRT treatment of the head and neck cancer patients.

Furthermore, the relative volume coverage were also found to be greater than 40% (N=3) in parotid glands, submandibular glands, and larynx at the corresponding $TD_{50,5}$ of the critical organs in SIB treatments [36]. A comparison of a complete set of PTVs contoured in SqIB (N=38) plans (PTV1, PTV2, and PTV3 plans) and SIB (N=3) plans (PTV1, PTV2, and PTV3 plans) is also presented in Fig. 5.9 at the corresponding PDs respectively.

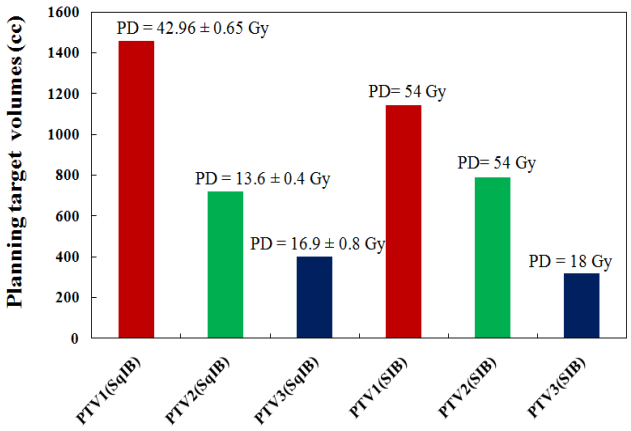

Fig. 5.9 A comparison of the planning target volumes (PTV1, PTV2, and PTV3 respectively) contoured in the sequential IMRT boost (SqIB; N=38) plans and simultaneous integrated boost (SIB; N=3) plans designed for the treatment of head and neck cancer patients.

5.3.2 Cumulative DVH analysis in treatment of the prostate cancer patients

The cDVH analyses were performed in the GTV and the rectum and bladder, in the PELVIS plan using the conventional 4-FD box technique at PD (45 Gy; N=10), and the three SqIB plans (PTV1, PTV2, and PTV3 plans respectively) at PDs (12.6 ± 2.5 Gy, 10.35 ± 0.83 Gy, and 5.05 ± 1.00 respectively) in the treatment of the prostate cancer patients (N=10). Ideal dose-volume constraint limits a maximum of 60% (5%) volume coverage at excess of 30 Gy (80 Gy) dose in rectum, and a maximum of 35% (20%) volume coverage greater than 45 Gy (70 Gy) dose in bladder. The relative distribution of the dose-volume coverage in GTV, rectum and bladder is

also presented in Fig. 5.10 in the four different plans at 50% PD. The volume of the rectum and bladder were 93.5 ±11.1 cc (N=10; CI: 0.95) and 241.5 ±72 cc (N=10; CI: 0.95) respectively.

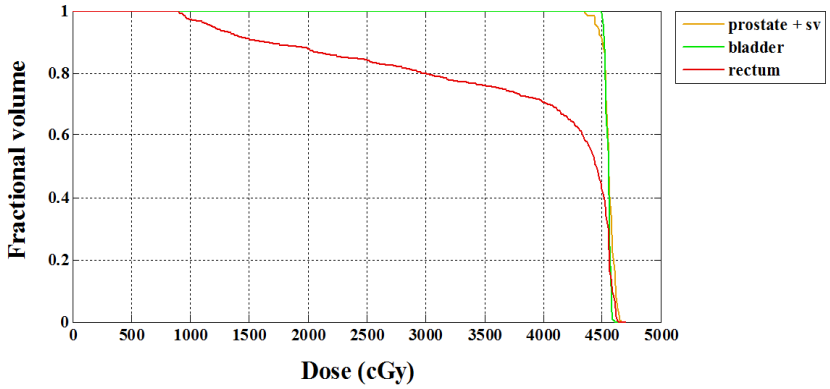

Fig. 5.10 (a) Relative dose-volume coverage in Gross Tumor Volume (GTV), and in the neighboring critical organs (rectum and bladder) in a conventional 4-field (4FD) treatment of a typical prostate cancer patient at the prescription dose (PD) of 45 Gy.

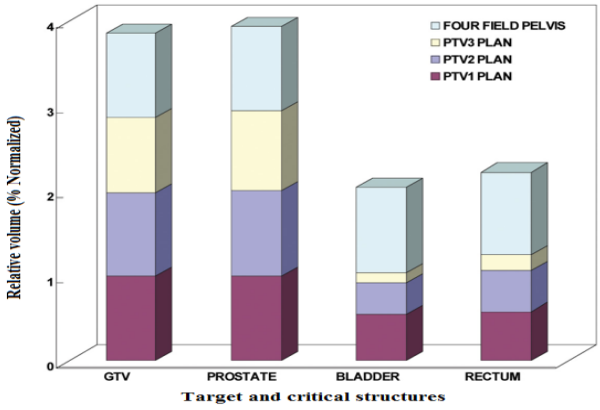

Fig. 5.10 (b) A statistical analysis of HART extracted dose-volume histogram (DVH) data points for the normalized volume coverage at 50% prescription dose (PD) for the targets - Gross Tumor Volume (GTV) and prostate, and two major critical structures (rectum and bladder) contoured in the four field (4-FD) box plan in the treatment of 10 prostate cancer patients at PD of 45 Gy in combination with the sequential IMRT boost plans (PTV1, PTV2, and PTV3 respectively) at corresponding PDs (12.6 ± 2.5 Gy, 10.35 ± 0.83 Gy, and 5.05 ± 1.00 Gy respectively) [31].

5.3.3 Cumulative DVH analysis in the treatment of the left-breast cancer patients

The cDVH analyses were also performed in the tumor bed (TB) and the neighboring critical organs such as left-lung and heart, in the hyper-fractionated scheme of the whole breast irradiation treatment of the 8 left-breast cancer patients using the COMPOSITE plans at the cumulative PD of 56.05 ± 5.23 Gy (N=8). DVH constraint requires minimizing the irradiated ipsilateral lung volume receiving greater than 20 Gy (V20) to less than 25%, and mean lung dose to less than 15 Gy, and the heart volume receiving greater than 30 Gy (V30) to less than 10% respectively. The relative distribution of the dose-volume coverage was also estimated from the cDVH curves of the heart and left-lung at the corresponding $TD_{50,5}$ of the organs in these plans.

The total volume of the heart and left-lung contoured in the plans were 275.8 ± 48.6 cc (N=8; CI= 0.95) and 1313.3 ± 69.8 cc (N=8; CI= 0.95) respectively. It was observed that the radiation toxicity can be avoided in the left-lung since the relative dose-volume coverage at $TD_{50,5}$ was limited to 0.13 ± 0.04 (N=8; CI= 0.95) in the accelerated whole breast irradiation technique as shown in Fig. 5.11. The relative volume coverage was found to be in good agreement with the critical dose-volume constraint of the ipsilateral lung in the treatments.

5.3.4 Cumulative DVH analysis in the treatment of left-lung cancer patients

The cDVH analyses were performed in the target (PTV), total lung, heart, spinal cord and thoracic esophagus, in the 3DCRT treatment of 8 left-lung cancer patients using the COMPOSITE plans designed at the cumulative PD of 54.77 ± 3.33 Gy (N=8; CI=0.95) and the hyper-fractionation scheme. The relative distribution of the dose-volume coverage at $TD_{50,5}$ were also estimated from the cDVH curves of the organs in the COMPOSITE plans designed for the curative treatment as discussed earlier in Fig. 5.1.

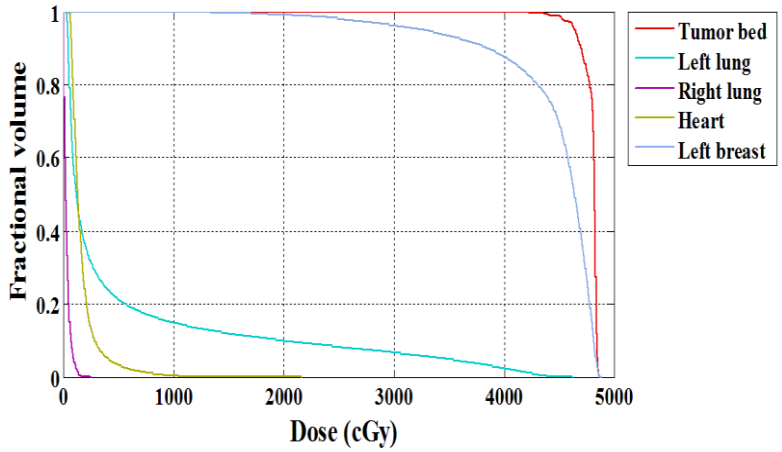

Fig. 5.11(a) Relative dose-volume coverage in tumor bed (TB), left-lung and heart in the three dimensional conformal radiotherapy (3DCRT) treatment of a typical left-breast cancer patient.

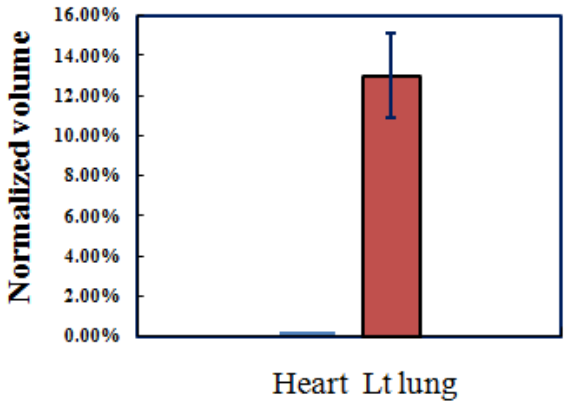

Fig. 5.11(b) Dose-volume coverage at tolerance dose ($TD_{50,5}$) of the heart and left-lung in the COMPOSITE plan designed in the treatment of the left-breast cancer patients using the combined three dimensional conformal radiation therapy (3DCRT) and electron beam therapy (EBT) at the cumulative PD (56.05 ± 5.23 Gy; N=8; CI= 0.95).

DVH constraint recommends the relative volume, V (50 Gy), less than 25% and mean dose less than 25 Gy in esophagus ($TD_{50,5}$; 47Gy) to avoid the complications in the organ. The

volumes of the contours were found to be 520.9 ± 131.5 cc (N=8; CI = 0.95) in the heart, 24.9 ± 4.6 cc (N=8; CI = 0.95) in the spinal cord, 2957.4 ± 485.2 (N=8; CI = 0.95) in the total-lung, and 25.5 ±4.3 cc (N=8; CI=0.95) in the esophagus respectively, in the PET/CT image fusion.

Furthermore, the cDVH analyses were also performed to estimate the relative dose-volume coverage at $TD_{50,5}$ in the lung, heart, spinal cord and thoracic esophagus, in the COMPOSITE plan designed at the mean PD of 31.0 ± 1.8 Gy (N=8; CI= 0.95) in the APPA treatment of the 8 left-lung cancer patients for the palliative intent using the hyper-fractionated scheme as shown in Fig. 5.12. The volume of the contours were found to be 511.35 ± 73.7 cc (N=8; CI = 0.95) in the heart, 24.92 ± 4.4 cc (N=8; CI = 0.95) in the spinal cord, 2197.3 ± 708.5 cc (N= 8; CI = 0.95) in the total lung, and 22.26 ± 1.51 cc (N=8; CI= 0.95) in the esophagus respectively, in the PET/CT image fusion.

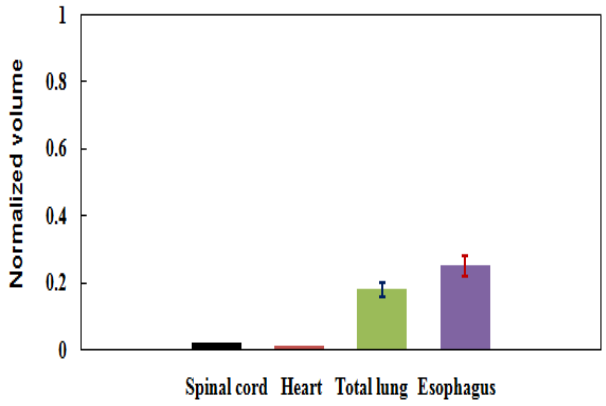

Fig. 5.12 Dose-volume coverage at tolerance dose ($TD_{50,5}$) of the heart, spinal cord, total lung, and esophagus in the external beam radiation therapy (XRT) treatment plan designed for the palliative treatment of the left-lung cancer patients using anteroposterior / posteroanterior (APPA) techniques at the average prescription dose (PD : 31.0 ± 1.8 Gy; N=8).

5.4 Biological modeling and outcome analysis in the radiation therapy treatments

The outcomes of the radiotherapy treatments were assessed in the SqIB treatment of 10 head and neck cancer patients, the conventional 4-FD box treatment of the10 prostate cancer patients, the 3DCRT treatment of the 8 left-breast cancer patients, and the 3DCRT treatment of the 8 left-lung cancer patients for curative and palliative purposes using the biological models such as TCP and NTCPs respectively.

5.4.1 Biological modeling in the treatment of head and neck cancer patients

The NTCP and TCP indices were computed in the SqIB treatment plans of the 10 head and neck cancer patients using the COMPOSITE plan at PD of 73.5 Gy. The TCPs were computed in the PTV3 target using the Poisson statistics model, and the NTCPs were also computed in the parotid glands, submandibular glands, ct-esophagus, and larynx respectively, using the JT Lyman model for the homogeneous medium as shown in Fig. 5.13.

The cell killing parameters were appropriately chosen as TCD50 (63.8 Gy) and γ50 (2) to compute the TCP of the target (PTV3) using the Poisson statistics model in the corresponding plans. Furthermore, the complications in the normal tissue organs were also examined by using the cell survival parameters: (a) $TD_{50,5}$ (46 Gy), γ50 (2.22), n(0.7) for the parotid gland and submandibular glands, (b) $TD_{50,5}$ (47 Gy), γ50 (1.11), n(0.69) for the ct-esophagus and (c) $TD_{50,5}$(80 Gy), γ50(5.32), n(0.11) for the larynx in JT Lyman model for the homogeneous medium. NTCP indices for these organs were also computed in the constituent plans (PTV1, PTV2, and PTV3 plans respectively) as presented below in Table 5.3.

A group of radiation oncologists has also reported the clinical outcomes of the SqIB treatments administered on 83 head and neck cancer patients at the NMH Laurie cancer center. The report indicates that 13% patients diagnosed at stage III and 74% patients diagnosed at stage

IV disease were primarily involved in the 5 year (2002-2008) follow up study. The outcomes of the treatments were systematically analyzed for the 8 patients receiving post-operative radiation, 6 receiving radiation alone, 49 receiving radiation and chemotherapy, and 20 receiving surgery, radiation and chemotherapy. Sites included were larynx (14), nasopharynx (7), oral cavity (5), oropharynx (45), hypo-pharynx (5) and unknown primary (7). Unfortunately, the study showed the existence of a large number of the worst chronic toxicities and organ failures in the patients following the SqIB treatments, such as skin damage (8%), swallowing dysphagia (18%), weight loss (26%), and the complication in the salivary glands (32%) respectively, as mentioned in Table 5.3 [39].

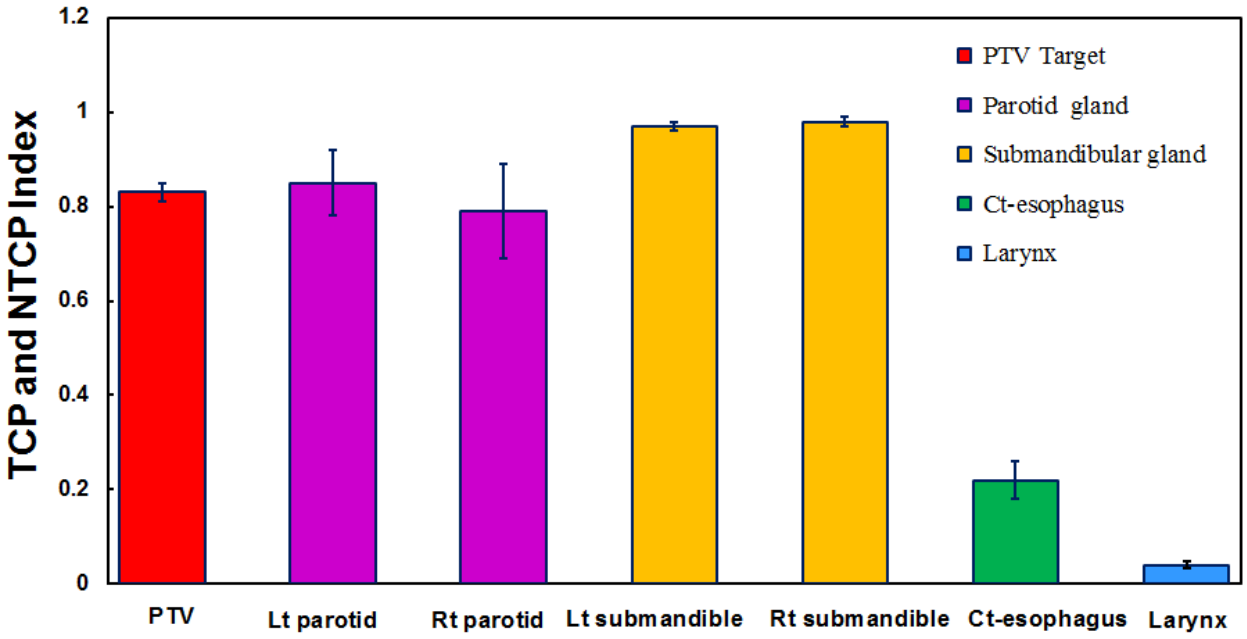

Fig. 5.13 Assessment of the biological modeling based outcome analysis indices, tumor control probability (TCP) and normal tissue complication probability (NTCP), in the sequential intensity modulated radiation therapy (IMRT) boost (SqIB) treatment of the head and neck cancer patients (COMPOSITE Plan; PD: 73.5 Gy; N=10). PTV implies the target volume (PTV3).

The TCP was estimated to be 0.83 ± 0.05 (N=10; CI: 0.95) in the SqIB treatment of the head and neck cancer patients. Similarly the NTCP indices showed that the submandibular glands (0.97 ± 0.02 and 0.98 ± 0.01; N=10; CI: 0.95), the parotid glands (0.85 ± 0.14 and 0.79 ± 0.20; N=10; CI: 0.95), and the ct-esophagus (0.22 ± 0.08; N=10; CI: 0.95) were the major critical organs prone to the radiation toxicity as compared to the other neighboring organs such as larynx and mandible in the COMPOSITE plans. Parotid and submandibular glands produce approximately 60% and 20% of the saliva respectively, while the rest is secreted by the sublingual and accessory glands.

Table 5.3 The computed and observed* values of the normal tissue complication probability (NTCP) of the salivary glands, cervico-thoracic esophagus, and the larynx in the sequential IMRT boost (SqIB) treatment of the head and neck cancer patients (N=10 and N*=83 respectively) using the IMRT plans (PTV1, PTV2, PTV3 and COMPOSITE plans respectively) at the prescription doses (PDs) of 41 ± 3.2, 13.9 ± 1.9, 16.9 ± 4.2 Gy, and 73.5 Gy respectively.

Critical organs	NTCP					
	COMPOSITE Plan	PTV1 plan	PTV2 plan	PTV3 plan	Mean	*Observed
Left parotid gland	0.85 ± 0.14	0.06 ± 0.02	< 0.01	< 0.01	0.45 ± 0.14	0.32
Right parotid gland	0.79 ± 0.20	0.07 ± 0.02	< 0.01	< 0.01	0.43 ± 0.20	0.32
Left submandibular gland	0.97 ± 0.02	0.24 ± 0.04	< 0.01	< 0.01	0.60 ± 0.04	0.32
Right submandibular gland	0.98 ± 0.01	0.23 ± 0.03	< 0.01	< 0.01	0.60 ± 0.03	0.32
Larynx	0.04 ± 0.01	< 0.01	< 0.01	< 0.01	0.03 ± 0.01	-
Ct-esophagus	0.22 ± 0.08	0.13 ± 0.04	< 0.01	< 0.01	0.17 ± 0.09	0.18

5.4.2 Biological modeling in the treatment of prostate cancer patients

TCP-NTCP indices were computed in the 4-FD box plan at PD of 45 Gy, and the 3 SqIB plans (PTV1, PTV2, and PTV3 plans respectively) at the PDs (12.6 ± 2.5 Gy, 10.4 ± 0.8 Gy, and 5.1 ± 1.0 Gy respectively) designed to treat the 10 prostate cancer patients as shown in Table 5.4.

Table 5.4 The computed values of tumor control probability (TCP) of Gross Tumor Volume (GTV), and normal tissue complication probability (NTCP) of the organs in the radiotherapy treatment of the prostate cancer patients (N=10) using the conventional 4 field box technique to treat the PELVIS at prescription dose (PD) of 45 Gy (N=10), and the sequential intensity modulated radiation therapy boost (SqIB) technique to treat the Planning Target Volumes (PTVs) at PDs of 12.6 ±2.5 Gy, 10.4 ±0.8 Gy and 5.1 ± 1.0 Gy respectively, for the 10 patients.

	TCP	NTCP			
Structures	PELVIS Plan	PELVIS Plan	PTV1 plan	PTV2 plan	PTV3 plan
GTV	0.66 ± 0.03	-	-	-	-
Rectum	-	< 0.01	< 0.01	< 0.01	< 0.01
Bladder	-	< 0.01	< 0.01	< 0.01	< 0.01

The appropriate cell killing parameters were chosen as $TCD_{50,5}$ (38.9 Gy), γ50(0.74) in order to compute the TCP in GTV using Poisson statistics model, and the complications in normal tissue organs were also examined on using the cell survival parameters $TD_{50,5}$(80 Gy), γ50 (2.66), n(0.12) in rectum, and $TD_{50,5}$(80 Gy), γ50(3.63), n(0.5) in JT Lyman model for the bladder respectively.

5.4.3 Biological modeling in the treatment of left-breast and left-lung cancer patients

The TCP-NTCP indices were computed in the COMPOSITE plans designed in the accelerated whole breast 3DCRT treatment of the left-breast cancer patients (N=8) at the mean PD of 56.05 ± 5.23 Gy. The appropriate cell killing parameters were chosen as $TCD_{50,5}$(39.3 Gy) and γ50(1.7) to compute TCP using Poisson statistics model in left-breast tumor targets as shown in Fig. 5.14, and the NTCPs were also computed for the neighboring critical organs using the KB model as presented in Table 5.5.

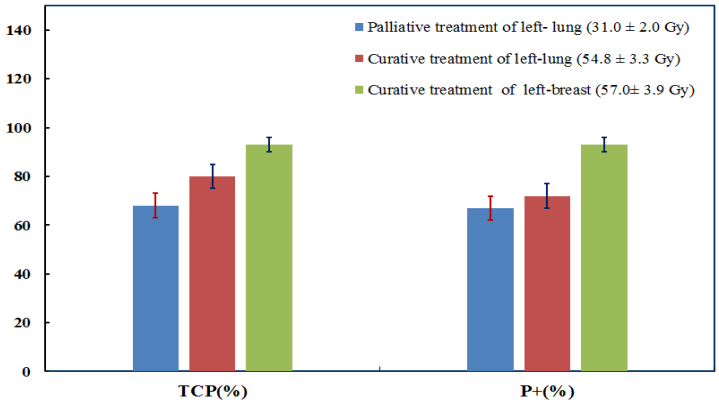

Fig. 5.14 Tumor control probability (TCP) and the uncomplicated cure probability (P+) in the three dimensional conformal radiation therapy (3DCRT) treatment of the left-breast cancer patients (N=8) and left-lung cancer patients (N=8).

In the left breast treatments, KB model employed the appropriate cell survival parameters as $TD_{50,5}$ (24.5 Gy), γ50 (2.22), n(0.87) for the left-lung, and $TD_{50,5}$(50.6 Gy), γ50 (3.07), n(0.64) for the heart respectively. The volume of the contours were found to be 275.8 ± 48.6 cc (N=8; CI = 0.95) in the heart, and 1313.3 ± 69.8 cc (N=8; CI= 0.95) in the left-lung respectively, in the COMPOSITE radiation therapy treatment plans.

Similarly TCP-NTCP indices were also computed in the two different cases of 3DCRT plans at PD of 54.77 ± 3.33 Gy and 31.0 ± 2.0 Gy, in the curative and palliative treatments of the left-lung cancer patients (N=8) respectively. The appropriate cell killing parameters were chosen as $TCD_{50,5}$ (51.24 Gy) and γ50 (0.83) for curative intent, and $TCD_{50,5}$ (36.5 Gy) and γ50 (0.72) for palliative intent to compute TCP using the Poisson model in the ipsilateral lung tumors in the left side as shown above in Fig. 5.14, and the NTCPs were also computed in the neighboring critical organs using the KB model as presented earlier in Table 5.5. The KB model employed the appropriate cell survival parameters as $TD_{50,5}$ (24.5 Gy), γ50 (2.22), n (0.87) for the lung, $TD_{50,5}$ (50.6 Gy), γ50 (3.07), n (0.64) for the heart, $TD_{50,5}$ (47 Gy), γ50 (1.1), n (0.69) for the esophagus, and $TD_{50,5}$ (66.5 Gy), γ50 (2.28), n (0.05) for the spinal cord respectively.

Table 5.5 The computed values of the normal tissue complication probability (NTCP) of the heart, esophagus, left- and right-lung, and spinal cord using the COMPOSITE plans designed in the accelerated whole breast radiotherapy treatment of the left-breast cancer patients (N=8), and three dimensional conformal radiation therapy (3DCRT) treatment of left-lung cancer patients (N=8) for the curative and palliative intents respectively.

	NTCP				
3DCRT Treatments	Left-lung	Right lung	Heart	Spinal cord	Esophagus
Palliative (Left-lung)	< 0.01	< 0.01	< 0.01	< 0.01	< 0.01
Curative (Left-lung)	< 0.01	0.02	< 0.01	< 0.01	0.25 ± 0.02
Curative (Left-breast)	< 0.01	< 0.01	< 0.01	< 0.01	< 0.01

The volume of the contours were also found to be 24.9 ± 4.6 cc (N=8; CI=0.95) in the spinal cord, 520.9 ± 131.5 cc (N=8; CI=0.95) in the heart, 25.5 ± 4.3 cc (N=8; CI=0.95) in the esophagus, and 2957.4 ± 485.2 cc (N=8; CI=0.95) in the lung in the curative treatment of the left-lung cancer patients respectively. Similarly the volume of the contoured regions were 24.92 ± 4.4 cc (N=8) in spinal cord, 511.35 ± 73.7 cc (N=8) in heart, 22.26 ± 1.51 cc (N=8) in thoracic esophagus, and 2197.3 ± 708.5 cc (N=8) in the lung in the palliative treatment of the left-lung cancer patients respectively. The NTCP results of the critical organs suggest that special attention should be taken to preserve the normal functionality of the esophagus in the 3DCRT treatment of the left-lung cancer patients (N=8).

5.5 Spatial dose-volume histogram (sDVH) analysis in radiation therapy treatments

The sDVH (x-,y-, and z- DVHs) analyses were especially useful to determine the cause of complications in the various critical organs in the SqIB treatment of the 10 head and neck cancer patients, and the 3DCRT treatment of 9 non-small cell left-lung cancer patients.

5.5.1 Spatial DVH analysis in treatment of the head and neck cancer patients

Since the major critical organs such as parotid and submandibular glands, and larynx were found to be vulnerable to the radiation toxicity from the cDVH analyses and BMOA in the SqIB treatment of the 38 head and neck cancer patients, it was imperative to perform the x-, y-, and zDVH analyses respectively. The sDVH analyses were performed in the parotid glands and submandibular glands, and the ct-esophagus using the COMPOSITE plans designed at the cumulative PD of 73.5 Gy (N=10).

Critical spots indicate the relative dose-volume coverage at the corresponding $TD_{50,5}$ of a normal tissue organ. The hot spots (dose grids > 1.0PD) are generally acceptable to a margin of 20% volume in the PTVs as per the RTOG criteria; however the excess hot and critical spots in the critical organs are the principal cause of the complications in the organs in the radiation guided treatments. The volume coverage of the critical spots per unit slice were normalized relative to the gross volume of the corresponding organs such as parotid glands, submandibular glands, and the ct-esophagus in the SqIB treatment of the 10 head and neck cancer patients.

The relative volume coverage of the critical spots were estimated at high spatial resolution ($\delta x, \delta y, \delta z$ = 1 mm) in the discrete slices using the sDVH analysis. The relative volume coverage were (a) 0.16 ± 0.11 (0.97 ± 0.02 slices; N=10) along x-planes, 0.12 ± 0.08 (0.99 ± 0.01 slices; N=10) along y-planes, and 0.14 ± 0.07 (1 ± 0 slices; N=10) along z-planes in left submandibular gland respectively, (b) 0.14 ± 0.11 (0.99 ± 0.01 slices; N=10) along x-planes, 0.13 ± 0.08 (0.99 ± 0.01 slices; N=10) along y-planes, and 0.11 ± 0.1 (1.0 ± 0 slices; N=10) along z-planes in right submandibular gland respectively, (c) 0.08 ± 0.06 (0.88 ± 0.03 slices; N=10) along x-planes, 0.06 ± 0.05 (0.93 ± 0.04 slices; N=10) along y-planes, and 0.06 ± 0.05 (0.93 ± 0.03 slices; N=10) along z-planes in left parotid gland respectively, (d) 0.07 ± 0.05 (0.87 ± 0.04 slices; N=10) along x-planes, 0.06 ± 0.04 (0.94 ± 0.02 slices; N=10) along y-planes, and 0.05 ± 0.04 (0.93 ± 0.02 slices; N=10) along z-planes in right parotid gland respectively, and (e) 0.03 ± 0.01 (0.44 ± 0.05 slices; N=10) along z-planes in the ct-esophagus respectively, as shown in Fig. 5.15(b).

The sDVH statistics showed that the parotid glands, submandibular glands and ct-esophagus were significantly vulnerable to the radiation toxicity, and the chances of complications were found to increase with the depth of the penetration of radiation along the x-direction in the corresponding organs.

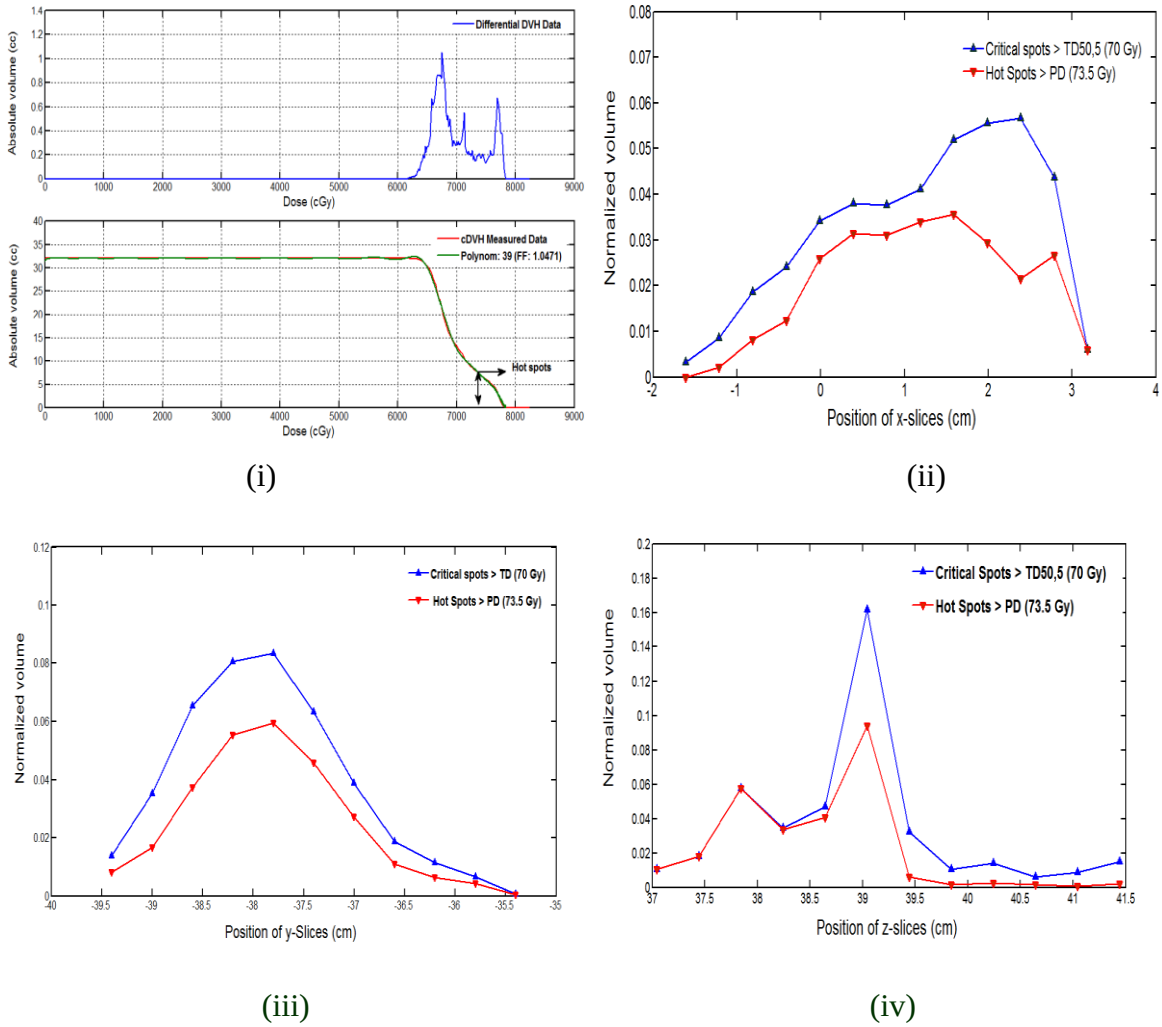

Fig. 5.15 (a) The volume of the critical spots and hot spots in the core structure of a typical organ, larynx in the sequential IMRT boost (SqIB) COMPOSITE plan designed for the treatment of a head and neck cancer patient using the spatial dose-volume histogram (sDVH) analysis at the tolerance dose ($TD_{50,5}$) of 70 Gy and prescription dose (PD) of 73.5 Gy respectively. (i) The cDVH analysis of the larynx (V_{PD}= 0.24 ± 0.02) is shown in DVH curve (bottom) derived from the differential DVH curve (top), (ii) The resolution of the x-component of the cDVH curve (xDVH) simulated for the larynx (V_{PD}= 0.26 ± 0.02), (iii) The resolution of the y-component of the cDVH curve (yDVH) simulated for the larynx (V_{PD} = 0.27 ± 0.02), and (iv) The resolution of the z-component of the cDVH analysis (zDVH) simulated for the larynx (V_{PD} = 0.26 ± 0.02).

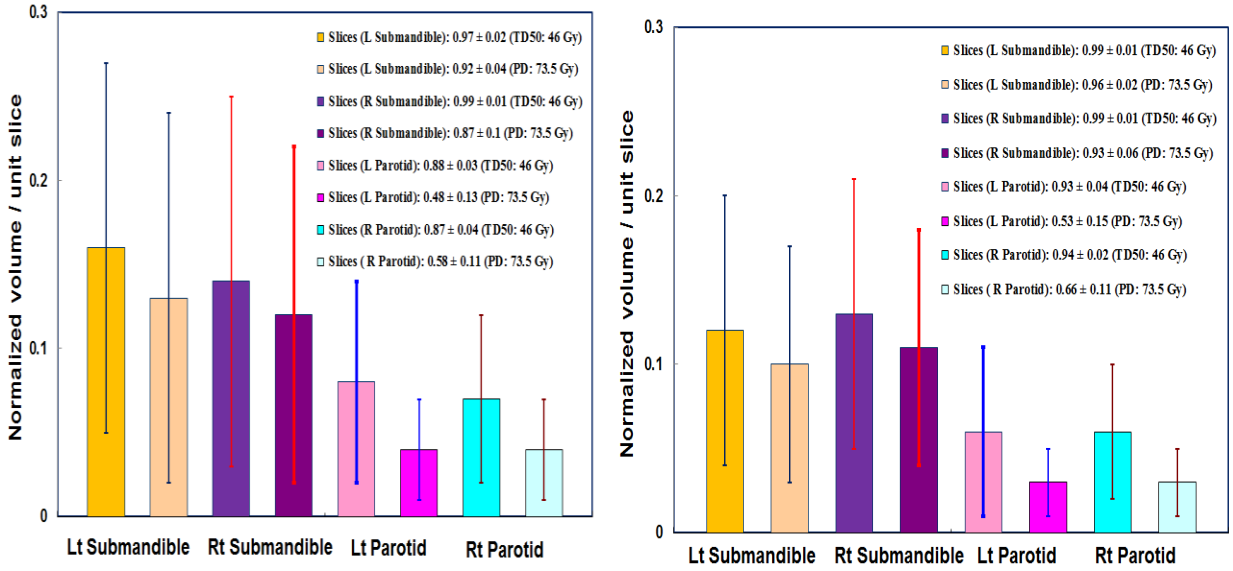

Fig. 5.15 (b) Statistical analysis of the relative volume coverage of the critical spots ($TD_{50,5}$) and hot-spots (PD) per unit slice of the left- and right- submandibular glands, left- and right- parotid glands, and ct-esophagus contoured in the 3D COMPOSITE plans designed for the sequential IMRT boost (SqIB) treatment of the head and neck cancer patients (N=10) at prescription dose (PD) of 73.5 Gy using (i) xDVH, (ii) yDVH, and (iii) zDVH analyses respectively.

5.5.2 Spatial-zDVH analysis in the treatment of the left-lung cancer patients

The critical organs such as heart, esophagus, left- and right-lungs, were found to be vulnerable to the radiation toxicity in the cDVH analysis of the organs in the 3DCRT treatment of the 9 left-lung cancer patients. An additional test was also performed using the zDVH analysis of the selective organs contoured in the COMPOSITE plans at PD of 55.3 ± 3.1 Gy (N= 9; CI= 0.95). The relative distribution of the dose-volume coverage at $TD_{50,5}$ of the neighboring critical organs (heart, left lung, right lung and esophagus) in the curative treatment of the left-lung cancer patients is also presented in Fig. 5.16.

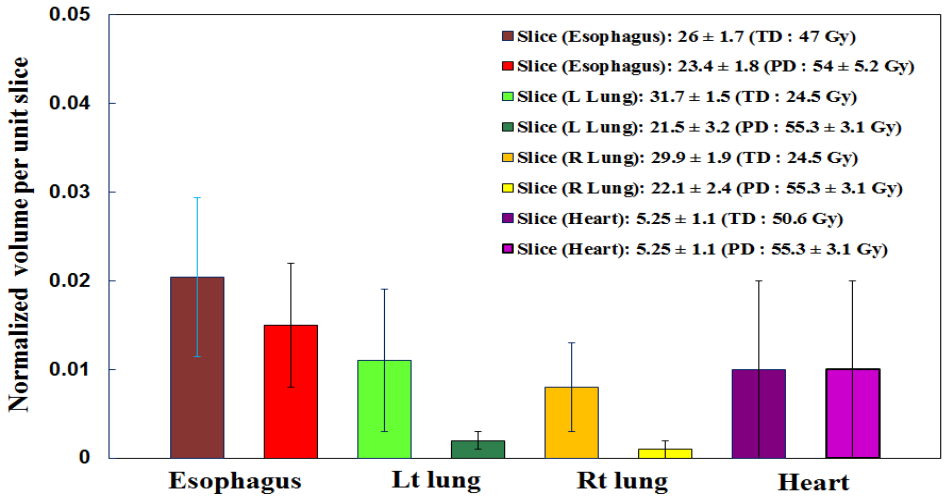

Fig. 5.16 Identification of the critical spots and hot spots in heart, esophagus, left-lung, and right-lung in the three dimensional conformal radiation therapy (3DCRT) treatment of the left-lung cancer patients (N=9) using the z-spatial dose-volume histogram (zDVH) statistics.

As shown in Fig. 5.14, the relative volume coverage of the critical spots in unit slice were found to be: (a) 0.02 ± 0.01 (26 ±1.7 slices; N=5) in esophagus, (b) 0.01 ± 0.01 (31.7 ± 1.5 slices; N=9) in left-lung, (c) 0.01 (29.9 ± 1.9 slices; N=9) in right-lung, and (d) 0.01 ± 0.01 (5.2 ±1.1 slices; N=9) in heart respectively, in the 3DCRT treatment of the left-lung cancer patients.

The effective ratio of the specific volume coverage of the hot spots to the critical spots (HC ratio per unit slice along z-axis) were estimated to be 0.75 ± 0.12 (N=5) for the esophagus, 0.22 ± 0.06 (N=9) for the left-lung, 0.14 ± 0.05 (N=9) for the right-lung, and 0.67 ± 0.18 (N=9) for the heart along the z-direction respectively. The results showed that the high precision radiation therapy techniques are imminent to avoid the radiation induced complications in the vital organs such as esophagus and heart, in the left-lung cancer treatments.

5.6 Chart analysis in the radiation therapy treatment of the various types of cancers

In general, various types of cancer patients are treated with adjuvant systematic therapy using radiation therapy as one of the major components in the clinical practice. It is essential to design the optimal treatment plans to treat the tumor targets sparing the critical organs using the IMRT and 3DCRT techniques. However, the critical organs in the neighborhood of the target always limit the efficiency of the radiation therapy treatments. Therefore, various types of DVH based models and UPI evaluation techniques were utilized to improve the quality of radiation therapy treatment plans in this study. The complication probabilities in the normal tissue organs were also estimated accurately using the dose-volume effects in the retrospective study of the IMRT treatment of the head and neck cancer patients (N=38), and the retrospective study of the 4FD / IMRT treatment of the prostate cancer patients (N=10), the 3DCRT treatments of the left-breast cancer patients (N=8) and the left-lung cancer patients (N=8) respectively. The results have also been systematically presented in Table 5.6.

The UPI scores of the IMRT plans were also found to be in the range of 0.98-1.21, but the overall QF of the plans were estimated to be 0.93 ± 0.03 (N=5) in the SqIB treatment of the head and neck cancer patients. Furthermore, the mean UPI scores and the overall QF of the treatment

plans were found to be (a) in the range of 0.95-1.10 and 0.99 ± 0.00 respectively, in the IMRT treatment of the prostate cancer patients (N=10), (b) in the range of 0.93-1.11 and 0.98 ± 0.04 respectively, in the 3DCRT plans designed for the accelerated whole breast irradiation treatment of the left-breast cancer (N=8); and (c) in the range of 0.25-1.26 and 0.94± 0.04 respectively, in the 3DCRT treatment of the left-lung cancer patients (N=8). The optimal QFs of the XRT plans indicated that the toxicity can be significantly avoided in the normal tissue organs in the 3DCRT treatment of the left-breast cancer patients and the prostate cancer patients respectively.

In this study, the cDVH analysis of the GTV and 14 critical structures showed that the damage can be avoided in the spinal cord and brainstem due to radiation exposure at the corresponding $TD_{50,5}$'s (< 1% volume), however the salivary glands and the ct-esophagus were prone to the radiation toxicity in the SqIB (N=38) and SIB (N=3) treatments of the head and neck cancer patients. Similarly the cDVH analysis of the organs showed that the rectum and bladder can be secured by limiting the cumulative PD (69.6 ± 4.6 Gy; N=10) below the $TD_{50,5}$ (80Gy and 80Gy respectively) of the corresponding organs in the 4-FD box and the subsequent SqIB treatment of the prostate cancer patients. Furthermore the left-lung was also found to be significantly preserved since the average relative volume coverage at $TD_{50,5}$ (V(24.5 Gy)) was less than 13% in the cDVH analysis of the neighboring organs in the 3DCRT treatment of the left-breast cancer patients. However, the esophagus and the lung were found to be significantly vulnerable to the radiation toxicity in the cDVH analysis of the organs in the 3DCRT treatment of the left-lung cancer patients.

Biological modeling based outcome analysis (NTCP-TCP) parameters were found to be deterministic to estimate the clinical outcomes of the radiation therapy plans in the treatment of head and neck cancer patients (N=10), the prostate cancer patients (N=10), the left-breast cancer

patients (N=8), and the left-lung cancer patients (N=8) respectively. As discussed earlier in Fig. 5.13, the mean TCP for the PTV3 target was found to be 0.83 ± 0.05 (CI = 0.95), in the COMPOSITE plans in the SqIB treatment of the head and neck cancer patients (N=10) using the Poisson statistics model. Similarly the overall tumor progression free survival was observed to be 82% in the median 2 year follow up of the head and neck cancer patients treated with the SqIB techniques [39]. The prognosis was also found to be very consistent with the mean TCP computed for the targets (GTV and PTV3) in the COMPOSITE plans of the sub-group (N=10) of the 83 head and neck cancer patients. Similarly the mean NTCPs were algebraically estimated to be (a) (45.1 ± 15.0 %; CI: 0.95) for the parotid glands, (b) (60.5 ± 4.0 %; CI: 0.95) for the submandibular glands, and (c) (17.0 ± 9.0 %; CI: 0.95) for the ct-esophagus using the cumulative dose-volume effects in the corresponding organs contoured in the SqIB plans (PTV1, PTV2, and PTV3 respectively) in the treatment of the head and neck cancer patients (N=10) using the LKB models respectively. It can also be noticed that the normal tissue complications in the median 2 year follow up, is in good agreement with the mean NTCP values estimated for the parotid glands and ct-esophagus in the SqIB treatment of a sub-group (N=10) of the 83 head and neck cancer patients. However, the observed discrepancies can be attributed to the lack of sufficient information of the tissue inhomogeneity correction of the critical organs in the corresponding radiobiological models. Similar complications have also been reported by various oncologists at various institutions in other types of IMRT treatments of head and neck cancer patients [40]. Thus it can also be concluded that the salivary glands are significantly vulnerable to the radiation toxicity in the IMRT treatment of the head and neck cancer patients.

Similarly the smaller values of NTCP of rectum and bladder in all 4 plans proved that the conventional 4-FD box technique and SqIB treatment dual modality was a favorable combination

for the efficient treatment of the prostate cancers using high energy radiation. In the similar manner, the lower values of NTCPs for the left-lung (< 1%) and heart (< 1%) showed that the accelerated whole breast irradiation technique was also an appropriate choice for the efficient treatment of the breast cancer patients. However, the largest value of NTCP of thoracic-esophagus (0.25 ± 0.02) has brought a serious attention to the left-lung cancer patients treated with 3DCRT techniques. Studies have shown that, stereotactic body radiation therapy (SBRT) may have an additional advantage to reduce the dose in neighboring critical organs such as heart, esophagus, and lungs by using sophisticated imaging techniques with multiple radiation beams over 3DCRT treatment of early-stage medically inoperable NSCLC patients.

Furthermore, the sDVH analysis was also performed to determine the cause of radiation toxicity in the critical organs in the selective complicated cases as follows: (a) SqIB treatment of head and neck cancer patients (N=10), and (b) 3DCRT treatment of the left-lung cancer patients (N=8). It showed that the submandibular glands were relatively dominated by a large number of critical spots and hot spots as compared to the parotid glands, and ct-esophagus in the SqIB treatment of the head and neck cancer patients. Similarly a significant number of critical spots and hot spots were also detected in the esophagus in the zDVH analysis of the neighboring organs in the 3DCRT treatment of the left-lung cancer patients. The presence of a large number of critical spots obviously poses a high level of risks of losing or impairing the functionality of the neighboring organs such as esophagus and heart, in such types of treatments. It warrants further improvements in the radiation guided treatment methodologies of the complicated cases such as head and neck, and lung cancer cases.

In clinical practice, it is generally assumed that the absorbed dose less than 1 Gy (SI unit) or 100 rad (cgs unit) is assumed to be the safe dose limit in preserving the normal functionality of

the human body. Various studies have also shown that CyberKnife robotic radiosurgery system (CRS) has better advantage in sparing the salivary glands, larynx and mandible, over the IMRT techniques in treatment of head and neck cancer patients. This study supports the novel formalism known as, CUBS (cDVH analysis, UPI evaluation, biological modeling, and spatial DVH analysis respectively) technique, as an effective and more practical approach to evaluate the radiotherapy treatment plans to improve the treatments, to prevent the complications in organs, and to assess the radiobiological consequences of the advanced radiation therapy treatments in various types of cancer.

Table 5.6 The chart analysis of the radiation therapy treatment plans designed in the treatment of various types of cancers using the CUBS (cumulative DVH analysis, universal plan-indices evaluation, biological modeling based outcomes, and spatial DVH analysis respectively) technique.

Case study	Techniques (PD)	UPIs / QF Index	cDVH statistics (Safe / Risk)	TCP / NTCP Indices	zDVH analysis (HC Ratio)
Head and neck cancer	Sequential IMRT Boost (SqIB technique; 72.5 ± 0.70 Gy; N=38)	(0.98-1.21) / 0.93 ± 0.03 (N=5)	Sp. cord – Brainstem / (Salivary glands, Ct - esophagus, Larynx) (N=38).	83% GTV/ (45-60%; Salivary glands) (N=10)	Lt / Rt Submandibular glands (N =10). (0.79 ± 0.11) / (0.83 ± 0.11)
Prostate cancer	Conventional 4-field and SqIB techniques (69.6 ± 4.6 Gy; N=10)	(0.95-1.10) / 0.99 (IMRT, N=10)	Rectum and bladder (PD< TD50; N=10) / NA	66% GTV/ (< 1.0 %; Rectum and Bladder; 4-field tech) (N=10)	NA
Left-breast cancer	3DCRT plus EBT (56.05 ± 5.23 Gy; N=8)	(0.93-1.11) / 0.98 ± 0.04 (N=5)	Heart/ Left-lung (N=8)	93% PTV/ (< 1.0 % Left-lung) (N=8)	NA
Left-lung cancer (Curative)	3DCRT technique (54.77 ± 3.33 Gy; N=8)	0.25-1.46/ 0.94 ± 0.04 (N=7)	Spinal cord / (Lung and Esophagus) (N=8)	68-80% PTV/ (25 % Esophagus) (N=8)	Esophagus (0.75 ± 0.12; N=9)

Chapter 6

Summary

6.1 Conclusion

The precise detection of the GTVs and MTVs using CT or PET/CT scans is the one of the key processes in the efficient diagnosis of the various types of cancers. On the other hand, the optimal planning of the radiation guided treatments is also very important for the accuracy of the treatments in cancer. A review study of various PET phantom volume measurements showed that a more practical approach such as the threshold based method with the better correlation of the tumor to background uptake (SUV) ratio and the tumor size, is recommended for the precise detection of the MTVs using the PET/CT dual imaging modalities in the radiation therapy treatments. In SUV based method, the SUV value should not be just a constant (e.g. 2.5), but as a function of tumor size, the metabolic characteristics of the tumor targets and the normal organs such as liver.

Modern techniques such as 3DCRT, EBT, and IMRT, are generally utilized to treat various types of cancer patients using the optimal radiation therapy treatment plans. The treatment plans can be evaluated using the several DVH based models such as cDVH, UPIs and sDVH respectively. Furthermore, various types of biological models such as Poisson statistics based TCP model and Lyman-Kutcher-Burman NTCP model, are the very efficient tools to estimate the tumor progression free survival rate and the NTCPs of the critical organs in the radiation therapy treatments in cancer.

Higher values of the UPI scores and the lower grades of the quality factors also indicate the higher probability of the complications in the critical organs. Fortunately, the UPI evaluations showed that the 3DCRT and IMRT techniques offer the promising results by maintaining the dose-homogeneity and conformality of the targets sparing the critical organs in the radiation therapy treatments of the left-breast cancer patients and the prostate cancer patients.

This study also revealed that the radiation toxicity cannot be avoided in the salivary glands but brainstem and spinal cords, in consistent with the follow-up results of the SqIB treatment of the 83 head and neck cancer patients. The presence of a significant number of critical spots was found to be one of the major causes of the higher values of NTCPs in the salivary glands from the sDVH analysis. These critical spots led to the critical failures of the salivary glands in such types of treatments. However the higher TCP levels were the major advantage of the SqIB treatment of the head and neck cancer patients. Although SIB techniques relatively deliver high dose-rate (2.0-2.2 Gy/ fraction) to destroy the tumor cells in comparison to the SqIB techniques, they are not favorable to the normal structures in the proximity of the tumor target. The sequential technique reduces the concentration of the hot and critical spots in the critical organs, and also maintains a constant fraction size of the radiation dose in the targets. The SqIB technique offers excellent tumor progression free survival and offers reduction in radiation toxicities as compared to the SIB techniques. Furthermore, the evaluation of the DVH statistics and the NTCP indices also indicated that the thoracic-esophagus are critical to the radiation toxicity in the 3DCRT treatment of the left-lung cancer patients.

In conclusion, the CUBS technique is one of the more practical approaches to evaluate the radiation therapy treatment plans in order to improve the quality of the treatments in the various types of cancers. More specifically, this technique is efficient to determine the radiobiological

outcomes and the primary cause of complications in the normal tissue organs in the radiation therapy treatments in cancer. The open source software system, HART, is also efficient to assess the radiation therapy treatment plans, to compute the biological outcomes and the dose-volume effects in normal tissue organs.

6.2 Future work

Notable future works are to explore the noble ideas in space-time DVH analyses in the advanced radiation therapy treatment plans designed for the treatment of various types of cancers. We also plan to perform the correlation study of multidimensional DVHs with the complications in neighboring organs in the critical type of treatments such as head and neck cancers, and lung cancers in the 4D treatment planning system. It is also expected to pursue an extensive evaluation of the outcomes of the ‘CUBS’ technique with the outcomes of the follow up studies in the radiation therapy treatment of a large number of patients diagnosed with various types of cancers.

Cited Literature

[1] McKinnell R G, Parchment R E, Perantoni A O and Pierce G B 2000. *The Biological Basis of Cancer*, Cambridge University Press, New York, NY.

[2] Grubbe E H 1933. Priority in the therapeutic use of x-rays; *Radiology* 21, p. 1212-17.

[3] Coutard H 1934. Principles of x-ray therapy of malignant disease; *Lancent* 2, p. 1-8.

[4] Jones L, Hoban P and Metcalfe P 2001. Use of the linear quadratic model in radiotherapy: a review Australas; *Phys. Eng. Sci. Med*. 24, p. 132-46.

[5] Podgorsak E, 2005. *Radiation Oncology Physics: A handbook for teachers and students*, International Atomic Energy Agency, Vienna.

[6] Williams R A and Beck M S (Eds.) 1995. *Process Tomography- Principles, Techniques and Applications*, Oxford (Butterworth-Heinemann).

[7] Jang S, Yun M, McDonough J, and Zhu T 2001. Tumor characteristics obtained using FDG-PET imaging in lung cancer and new strategies for 3D radiotherapy; *Med Phys.* 28(6): p.1217.

[8] Harms W 1999. Specifications for Tape/Network Format for Exchange of Treatment Planning Information; *Guidelines, RTOG 3D Quality Assurance Center*, version 4, Washington University.

[9] ICRU Report 50 1993. Prescribing, recording and reporting photon beam therapy. *International Commission on Radiation Units and Measurements*, Bethesda MD.

[10] ICRU Report 62 1999. Prescribing, recording and reporting photon beam therapy. *International Commission on Radiation Units and Measurements*, Bethesda MD.

[11] Aaltonen-Brahme P, Brahme A, Lax I, Levernes S, Naslund I, Reitan J, Turesson I 1997. Specification of dose delivery in radiation therapy; *Acta. Oncologica* 36, suppl.10.

[12] Dobbs H J, Parker N J, Hobday P, and Husband J E 1983. The use of CT in radiotherapy treatment planning; *Radiother. Oncol.* 37, p. 133-141.

[13] Hendee W R and Ibbott G S 1996. *Radiation Therapy Physics*, Mosby-Year Book Inc., St. Louis, MI.

[14] Khan F M 2003. *The Physics of Radiation Therapy*, Lippincott Williams and Wilkins, Philadelphia, PA.

[15] Webb S 2001. *Intensity Modulated Radiation Therapy*, Institute of Physics Publishing, Bristol and Philadelphia.

[16] Takahashi S 1969. Conformation radiotherapy, rotation techniques as applied to radiography and radiotherapy*; Acta. Radiat. Oncol. Biol. Phys.* 242.

[17] Brahme A 1996. Recent developments in radiation therapy planning and treatment optimization Australas; *Phys. Eng. Sci. Med.* 19, p. 53-66.

[18] Bortfeld T, Burkelbach J, Boesecke R and Schlegel W 1990. Methods of image reconstruction from projections applied to conformation therapy; *Phys. Med. Biol.* 35, p. 1423-1434.

[19] MacKenzie M A, Lachaine M, Murray B, Fallone B G, Robinson D and Field G C 2002. Dosimetric verification of the inverse planned step and shoot multi-leaf collimator fields from a commercial treatment planning system; *J Appl Clin Med Phys*. 3, 97-109.

[20] Boyer A, and Strait 1997. Delivery of intensity-modulated treatments with dynamic multileaf collimator; Proc. Meeting: *Intensity-Modulated Radiation Therapy: A clinical perspective*, London, 26 June 1997, 11-16.

[21] Meerleer G, Vakaet L , Gersem W, Wagter C, Naeyer B, and Neve W 2000. Radiotherapy of prostate cancer with or without intensity modulated beams: A planning comparison; *Int. J. Radiat. Oncol. Biol. Phys.* 47, p. 639-648.

[22] Emami B, Lyman J, Brown A, Coia L, Goitein M, Munzenrider JE, Shank B, Solin LJ, Wesson M 1991. Tolerance of normal tissue to therapeutic irradiation; *Int. J. Radiat. Oncol. Biol. Phys.* 21(1): p. 109-22.

[23] Kehwar TS 2005. Analytical approach to estimate the normal tissue complication probability using the best fit of normal tissue tolerance doses into the NTCP equation of the linear quadratic model; *J. Cancer. Res. Ther.* 1(3), p. 168-179.

[24] Luxton G, Keall P, and King C 2008. A new formula for normal tissue complication probability (NTCP) as a function of equivalent uniform dose (EUD); *Phys. Med. Biol.* 53, p. 23–36.

[25] Erik B, Peter J, Oda B, John R, Henri V, Dirk P, Ben J, and Peter C 2000. Beam intensity modulation using tissue compensators or dynamic multi-leaf collimation in 3D conformal radiotherapy of primary cancers of the oropharynx and larynx, including the elective neck; *Int. J. Radiation Oncology Biol. Phys.* 47(5), p. 1299–1309.

[26] Debelleix C, Pointreau Y, Lafond C, Denis F, Calais G,and Bourhis JH 2010. Normal tissue tolerance to external beam radiation therapy: larynx and pharynx; *Cancer Radiother*. 14(4-5), p. 301-306.

[27] Francescon P, Cavedon C, Reccanello S 2000. Photon dose calculation of a three-dimensional treatment planning system compared to the Monte Carlo code BEAM; *Med Phys* 27; p. 1579–1587.

[28] Irvine C, Morgan A, Crellin A, Nisbet A, and Beange I 2004. The Clinical Implications of the Collapsed Cone Planning Algorithm; *Clinical Oncology* 16: p. 148–154.

[29] Soderstrom S, and Brahme A 1992. Selection of suitable beam orientations in radiation therapy using entropy and Fourier transform measures; *Phys. Med. Biol*. 37, p. 911–924.

[30] Mageras G, and Mohan R 1993. Application of fast simulated annealing to optimization of conformal radiation treatments; *Med. Phys*. 20, p. 639–647.

[31] Pyakuryal A, Myint W K, Gopalakrishnan M, Jang S, Logemann J, and Mittal B 2010. A computational tool for the efficient analysis of dose-volume histograms from radiation therapy treatment plans; *Journal of Applied Clinical Medical Physics*, Vol 11, No 1.

[32] Lyman JT 1985. Complication probability as assessed from dose-volume histograms; *Radiat Res Suppl*. 8, p. s13 – s19.

[33] Warkentin B, Stavrev P, Stavreva N, Field C, and Fallone BG 2004. A TCP-NTCP estimation module using DVHs and known radiobiological models and parameter sets; *J Appl Clin Med Phys* 5(1), p. 50–63.

[34] Kutcher G, and Burman C 1989. Calculation of complication probability factors for non-uniform normal tissue irradiation: the effective volume method; *Int J Radiat Oncol Biol Phys* 16(6): p. 1623–30.

[35] Driver D, and Dobbs H 2004. Improvements in radiotherapy practice: the impact of new imaging technologies; *Cancer Imaging* 4(2), p. 142–150.

[36] Dogan N, King S, Emami B, Mohideen N, Mirkovic N, Leybovich L, and Sethi A 2003. Assessment of different IMRT boost delivery methods on target coverage and normal tissue sparing; *Int J Radiat Oncol Biol Phys 57*(5): p. 1480–91.

[37] Deasy J, Blanco A, and Clark V 2003. CERR: a computational environment for radiation therapy research; *Med Phys* 30(5), p. 979-85.

[38] Pyakuryal A 2009. Implications of Histogram Analysis in Radiation Therapy (HART) Software; *Proceedings* of 11th World Congress for Medical Physics and Biomedical Engineering, IFMBE proceedings 25/I, p. 5- 8.

[39] Bhate A, Koneru N, T. Thomas, and B Mittal 2009. Sequential Intensity Modulated Radiation Therapy for the Head and Neck cancer: The Northwestern University experience; *Int J Radiat Oncol Biol Phys 75*(3): Supplement p. S433.

[40] Lee S, Kim T, Kim J, Park S, Pyo H, Shin K, Kim D, Kim J, and Cho K 2006. Evaluation of parotid gland function following the intensity modulated radiation therapy for the head and neck cancer; *Cancer Res Treat*. 38(2), p.84-91.

Appendix A

Publications and presentations

1. A Pyakuryal, D Pokhrel, S Jang, M Gopalakrishnan, V Sathiaseelan, and B Mittal, "Implication of the Spatial Resolution of the Conventional Dose-Volume Histogram Analysis in the Radiation Therapy Treatments,'' *Med Phys 38(6)*, p. 3680 (2011).

2. A. Pyakuryal, K. Myint, M. Gopalakrishnan, S. Jang, J. Logemann and B. Mittal, "A computational tool for the efficient analysis of the dose volume histograms from radiotherapy treatment plans," *Journal of Applied and Clinical Medical Physics***,** Vol. 11, No 1, p.3013 (2010).

3. A. Pyakuryal and S. Jang, "Evaluation of universal plan-indices and quality factor of treatment plans in radiotherapy treatment of cancer," *Proceedings of the SPIE Medical Imaging Annual Conference*, Feb. 13 -18, San Diego, CA (2010).

4. A. Pyakuryal , C. Chen and S. Dhungana, "Impact of Radiation in the Critical Organs in Radiation therapy Treatment of Breast and Lung Cancers," Abstract, *American Physical Society Conference***,** Feb 13-15, Washington, D.C. (2010).

5. A. Pyakuryal, "Implications of Histogram Analysis in Radiation Therapy (HART) Software," student paper published in the *Proceedings of 11th World Congress for Medical Physics and Biomedical Engineering*, IFMBE proceedings 25/I, pp. 5- 8 (2009).

6. W. Myint, A. Pyakuryal, M Gopalakrishnan, V.Sathiaseelan, and B. Mittal," A comparison of head and neck IMRT plans optimized with the biologically based versus dose-volume based objectives in a commercial treat ment planning system," *Med. Phys. 36(6)*, p. 2644 (2009).

7. W. Myint, A. Pyakuryal, M Gopalakrishnan, V. Sathiaseelan, and B. Mittal, "Evaluating head and neck IMRT plans with a computational tool for spatial dose-volume histograms," *Med. Phys. 36(6)***,** p. 2545 (2009).

8. A. Pyakuryal, "A Computational Study of Intensity Modulation Radiation Therapy (IMRT) Treatments of Head and Neck, and Prostate Cancers," Abstract presented in young investigator symposium, 26th *Annual Meeting of American College of Medical Physics*, May 02-05, West Virginia Beach, VA (2009).

9. S. Jang, A. Pyakuryal, K Myint, M. Gopalakrishnan, and B. Mittal, "Dose Volume Histogram (DVH) Analysis software for Radiation Therapy Research", *Med. Phys. 35(6)*, p.2812 (2008).

10. S. Jang, A. Pyakuryal, and J. Luo , " Review of the PET Tumor Volume Measurements for the Radiotherapy Treatment Planning ", Abstract, *First World Molecular Imaging Congress*, Sep 10-13, Nice, FR (2008).

Appendix B

Spatial dose-volume histogram analysis

DVHs are strong tools for three-dimensional treatment plan evaluation. However, the drawback is the loss of spatial information. In order to achieve two-dimensional dose distribution information across various planes and surfaces of an organ, zDVH and DSH analyses are the best evaluation techniques for CRT and IMRT plans. The zDVHs provide the spatial variation of the dose as well as the differential dose volume information along the z-axis with respect to the CT slice positions. DSHs provide the spatial variation of the dose in a surface perpendicular to the z-axis in the ROI of an organ.

HART accounts for all of the primary dose grid information and the 3-D co-ordinate geometry of the target and critical structures. The algorithm generates dDVHs (secondary data) to create the corresponding cumulative DVHs, DSHs, and zDVHs. The DSHs and zDVHs help identify "hot" and "cold" regions within each slice of the target or normal structure of interest.

It should be noted that the DVH may also be obtained from zDVH (D_i, z) by summing over the z-coordinates z_1, $z_2 \ldots z_n$ respectively. It can be expressed as,

$$\mathrm{DVH}(D_i) = \sum_{n=1}^{N_1} \mathrm{zDVH}(D_i, Z_n), \tag{1}$$

where D_i is a specific dose coverage sampling at z-coordinate position (z_n) in the n^{th} slice of the given CT image.

Similarly, the summation can be performed along the x and y-axes in order to obtain xDVH and yDVHs respectively, as given below,

$$\mathrm{DVH}(D_j) = \sum_{n=1}^{N_2} \mathrm{xDVH}(D_j, X_n), \tag{2}$$

$$DVH(D_k) = \sum_{n=1}^{N_3} yDVH(D_k, Y_n), \quad (3)$$

A general cDVH curve can be retrieved from the specific analysis of the 3 dimensional space based DVH curve that can help us to localize the ‘hot’ and ‘critical’ spots precisely in the contingent normal tissue organs. These spots are the primary cause of the complications in the normal tissue structures in the radiation therapy treatments.

$$DVH = \sum_{n=1}^{N_1} zDVH(D_i, Z_n) = \sum_{n=1}^{N_2} xDVH(D_j, X_n) = \sum_{n=1}^{N_3} yDVH(D_k, Y_n) \quad (4)$$

Appendix C

Universal plan-indices evaluation

High precision radiotherapy treatments such as CRT and IMRT have been frequently used in clinical routines in past decade. In order to maintain the precision and quality of these treatments, it is essential to perform accurate patient mapping including target and organ volumes, patient immobilization and treatment delivery utilizing an optimal treatment plan. The search for a single parameter to quantify the quality of a radiotherapy treatment plan has been ongoing, but as of yet unsuccessful. In this perspective, a simpler method of treatment plan indices (TPI) evaluation technique of radiotherapy treatment has been incorporated into HART.A universal plan indices (UPI) set has been defined by summarizing various recognized plan indices for plan evaluation of radio-surgical treatments, Gamma Knife (GK) treatments and conventional LINAC based treatments.

The overall quality factor (QF) of a plan can also be determined by combining the relative assessment of all plan indices in the UPI set by utilizing the DVH statistics extracted in HART. QF can be efficiently computed for a plan by assigning the relative weights to all UPI plan indices as a complete plan evaluation strategy. Plan indices in UPI set can be systematically described as follows:

i. Target coverage index (TCI) :

   TCI accounts for the exact coverage of PTV in a treatment plan at a given prescription dose (PD) as expressed below,

$$TCI = \frac{PTV_{PD}}{PTV}, \quad (1)$$

   where PTV_{PD} is the PTV coverage at PD, and PTV has usual meaning.

ii. Critical organ scoring index (COSI) :

   COSI is a measure of both target coverage and critical organ overdose. It can be expressed as given below,

$$COSI = \left[1 - \frac{\sum_{i=1}^{N} w_i V(OAR_i)_{\geq TOL}}{TCI} \right], \quad (2)$$

where $V(OAR_i)_{\geq TOL}$ is the fractional volume of i^{th} organ at risk (OAR) receiving more than tolerance dose (TOL), and relative weight (w_i) of fractional volume of each organ is 1/N.

iii. Radiation conformity index (RCI) :

RCI gives a consistent method for quantifying the degree of conformity based on isodose surfaces and volumes. It can be expressed as,

$$RCI = \frac{PTV_{PD}}{PTV_{0.95PD}}, \quad (3)$$

where $PTV_{0.95PD}$ is the PTV coverage at 95% of PD.

iv. Prescription isodose target volume conformal index (PITV) :

PITV assesses the conformity of a treatment plan. However it may not be an exact parameter to identify the beam isocenter that causes a plan not to conform to the shape of the target volume in a radio-surgery treatment. PITV can be expressed as,

$$PITV = \frac{PIV}{PTV}, \quad (4)$$

where PIV is the prescription isodose volume coverage for the target and normal tissues.

PITV >1 and PITV <1 refers to the over treatment and under treatment regions respectively. But it lacks to account properly the relative position of PIV with respect to PTV in radio-surgery and LINAC based plans.

v. Dose homogeneity index (HI) :

HI scales the “hot” spots in and around the planning target volumes. It can also be expressed as,

$$HI = \frac{D_{Max}}{PD}, \tag{5}$$

and the modified dose homogeneity index (MHI) is defined as,

$$MHI = \frac{D_{95}}{D_5}, \tag{6}$$

where D_{Max} is the maximum dose point in PTV. Similarly D_{95} and D_5 are the dose coverage at 95% and 5% volume of the PTV respectively.

vi. Conformality index (CI) and conformation number (CN) :

CI measures the conformity of a treatment plan. CN accounts for the relative measurement of dosimetric target coverage and sparing of normal tissues in a treatment plan.

$$CN = \frac{TCI}{TR}, \text{ and } CI = \frac{1}{TR}, \tag{7}$$

where treatment volume ratio (TR) is defined as,

$$TR = \frac{PIV}{PTV_{PD}}, \tag{8}$$

vii. Target volume ratio (TVR) :

TVR is an objective measure of how well the prescription isodose line conforms to the size and shape of the planning target volume. It is simply the inverse of ratio for PITV.

$$TVR = \frac{PTV}{PIV}, \tag{9}$$

viii. Dose gradient index (DGI) :

It examines the steepness or shallowness of dose fall-off in the target volume. It can be expressed as,

$$DGI = \frac{PTV_{PD}}{PTV_{0.50PD}}, \tag{10}$$

where $PTV_{0.50PD}$ is the planning target volume coverage at 50% of PD.

ix. New conformity index (NCI) :

NCI and HI allows for the quick and simple comparison of different radio-surgical treatment plans designed within the same or diverse radio-surgical systems such as between LINAC and Gamma Knife. NCI can be expressed as,

$$NCI = \frac{PIV * PTV}{PTV_{PD}^{2}}, \tag{11}$$

Thus UPI set can also be simply expressed as,

$$UPI = \{X_i\}, \tag{12}$$

where X_i = (TCI, COSI, RCI, PITV, HI, MHI, CN, TVR, DGI, NCI), for a number of N major plan indices (N=10). The number (N) can be arbitrarily selected from UPI set for treatment plan evaluation in HART.

The quality factor (QF) of a treatment plan can be analytically expressed in terms of the combination of above set of UPI indices as given below,

$$QF = \left[2.718 \exp\left(- \sum_{i=1}^{N} W_i X_i \right) \right], \tag{13}$$

where the values of weight factor (W_i) can be adjusted between zero to unity for all relatively weighted indices $\{X_i\}$ for a user defined number of indices (N) in the UPI set. The analytical expression in the argument of the exponential function in equation (12) is also termed as the UPI function. Thus the fundamental application of QF and UPI evaluations is to compare the conformity of plans among various trials for a treatment.

VITA

Education

University of Illinois at Chicago — Chicago, IL.
Doctor of Philosophy, Physics (PhD; Concentration: Radiation Oncology Physics) — (2003-2012)

Southern Illinois University — Carbondale, IL.
Master of Science, Electrical Engineering (MS; Specialty: VLSI and FPGA Circuit design) — (2000-2002)

Tribhuvan University — Kathmandu, Nepal.
Master of Science, Physics (MSc; Specialty: Solid State Physics) — (1994-1997)

Work Experience

Adjunct Instructor of Physics — (2011-2012)
Physical Science Department, Dominican University, — River Forest, IL.

Medical Physics Intern and Research Fellow — (2007-2011)
Department of Radiation Oncology, Northwestern University Memorial Hospital, — Chicago, IL.

Instructor of Mathematics and Physics — (2003-2011)
Federal TRIO Bridge Program / Department of Physics, University of Illinois at Chicago, — Chicago, IL.

Advanced Electronics Laboratory Instructor — (2000-2002)
Department of Electrical Engineering, Southern Illinois University, — Carbondale, IL.

Assistant Lecturer of Physics — (1998-2000)
Department of Radiation Physics, Tribhuvan University, — Kathmandu, Nepal.

Current Research

Intensive development of the open-source software system, ***Histogram Analysis in Radiation Therapy*** **(HART)**, to support the research in the radiation oncology and radiation therapy physics around the globe, initially funded by National Institute of Health (**NIH)** and multi-institutional collaboration. The tool is also available freely online at http: //www2.uic.edu/~apyaku1.

Peer-Reviewed Journals and Conference Proceedings Articles Publications

1. **A. Pyakuryal,** D Pokhrel, S Jang, M Gopalakrishnan, V Sathiaseelan, and B Mittal, "Implication of the 3D spatial resolution of the conventional DVH analysis in the radiation therapy treatments,'' *Med Phys 38(6)***,** p. 3680 (2011).

2. **A. Pyakuryal**, K. Myint, M. Gopalakrishnan, S. Jang, J. Logemann and B. Mittal, "A computational tool for the efficient analysis of the dose volume histograms from radiotherapy treatment plans," *Journal of Applied and Clinical Medical Physics***,** Vol. 11, No. 1, *Article no.* 3013, p.137-157 (2010).

3. **A. Pyakuryal**, A.Keppa, M.Gopalakrishnan, S.Jang, V.Satheseelan and B.Mittal, "Current status of the Histogram Analysis in Radiation Therapy (HART): An open-source software system," *Med Phys 37(6),* p. 3217 (2010).

4. **A. Pyakuryal**, "Implications of Histogram Analysis in Radiation Therapy Software," student paper in *Proceedings of 11th World Congress for Medical Physics and Biomedical Engineering*, IFMBE proceedings 25/I, p. 5-8 (2009).

5. W. Myint, **A. Pyakuryal**, M. Gopalakrishnan, V. Sathiaseelan, and B. Mittal," Evaluating head and neck IMRT plans with a computational tool for the spatial dose-volume histograms," *Med Phys 36(6),* p. 2545 (2009).

6. S Jang, G Noren, **A. Pyakuryal**, B Curran, J Luo, and E Sternick, "A Dose-Volume Histogram (DVH) Study of Single and Multiple Shot GammaKnife Treatments," *Med Phys 36(6),* p. 2651 (2009).

7. **A. Pyakuryal**, K. Myint,M. Gopalakrishnan, S. Jang,V. Sathiaseelan,J. Logemann, and B.Mittal, " Improvements to the Histogram Analysis in Radiation Therapy (HART) Open-Source Software System," *Med Phys* 36(6), p. 2547 (2009).

8. S. Jang, **A. Pyakuryal**, K Myint, M. Gopalakrishnan, and B. Mittal, "Dose Volume Histogram (DVH) Analysis software for Radiation Therapy Research," *Med Phys 35(6),* p. 2812 (2008).

9. S. Jang, **A. Pyakuryal**, V. Sathiaseelan, J. Kalapurkal and J. Luo, "Statistical Analysis of the Iodine-125 Prostate (I-125) Brachytherapy," *Med. Phys. 34(6),* p. 2490 (2007).

Selective Abstracts and Presentations

1. **A. Pyakuryal**, C. Chen and S. Dhungana, "Impact of Radiation in the Organs in Radiation Therapy Treatment of Breast and Lung Cancers," Student abstract, *American Physical Society Conference***,** Feb 13-15, Washington, D.C. (2010).

2. **A. Pyakuryal**, "Dose Response Modeling of Organs in the Intensity Modulated Radiation Therapy (IMRT) Treatments," Student abstract presented in *54th Annual Meeting of the Health Physics Society*, July 12-16, Minneapolis, MN (2009).

3. **A. Pyakuryal**, "A Computational Study of Intensity Modulation Radiation Therapy (IMRT) Treatments of Head and Neck, and Prostate Cancers," Student abstract presented in the *26th Annual Meeting of American College of Medical Physics*, May 02-05, West Virginia Beach, VA (2009).

4. S. Jang, **A. Pyakuryal**, A. Kepka, E. Sternik et al., "A Comparative Study of Single Shot and Multiple Shot Gamma Knife Treatment using DVH Analysis," Abstract presented in the *14th International Leksell Gamma Knife Society Conference*, Abstract Book- p. 246; May 19-22, Quebec, CA (2008).

5. S. Jang, **A. Pyakuryal**, J. Luo, A. Alavi and E. Sternick, "Review of PET Tumor Volume Measurements for Radiation Therapy Planning," Abstract in the *1st World Molecular Imaging Congress*, Abs Book-p.54; Sep.10-13; Nice, FR (2008).

Grant and Awards

- Development of the DVH computational tool, HART, for radiotherapy research (NIH-NIDCD grants).

Professional Memberships and Journal Reviewers

- Member: American Association of Physicists in Medicine (AAPM): *Student Membership (2008-2012).*
- Member: American Physical Society (APS): *Student /Junior Membership (2000-2012).*
- Member: Health Physics Society (HPS): *Student Membership (2009-2012).*
- Reviewer: Radiotherapy and Oncology (*Journal of the European Society for Therapeutic Radiology and Oncology; 2012*).
- Reviewer: IEEE Proceeding Journals (*IEEE Symposium of Science, Engineering, and Technology, Indonesia; 2012*).

Skills

Computer programs and programming languages: MS Office; UNIX / Windows; HTML/ php; C++ / MATLAB.
